REPUBLIC OF TURKEY
YILDIZ TECHNICAL UNIVERSITY
GRADUATE SCHOOL OF SCIENCE AND ENGINEERING

NUMERICAL INVESTIGATION OF HYDRODYNAMICS AND MASS TRANSFER IN STRUCTURED PACKING

Volkan TOPALOĞLU

MASTER OF SCIENCE THESIS
Department of Mechanical Engineering
Program of Heat and Processing

Supervisor
Prof. Dr. Hakan DEMİR

February, 2026

REPUBLIC OF TURKEY
YILDIZ TECHNICAL UNIVERSITY
GRADUATE SCHOOL OF SCIENCE AND ENGINEERING

NUMERICAL INVESTIGATION OF HYDRODYNAMICS AND MASS TRANSFER IN STRUCTURED PACKING

A thesis submitted by Volkan TOPALOĞLU in partial fulfillment of the requirements for the degree of **MASTER OF SCIENCE** is approved by the committee on 11.02.2026 in Department of Mechanical Engineering, Program of Heat and Processing.

Prof. Dr. Hakan DEMİR
Yildiz Technical University
Supervisor

Approved By the Examining Committee

Prof. Dr. Hakan DEMİR, Supervisor
Yildiz Technical University _____

Assoc. Prof. Zafer GEMİCİ, Member
Yildiz Technical University _____

Assoc. Prof. Sertaç ÇADIRCI, Member
Istanbul Technical University _____

I hereby declare that I have obtained the required legal permissions during data collection and exploitation procedures, that I have made the in-text citations and cited the references properly, that I haven't falsified and/or fabricated research data and results of the study and that I have abided by the principles of the scientific research and ethics during my Thesis Study under the title of Numerical Investigation of Hydrodynamics and Mass Transfer in Structured Packing supervised by my supervisor, Prof. Dr. Hakan DEMİR. In the case of a discovery of false statement, I am to acknowledge any legal consequence.

Volkan TOPALOĞLU

Signature

The numerical calculations reported in this paper were partially performed at TUBITAK ULAKBIM, High Performance and Grid Computing Center (TRUBA resources).

To my family

ACKNOWLEDGEMENTS

I would like to express my deepest gratitude to my supervisor, Prof. Dr. Hakan Demir, for his continuous guidance, encouragement, and trust throughout the course of this research. His expertise in transport phenomena and computational modeling has been invaluable in shaping both the technical depth and the scientific rigor of this study. His analytical approach and insightful discussions have been instrumental in refining the methodology and interpretation of results.

I would also like to acknowledge my colleagues and mentors in the engineering industry for their understanding and for providing the flexibility that allowed me to dedicate time to this study alongside my professional responsibilities.

I gratefully acknowledge the computational resources provided by TRUBA (Turkish National High Performance Computing Center), which enabled the extensive numerical analyses presented in this thesis.

Finally, I would like to extend my sincere appreciation to my family for their continuous support and understanding throughout my academic and professional journey.

Volkan TOPALOĞLU

TABLE OF CONTENTS

LIST OF SYMBOLS ix

LIST OF ABBREVIATIONS xiii

LIST OF FIGURES xv

LIST OF TABLES xx

ABSTRACT xxi

ÖZET xxiii

1 INTRODUCTION 1

1.1 Background and Motivation 1

1.2 Internal Configurations in Separation Columns 2

1.3 Research Problem and Hypothesis 4

1.4 Objectives and Scope 6

1.5 Organization of the Thesis 7

2 LITERATURE SURVEY 8

2.1 Hydrodynamics 8

2.1.1 Experimental 8

2.1.2 Numerical 18

2.2 Reactive Absorption 24

2.2.1 Experimental 24

2.2.2 Numerical 27

2.3 Other CFD Applications in Separation Process 30

3 THEORETICAL BACKGROUND 32

3.1 Hydrodynamics 32

3.1.1 Gas Load 32

3.1.2 Liquid Load 32

3.1.3 Static and Dynamic Liquid Holdup 35

3.1.4 Role of Surface Tension and Wettability 35

3.1.5 Static Contact Angle . . . 36
3.1.6 Dynamic Contact Angle . . . 36
3.2 Interface Capturing and Capillarity Modeling . . . 38
3.3 Reactive Absorption . . . 39
3.3.1 Overall Mass Transfer Coefficient . . . 39
3.3.2 Interfacial Area . . . 39
3.3.3 CO_2–MEA Reaction Mechanism . . . 40
3.3.4 Interfacial Equilibrium and Henry's Law . . . 43
3.3.5 CO_2–MEA Kinetics and Apparent First Order Rate . . . 44

4 COMPUTATIONAL METHODOLOGY 46
4.1 Geometrical Representation of the Packing . . . 46
4.2 Mesh Generation . . . 47
4.2.1 Pressure Drop Benchmarking and Calibration . . . 47
4.2.2 Two-Phase Hydrodynamic Analyses . . . 50
4.2.3 Two-Phase Reactive Absorption Analyses . . . 50
4.3 Governing Equations and Physical Models . . . 50
4.4 Property Modeling . . . 53
4.4.1 Property Correlations for Dry Pressure Drop . . . 53
4.4.2 Property Correlations for Two-Phase Model . . . 53
4.4.3 Mixture Property Models . . . 54
4.5 Reactive Absorption Methodology . . . 57
4.5.1 Framework Development . . . 57
4.5.2 Volumetric Reaction Definition . . . 58
4.5.3 Mass Transfer Definition . . . 59
4.6 Initialization and Boundary Conditions . . . 59
4.6.1 Single Phase Boundary Conditions . . . 60
4.6.2 Two-Phase: Non-Reactive Hydrodynamics Boundary Conditions . . . 60
4.6.3 Two-Phase: Reactive Absorption Boundary Conditions . . . 62
4.7 Post-Processing and Derived Quantities . . . 64
4.7.1 Liquid Holdup . . . 64
4.7.2 Pressure Drop per Unit . . . 64
4.7.3 Interfacial Area . . . 65

5 RESULTS AND DISCUSSION 66
5.1 Single Phase Hydrodynamics . . . 66
5.1.1 Mesh Sensitivity Analysis . . . 66
5.1.2 Number of Prism Layers . . . 67
5.1.3 Effect of Number of REUs . . . 69

5.1.4 Effect of Sheet Spacing 70
5.2 Two-Phase Non-Reactive Hydrodynamics 71
5.2.1 Model Selection 72
5.2.2 Mesh Sensitivity Analysis 72
5.2.3 Liquid Holdup 74
5.2.4 Wet Pressure Drop 81
5.2.5 Interface Area 84
5.3 Two-Phase Reactive CO_2-MEA Absorption 88
5.3.1 Mesh Sensitivity Analysis 88
5.3.2 Transient Development of Reactive Absorption 92
5.3.3 Effective and Interfacial Area 93
5.3.4 Overall Mass Transfer Coefficient 94

6 CONCLUSION **98**

REFERENCES **101**

A APPENDIX **109**
A.1 Snapshots of Single-Phase Gas Flow 109
A.2 Snapshots of Transient Liquid Flow Development 113
A.3 Snapshots of Reactive Gas–Liquid Flow Evolution 120
A.4 UDF Algorithms 121
A.5 Reconstruction of Experimental Data and Derivation of CFD Validation Parameters 122
A.5.1 Data reconstruction and regression details 122
A.5.2 Calculating Corresponding u_G for Reactive Absorption . . . 123
A.5.3 Holdup Data from [2] 124
A.6 Snapshots of Ansys Fluent Interface 125

PUBLICATIONS FROM THE THESIS **128**

LIST OF SYMBOLS

T	Absolute Temperature, K
$E_{a,i}$	Activation energy for chemical reaction i, J kmol^{-1}
θ^*	Apparent (Observed) Contact Angle, $^\circ$
k_{app}	Apparent rate of chemical reaction, kmol m^{-3} s^{-1}
D_{ij}	Binary diffusion coefficient, m^2 s^{-1}
$\mathbf{F}_\mathrm{S}$	Capillary (surface tension) force per unit volume (CSF body force), N m^{-3}
Ca	Capillary Number, Dimensionless
α_ch	Channel angle, $^\circ$
S	Characteristic Length of Packing, m
D	Column Diameter, m
Ch	Constant used in reference [1], Dimensionless
c	Constant used in reference [2], Dimensionless
C_i	Constants for various empirical correlations, Dimensionless
θ_A	Contact angle of Advancing, $^\circ$
θ_E	Contact angle of Equilibrium, $^\circ$
θ_R	Contact angle of Receeding, $^\circ$
A_c	Cross section of the column, m^2
$\nabla \cdot (\cdot)$	Divergence Operator, Operator
μ_L	Dynamic Viscosity, Pa s
$\mu(T)$	Dynamic Viscosity as a function of temperature, Pa s
Φ	Fraction of wetted interface cells contributing to the mass transfer, Dimensionless
Fr	Froude Number, Dimensionless

f_0	Friction factor, Dimensionless
y_{CO_2}	Gas phase mole fraction of CO_2, Dimensionless
F_g	Gas Load Factor, $(\mathrm{m\,s^{-1}})\sqrt{\mathrm{kg\,m^{-3}}}$
c_f	Gas-Liquid interaction coefficient, Dimensionless
∇	Gradient Operator, Operator
g	Gravitational Acceleration, m s^{-2}
Ha	Hatta Number, Dimensionless
c_p	Heat capacity, J kg^{-1} K^{-1}
z	Height of the domain of the packing, m
Z	Height of the packing, m
$H_{cp}(T)$	Henry constant in (c/p) convention as a function of Temperature, mol m^{-3} Pa^{-1}
$H_{px}(T)$	Henry constant in (p/x) convention as a function of Temperature, Pa
a_{int}	Interfacial Area of Liquid-Gas Phases, m^2 m^{-3}
x_{eq}	Interfacial equilibrium mole fraction of CO_2 in liquid, Dimensionless
γ_{LG}	Interfacial Tension between Liquid-Gas, N m^{-1}
γ_{SG}	Interfacial Tension between Solid-Gas, N m^{-1}
γ_{SL}	Interfacial Tension between Solid-Liquid, N m^{-1}
k_{L0}	Liquid film mass transfer coefficient, m s^{-1}
h_L	Liquid holdup, %
ρ_L	Liquid Mass Density, kg m^{-3}
$\rho_L(T)$	Liquid mass density as a function of temperature, kg m^{-3}
L	Liquid mass flux, m^3 m^{-2} h^{-1}
$C_L(T)$	Liquid molar density as a function of temperature, mol m^{-3}
x_L	Liquid mole fraction, Dimensionless
Δx	Liquid side driving force, Dimensionless
h_{th}	Liquid theoretical holdup, %

S_{int}	Liquid-Gas Interfacial Area, m
κ	Local interface curvature, m^{-1}
C	Mass Concentration of component, kg m^{-3}
C^*	Mass Concentration of equilibrium of component, kg m^{-3}
$\dot{m}$	Mass Source Term, kg m^{-3} s^{-1}
K_G	Mass Transfer Coefficient, mmol m^{-2} s^{-1} kPa^{-1}
ΔX	Minimum length of a cell in the domain of the mesh, m
$k_G a_e$	Overall Mass Transfer Coefficient, s^{-1}
$K_G a_e$	Overall Mass Transfer Coefficient, kmol m^{-3} h^{-1} kPa^{-1}
B	Packing channel base, m
a_e	Packing effective area, m^2 m^{-3}
d_p	Packing equivalent diameter for various models, m
a_0	Packing Geometry Specific Area, m^2 m^{-3}
β	Packing inclination angle, $^\circ$
a_p	Packing total area, m^2 m^{-3}
a_h	Packing wetted surface area, m^2 m^{-3}
p_{CO_2}	Partial pressure of CO_2 in gas phase, Pa
a_{pr}	Perforation spacing, m
A_i	Pre-exponential (frequency) factor for chemical reaction, m^3 $kmol^{-1}$ s^{-1}
h_0	Pre-loading holdup, Dimensionless
ΔP_{dry}	Pressure Drop for Dry Gas Flow, Pa
ΔP_{wet}	Pressure Drop for Liquid-Gas Flow, Pa
k_i	Rate constant for chemical reaction i (Arrhenius form), m^3 $kmol^{-1}$ s^{-1}
μ_0	Reference dynamic viscosity, Pa s
T_0	Reference Temperature, K
Re	Reynolds Number for Gas, Dimensionless
Sc	Schmidt Number, Dimensionless

$\mathbf{u}$	Shared (mixture) velocity field, m s^{-1}
F	Sheet face to face distance (gap), m
Sh	Sherwood Number, Dimensionless
a_G	Specific area density, m^2 m^{-3}
u_L	Superficial Velocity, m s^{-1}
σ	Surface Tension, N m^{-1}
γ	Surface tension coefficient, N m^{-1}
S_0	Sutherland constant, K
k	Thermal conductivity, W m^{-1} K^{-1}
P_{abs}	Total absorber pressure, Pa
Pr_t	Turbulent Prandtl Number, Dimensionless
$\hat{\mathbf{n}}$	Unit normal vector to the interface (reconstructed from α_l), Dimensionless
R	Universal Gas Constant, J mol^{-1} K^{-1}
β	van't Hoff slope parameter, K
α_L	VOF Liquid Fraction, Dimensionless
ϵ	Void Fraction of the Packing, Dimensionless
V_{cell}	Volume of the cell "i" in the mesh, m^3
V_{domain}	Volume of the computational domain, m^3
$\dot{V}_L$	Volumetric Flow Rate, m^3 h^{-1}
N	Volumetric Molar Absorption Rate, mol m^{-3} s^{-1}
θ	Wall Contact Angle, °
Δ	Wall Contact Angle Advancing/Receeding Amplitude, °
θ_{dyn}	Wall Dynamic Contact Angle, °
$\hat{\mathbf{n}}_w$	Wall normal unit vector, Dimensionless
θ_S	Wall Static Contact Angle, °
$\hat{\mathbf{t}}_w$	Wall tangential unit vector, Dimensionless
We	Weber Number, Dimensionless
L_p	Wetted perimeter in cross sectional slice of packing, m

LIST OF ABBREVIATIONS

AEEA	Aminoethylethanolamine
AR	Aspect Ratio
BSL	Bounded Second order Linear
CAD	Computer Aided Design
CFD	Computational Fluid Dynamics
CFL	Courant-Friedrichs-Lewy
CSF	Continuum Surface Force
CT	Computed Tomography
DCA	Dynamic Contact Angle
DES	Detached Eddy Simulation
HETP	Height Equivalent to a Theoretical Plate
HTU	Height of a Transfer Unit
JT	Joule-thompson
LOX	Liquid-oxygen
MEA	Monoethanolamine
MDEA	Methyldiethanolamine
MF-CST	Mass Fraction – Continuous Species Transfer
PDU	Process Development Unit
PZ	Piperazine
RANS	Reynolds Averaged Navier–Stokes
REU	Representative Elementary Unit
RNG	Renormalization Group
SCA	Static Contact Angle

SIMPLE	Semi-implicit Method for Pressure Linked Equations
SST	Shear Stress Transport
VOF	Volume of Fluid

LIST OF FIGURES

Figure 1.1 Publications about "CFD" & "Structured Packing" keywords per year with pie chart showing the country-wise distribution . . 2
Figure 1.2 Internals of the column: (a) mist eliminator, (b) liquid distributor, (c) random packings, (d) structural packings, and (e) trays [9] 3
Figure 1.3 6-REU model used for single-phase dry-gas pressure-drop calibration. 4
Figure 1.4 Single REU used for reactive two-phase hydrodynamics and mass transfer modeling. 5
Figure 2.1 Schematic packing layers and holdup profiles below and above the loading point (Adapted from [2]) 9
Figure 2.2 Liquid holdup (%) and wetted area as function of the number of prism layers [25]. 12
Figure 2.3 Effect of contact angle (θ_{wall}) on liquid film distribution (Adapted from [25]) 13
Figure 2.4 Experimental absorption column used and overall process configuration of the system [16]. 14
Figure 2.5 Comparison of fractional area correlations for Mellapak 500.Y reported by [16] with respect to the liquid load [16, 26–29]. . . . 14
Figure 2.6 3D view of Mellapak 500.Y (30 mm); water/air, 28 $m^3\,m^{-2}\,h^{-1}$; packing (gray), liquid (red-orange)[18]. 16
Figure 2.7 Holdup values along the packing height with the water/air system without counter-current gas flow (Adapted from [18]). . 17
Figure 2.8 Representative CT images of packing element for $B = 20\ \mathrm{m^3/m^2h}$ and $F_g = 0$. (a,b) Mellapak 500.Y with water and isopropanol, respectively; (c,d) Mellapak 250.Y with water and isopropanol. (e) Examples of liquid films (1), rivulets (2), and bridges (3) are highlighted. [17] 18
Figure 2.9 Three dimensional flow in a corrugated packing channel with streamlines colored by velocity and cross sections colored by pressure. Adapted from [31] 19

Figure 2.10 Effect of sheet perforations on transient liquid holdup (a) and normalized interfacial area (b) for static contact angles $30°$, $50°$, and $70°$ (Adapted from [11]). 20
Figure 2.11 Rivulet flow on structured packing [12]: (a) 53.8 mL/min, (b) close up of a, (c) CFD at 41.8 mL/min. 21
Figure 2.12 Transient wetting of a three REU stack at $L = 62\,\mathrm{m^3\,m^{-2}\,h^{-1}}$: (a) initially wetted evolution; (b) initially dry snapshot at $t = 2.0\,\mathrm{s}$; (c) comparison of $a_{int}(t)$ for wetted and dry starts; (d) $\Delta a_{int}(t)$ showing a slightly larger change at lower liquid load for the same dynamic contact angle settings. 22
Figure 2.13 Irrigated pressure drop with respect to different F_G along with (a) $u_L = 0.0033$ m/s and (b) $u_L = 0.0203$ m/s (Adapted from [34]) 23
Figure 2.14 K_G versus CO_2 loading for 5 mol L^{-1} MEA at 313 and 333 K [40] 27
Figure 2.15 Gas-phase CO_2 mole fraction along column height: (a) CFD contours for the full column; (b) comparison of porous-media CFD predictions [46] 29
Figure 2.16 MF–CST with VOF Simulation over three stacked REU of Mellapak 250Y: (a) liquid volume fraction highlighting film and rivulet accumulation at corrugation junctions, (b) ammonia mass fraction alteration along the flow. (Adapted from [47]). . . 30
Figure 3.1 Liquid holdup h_L as a function of gas load F_G for various liquid loads L for Mellapak 500Y structural packing. Reproduced from [2]. 34
Figure 3.2 Definition of the static contact angle θ_{wall} on a horizontal solid surface. 36
Figure 3.3 Definition of the dynamic contact angle θ_A and θ_R on an inclined solid surface. 37
Figure 3.4 Concentration and partial pressure profiles in the two film concept. 41
Figure 3.5 Schematic representation of penetration and surface renewal concepts. 43
Figure 4.1 Representation of six-REU's, four-REU's and single-REU . . . 46
Figure 4.2 Dimensions defined to represent Sulzer Mellapak 500.Y 47
Figure 4.3 Dimensions defined to represent Sulzer Mellapak 500.Y 48
Figure 4.4 Dimensions defined to represent Sulzer Mellapak 500.Y 49
Figure 4.5 Reactive absorption framework developed for the study 57
Figure 4.6 Multiple-REU's of Mellapak 500.Y. and associated boundary conditions for gas pressure drop 60

Figure 4.7 Single representative elementary unit (REU) of Mellapak 500.Y. and associated boundary conditions for two-phase studies 61
Figure 5.1 Dry unit pressure drop across different number of cells. Panel (a) compares numerical predictions with the Stichlmair et al. [30] correlation as a function of gas load F_G. Panel (b) Corresponding relative deviation from the correlation. 68
Figure 5.2 Effect of near-wall prism layers on the predicted dry unit pressure drop in the Mellapak 500.Y REU. (a) Meshes with 0, 8, and 12 prism layers compared against the Stichlmair et al. [30] correlation versus gas load F_G. (b) Corresponding relative deviation from the correlation. 69
Figure 5.3 Dry unit pressure drop in Mellapak 500.Y REUs with 1, 4, and 6 repeating units at similar cell counts per REU. (a) CFD predictions compared with the Stichlmair et al. [30] correlation versus gas load F_G. (b) Corresponding relative deviation from the correlation. 70
Figure 5.4 Dry unit pressure drop across 6 REUs versus gas load F_G for three face-to-face sheet spacings. Markers indicate CFD results for 2.00, 0.40, and 0.24 mm, grey circles show Tsai [16] experimental data, and the gray line denotes the Stichlmair [30] correlation. 71
Figure 5.5 Liquid holdup sensitivity analysis with minimum maximum and mean values 73
Figure 5.6 Wet pressure drop sensitivity analysis with minimum maximum and mean values 74
Figure 5.7 Interface area sensitivity analysis with minimum maximum and mean values 75
Figure 5.8 Three hold-up correlations compared in the range of 5-150 m3/m2-h liquid loads [2], correlations were computed for the present study. 76
Figure 5.9 Effect of liquid load on holdup compared with correlation by Tsai based on Billet–Schultes [1, 16]. 76
Figure 5.10 Effect of liquid load on holdup compared with correlation by Billet–Schultes for $20\%wt$ MEA at $36^{\circ}\mathrm{C}$ [1]. 77
Figure 5.11 Effect of gas load on liquid holdup compared with correlation by Tsai based on Billet–Schultes [1, 16] 78
Figure 5.12 Effect of static wall contact angle on liquid holdup compared with correlation by Tsai based on Billet–Schultes [1, 16] 79

Figure 5.13 Static contact angle and dynamic contact angle comparison between 0.8s-1.0s: iso-surface at $\alpha = 0.5$ 80
Figure 5.14 Dynamic contact angle and static contact angle comparison for holdup 81
Figure 5.15 Dynamic contact angle and static contact angle comparison for relative interface area 81
Figure 5.16 Effect of liquid load on pressure drop compared with correlation by Tsai based on Stichlmair [16, 30] 83
Figure 5.17 Effect of gas load on pressure drop compared with correlation by Tsai based on Stichlmair [16, 30] 83
Figure 5.18 Effect of gas load on pressure drop compared with correlation by Tsai based on Stichlmair [16, 30] 84
Figure 5.19 Effect of liquid load on interface area compared with correlations by Tsai [64], Billet-Schultes [27],Schug [18] depending on different iso-surfaces 86
Figure 5.20 Effect of gas load on interface area compared with Billet-Schultes [27] 87
Figure 5.21 Effect of wall static contact angle on interface area compared with Billet-Schultes [27] 87
Figure 5.22 Effect of number of cells to the mass transfer of REU 89
Figure 5.23 Reactive absorption sensitivity analysis comparing $K_g a_e$ with a_{int} and the $\mathrm{CO_2}$ outlet mole fraction over a $1.0\,\mathrm{s}$ interval. Time-averaged values (grayed area) were computed over the pseudosteady-state window from 0.70 to $0.95\,\mathrm{s}$. Operating conditions were $L = 22.91\,\mathrm{m^3\,m^{-2}\,h^{-1}}$ and $F_g = 0.3\,\mathrm{m\,s^{-1}}$, using $20\,\mathrm{wt\%}$ MEA at $36\,^{\circ}\mathrm{C}$. 91
Figure 5.24 Transient reactive absorption for single REU: Streamlines, liquid volume fraction ($\alpha_L = 0.5$) and CO_2 absorption for 0.8, 0.9 and 1.0s (MEA ≈20% wt. at 36°C, $\theta_{wall} = 50°$, $L = 23\ m^3 m^{-2} h$, $F_g = 1.3, m/s\ (kg/m^3)^{0.5}$) 93
Figure 5.25 Comparison for calculated a_e values [27, 29, 35, 64] and the CFD Results a_{int} across liquid load of $L = 3.82 - 22.91\ m^3 m^{-2} h$ 94
Figure 5.26 Comparison of calculated $K_g a_e$ values [kmol $\mathrm{m^{-3}\,h^{-1}\,kPa^{-1}}$] with experimental data from Aroonwilas [19] 95
Figure A.1 Pressure contour of single-phase sectioned view for six-REUs at $F_g = 1.445$ 110
Figure A.2 Velocity contour of single-phase sectioned view for six-REUs at $F_g = 1.445$ 111

Figure A.3 Turbulent kinetic energy contour of single-phase sectioned view for Six-REUs at $F_g = 1.445$ 112
Figure A.4 Two-phase liquid flow streams for 0.05 s to 1.00 s (Water at 25°C, $\theta_{wall} = 70°$, $L = 25\ m^3hm^{-2}$, $F_g = 0.3$, $m/s\ (kg/m^3)^{0.5}h$)113
Figure A.5 Two-phase liquid flow streams for 0.05 s to 1.00 s (Water at 25°C, $\theta_{wall} = 70°$, $L = 50\ m^3hm^{-2}$, $F_g = 0.3$, $m/s\ (kg/m^3)^{0.5}h$)114
Figure A.6 Two-phase liquid flow streams for 0.40 s to 0.85 s (Water at 25°C, $\theta_{wall} = 70°$, $L = 75\ m^3hm^{-2}$, $F_g = 0.3$, $m/s\ (kg/m^3)^{0.5}h$)115
Figure A.7 Two-phase liquid flow streams for 0.40 s to 0.85 s (Water at 25°C, $\theta_{wall} = 45°$, $L = 75\ m^3hm^{-2}$, $F_g = 0.3$, $m/s\ (kg/m^3)^{0.5}h$)115
Figure A.8 Two-phase liquid flow streams for 0.40 s to 0.60 s (Water at 25°C, $\theta_{wall} = 30°$, $L = 75\ m^3hm^{-2}$, $F_g = 0.3$, $m/s\ (kg/m^3)^{0.5}h$)116
Figure A.9 Two-phase liquid flow streams for 0.40 s to 0.85 s (Water at 25°C, $\theta_{wall} = 70°$, $L = 50\ \ m^3m^{-2}h$, $F_g = 0.633$, $m/s\ (kg/m^3)^{0.5}h$) 116
Figure A.10 Two-phase liquid flow streams for 0.40 s to 0.85 s (Water at 25°C, $\theta_{wall} = 70°$, $L = 50\ \ m^3m^{-2}h$, $F_g = 0.900$, $m/s\ (kg/m^3)^{0.5}h$) 117
Figure A.11 Two-phase liquid flow streams for 0.40 s to 0.85 s (Water at 25°C, $\theta_{wall} = 70°$, $L = 50\ \ m^3m^{-2}h$, $F_g = 1.084$, $m/s\ (kg/m^3)^{0.5}h$) 117
Figure A.12 Two-phase liquid flow streams for 0.40 s to 0.85 s (Water at 25°C, $\theta_{wall} = 70°$, $L = 50\ \ m^3m^{-2}h$, $F_g = 1.355$, $m/s\ (kg/m^3)^{0.5}h$) 118
Figure A.13 Two-phase liquid flow streams for 0.40 s to 0.85 s (Water at 25°C, $\theta_{wall} = 70°$, $L = 50\ m^3m^{-2}h$, $F_g = 0.3$, $m/s\ (kg/m^3)^{0.5}h$)118
Figure A.14 Two-phase liquid flow streams for 0.40 s to 0.85 s (Water at 25°C, $\theta_{wall} = 70°$, $L = 50\ m^3m^{-2}h$, $F_g = 0.3$, $m/s\ (kg/m^3)^{0.5}h$)119
Figure A.15 Reactive absorption for 0.30 s to 1.2 s (MEA ≈20% wt. at 36°C, $\theta_{wall} = 50°$, $L = 23\ m^3m^{-2}h$, $F_g = 1.3$, $m/s\ (kg/m^3)^{0.5}h$) . . 120
Figure A.16 Fitted validation curves from the reference [19] 123
Figure A.17 Liquid holdup h_L as a function of gas load F_G for various liquid loads L for Mellapak 500Y structural packing. (Figure from [2]) 125
Figure A.18 ANSYS-Fluent property mixture window 125
Figure A.19 ANSYS-Fluent phase interaction 126
Figure A.20 ANSYS-Fluent reaction no: 1 126
Figure A.21 ANSYS-Fluent reaction no: 2 127

LIST OF TABLES

Table 1.1 Research objectives 6
Table 1.2 Scope and assumptions 7
Table 4.1 Mesh configurations and cell counts for all single phase models . 49
Table 4.2 Mesh configurations and cell counts for all hydrodynamics two-phase models 50
Table 4.3 Mesh configurations and cell counts for all hydrodynamics two-phase models 50
Table 4.4 Operating air gas density and viscosity as a function of temperature and F_g. 53
Table 4.5 Constant thermophysical properties used in the two-phase model. Water properties at 25°C and 36°C were computed at atmospheric conditions. 54
Table 4.6 Surface tension values used in the present work. 56
Table 4.7 Binary liquid-phase diffusion coefficients used in the multicomponent (Maxwell–Stefan) model. 57
Table 4.8 Kinetic parameters used for CO_2–MEA reactions. 58
Table 4.9 Other thermodynamic, transport, and model parameters used in the mass-transfer UDF. 59
Table A.1 Fit quality for polynomial surrogates by liquid load L (errors at original digitized points). 123
Table A.2 Operating values used for interpolation at $z = 0.0142\ \mathrm{m}$. 124

ABSTRACT

Numerical Investigation of Hydrodynamics and Mass Transfer in Structured Packing

Volkan TOPALOĞLU

Department of Mechanical Engineering
Master of Science Thesis

Supervisor: Prof. Dr. Hakan DEMİR

Structured packings are central to post-combustion CO_2 capture, yet their microscale hydrodynamics and reactive transport remain difficult to resolve experimentally; high-fidelity computational fluid dynamics (CFD) offers a route to interrogate these scales directly. We develop a representative elementary unit (REU) of Sulzer Mellapak 500.Y and evaluate it in two consecutive parts: hydrodynamics and reactive absorption. In the hydrodynamics part, a single-phase CFD campaign performs a parametric pressure-drop calibration to identify an optimum face-to-face sheet spacing and the required number of stacked REUs. Building on prior analyses of liquid holdup, interfacial area, and static/dynamic wall contact angles, we extend the model to a transient Volume of Fluid (VOF) formulation to resolve film evolution and quantify the wet pressure drop alongside the aforementioned hydrodynamic variables. In the reactive absorption part, CO_2 capture with an MEA (Monoethanolamine) solvent is CFD investigated. Whereas earlier studies often inferred overall mass-transfer coefficients via tracer-based approaches, we demonstrate a fully coupled transient VOF model that embeds gas-liquid mass transfer, liquid-phase reaction kinetics and thermodynamic equilibria to predict the overall mass-transfer coefficient. Simulation outputs for pressure drop, holdup, interfacial area, and overall mass-transfer performance are compared with literature data and exhibit consistent trends and magnitudes. The proposed REU-based framework links packing geometry to hydrodynamic and reactive performance in a physics-resolved manner, providing actionable guidance for packing design, screening, and scale-up.

Keywords: Computational Fluid Dynamics, Structured Packing, Holdup, Interfacial Area, Pressure Drop, Reactive Absorption, Mass Transfer

ÖZET

Yapılandırılmış dolgu malzemelerinde hidrodinamik ve kütle transferinin sayısal olarak incelenmesi

Volkan TOPALOĞLU

Makine Mühendisliği Anabilim Dalı
Yüksek Lisans Tezi

Danışman: Prof. Dr. Hakan DEMİR

Yapılandırılmış dolgular, baca gazı sonrası CO_2 yakalama süreçlerinde merkezi bir rol oynamaktadır; ancak mikroskobik ölçekteki hidrodinamikleri ve reaktif taşınımı deneysel olarak çözümlemek güçtür. Yüksek doğruluklu hesaplamalı akışkanlar dinamiği (HAD), bu ölçekleri doğrudan incelemek için bir yol sunmaktadır. Bu çalışmada Sulzer Mellapak 500.Y için bir temsili elemanter birim (TEB, İng. Representative Elementary Unit, REU) geliştirilmiş ve iki ardışık bölümde değerlendirilmiştir: hidrodinamik ve reaktif absorpsiyon. Hidrodinamik bölümünde, tek fazlı bir CFD çalışması yürütülerek parametre bazlı basınç düşümü kalibrasyonu yapılmış, optimum levha aralığı ve gerekli sayıda üst üste dizilmiş REU sayısı belirlenmiştir. Daha önceki sıvı tutma, ara yüzey alanı ve statik/dinamik duvar temas açıları analizlerine dayanarak model, akışkan film gelişimini çözümleyen ve söz konusu hidrodinamik değişkenlerle birlikte ıslak basınç düşümünü nicel olarak hesaplayan zamana bağlı bir VOF (Volume of Fluid) formülasyonuna genişletilmiştir. Reaktif absorpsiyon bölümünde ise, MEA (Monoetanolamin) çözücüsü ile CO_2 yakalaması incelenmiştir. Önceki çalışmalar genel kütle transfer katsayısını çoğunlukla iz sürücü tabanlı yöntemlerle dolaylı yoldan elde ederken, burada gaz-sıvı kütle transferini, sıvı faz reaksiyon kinetiklerini ve termodinamik dengeleri içeren, birbirine bağlı denklemler ile birlikte zamana bağlı bir VOF modeliyle tahmin gerçekleştirilmiştir. Basınç düşümü, sıvı tutma, ara yüzey alanı ve genel kütle transfer performansı çıktıları literatür verileriyle karşılaştırılmış ve uyumlu eğilimler ve büyüklükler gözlemlenmiştir. Önerilen TEB tabanlı çerçeve, dolgu geometrisini hidrodinamik

ve reaktif performansa fiziksel olarak çözümlemeye dayalı fakat hesaplamalı olarak uygulanabilir bir biçimde bağlamakta, dolgu tasarımı, taraması ve ölçek büyütme için uygulanabilir yol gösterici bilgiler sunmaktadır.

Anahtar Kelimeler: Hesaplamalı Akışkanlar Dinamiği, Yapılandırılmış Dolgu, Sıvı Tutulumu, Ara Yüzey Alanı, Basınç Düşümü, Reaktif Absorpsiyon, Kütle Transferi

1
INTRODUCTION

1.1 Background and Motivation

Distillation is recognized as the most energy-intensive separation process in the production industries, consuming approximately 40% of the total operational energy input [3]. Moreover, research highlights that this significant demand corresponds to nearly 3% of global energy consumption [4]. Today, the performance of distillation column still dominated by the design structural packings. Thus, the capital/operating costs for distillation columns are still dominated by,

- pressure drop that drives blower and compressor power,
- gas-liquid contact for higher gas-liquid mass transfer rate,
- increased column height due higher performance requirement.

With relatively lower capital investment risk, amine-based post-combustion CO_2 capture has emerged as a promising technology, since it can be retrofitted to existing flue gas stacks. In such absorption columns, the contact between the flue gas and the amine solvent is provided by internals designed to maximize interfacial area and minimize pressure drop. Among different type of internals, structured packings—corrugated metal, ceramic, or plastic sheets arranged in a periodic pattern—have been widely adopted at commercial scale. Their geometry offers a high gas–liquid interfacial area while maintaining a low pressure drop, making them especially well-suited for absorption applications.

However, developing novel structured packing designs still remains challenging because performance data from published experimental studies are often hard to extrapolate to new configurations and designs. Lately, high-performance computing (HPC) resources becoming more and more accessible to the researchers. Therefore,

Computational Fluid Dynamics (CFD) studies creates new opportunities to develop the next generation of high-performance structured packings by leveraging HPC infrastructures.

Recently, CFD studies on this topic have attracted attention as shown in the Fig. 1.1 since the publication of the study keywords as "CFD" and "Structured Packing" in the Scopus database.

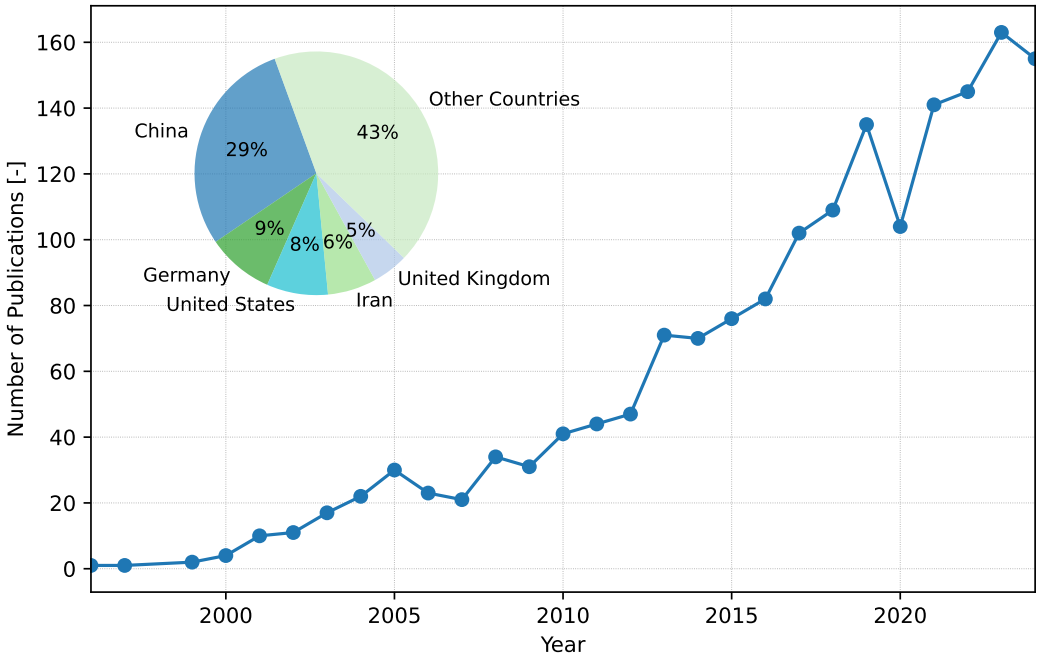


Figure 1.1 Publications about "CFD" & "Structured Packing" keywords per year with pie chart showing the country-wise distribution
[5]

Although the number of publications is increasing year by year, numerical studies have focused on mostly single-phase flow, simplified two-dimensional models, or have neglected mass transfer models and chemical reactions. Given the industrial relevance of CO_2 capture and the geometric complexity of modern packings, developing such a CFD-based simulation framework remains a critical research. Consequently, the literature still lacks reliable two-phase CFD simulations that couple hydrodynamics with reactive absorption. This study addresses that gap by providing a comprehensive CFD-based investigation of hydrodynamics and reactive mass transfer under realistic absorption conditions.

1.2 Internal Configurations in Separation Columns

Separation columns are essential process unit in many chemical processes. It relies on internal components such as packings and trays to enhance mass transfer

between gas-liquid [6–8]. A representative figure has been demonstrated in the Figure 1.2. The distillation or absorption is achieved through repeated gas–liquid contact across internal structures that enhance mass transfer. As shown in the Figure 1.2, the liquid phase flows downward, while the gas phase rises countercurrently within the column. The liquid-gas contact requires better contact to increase mass transfer between phases. To achieve this, different types of column internals have been used in the process industry.

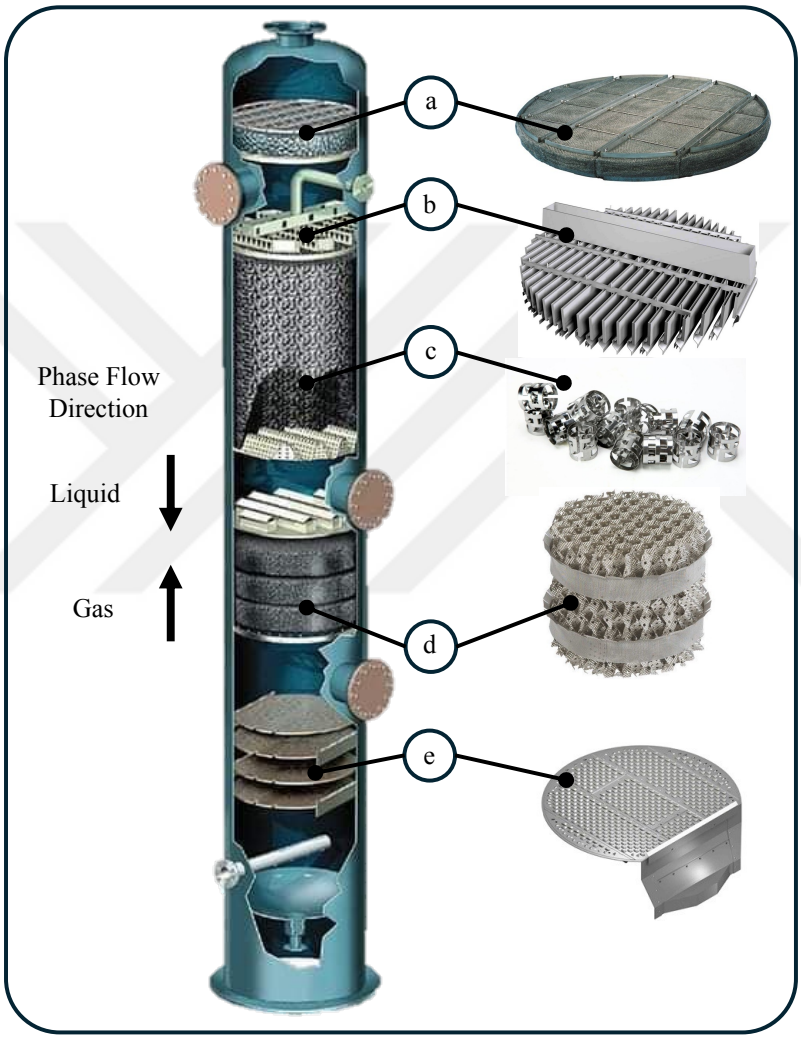


Figure 1.2 Internals of the column: (a) mist eliminator, (b) liquid distributor, (c) random packings, (d) structural packings, and (e) trays [9]

To illustrate this, a mist eliminator (Figure 1.2a), used to eliminate liquid droplets leaving the column in the gas (or vapor) stream. Liquid distributors are used to distribute the liquid over the stage below (Figure 1.2b). Mist eliminators and liquid distributors generally have negligible efficiencies in the separation processes. To enhance mass transfer three main types of internals are used as follows,

- **Random packings**: These are mass transfer elements that are randomly poured into the section of the column, allowing for vapor–liquid contact in a non-structured manner (Figure 1.2c).
- **Structured packings**: Representing the primary focus of this study, structured packings typically offer higher mass transfer efficiency compared to both trays and random packings due to their organized geometry (Figure 1.2d).
- **Trays**: In trays, the rising gas passes through perforations in the tray (holes or special designed valves) and interacts with the liquid phase. The liquid flows across the tray and descends through downcomers to the tray below (Figure 1.2e).

1.3 Research Problem and Hypothesis

Structured packings require higher number of cells to be computed in numerical modeling due to its complex geometry. With the help of its organized structure of structural packings, Representative Elementary Unit (REU) approach could be used to tackle computational limits [10–15]. In this study REU-based approach is employed to simulate both single-phase gas flow and two-phase liquid-gas flow. The two-phase liquid-gas flow is extended with a mass transfer model to observe how accurate the selected model.

Two different modeling strategies were adopted to serve different validation and prediction goals, as shown in Figure 1.3 and Figure 1.4. In the Figure 1.3, six-periodic REU's is employed to calibrate the model, dimensions and turbulence settings

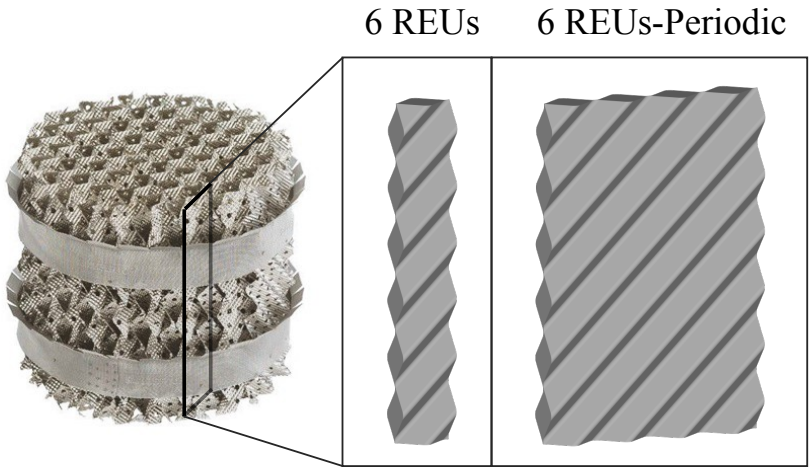


Figure 1.3 6-REU model used for single-phase dry-gas pressure-drop calibration.

Moreover, in the Figure 1.4, single-periodic REU is employed to conduct the two-phase liquid-gas flow. This system is extended with mass transfer model for capturing CO_2.

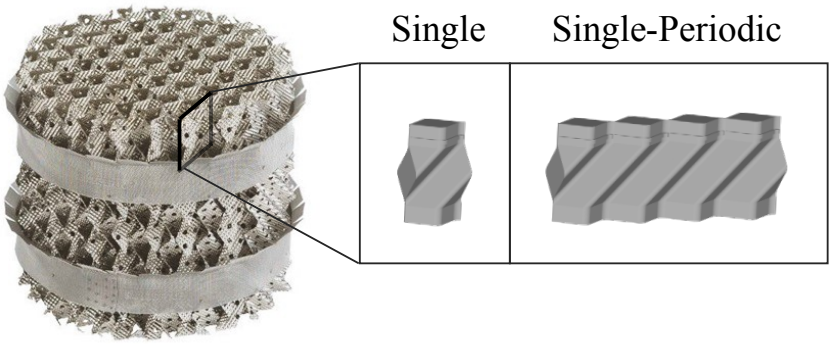


Figure 1.4 Single REU used for reactive two-phase hydrodynamics and mass transfer modeling.

In other words, these two approaches enable the separation of numerical challenges. While the six-REU model is used to match experimental pressure-drop data [2, 16], the single REU cell is used to perform high-resolution two-phase simulations including hydrodynamics [10], interfacial mass transfer and reactions.

Problem Statement: Once calibrated in a six-REU dry-gas configuration, could a CFD model based on a single REU geometry be reliably extended to simulate hydrodynamics, wet pressure drop, interface area, and reactive mass transfer in structured packings? Thus, following points are the problem statement of this study:

- What are the accuracy range of REU-based modeling for predicting dry-wet ΔP, liquid holdup, $K_G \times a_e$, interfacial area in structured packing?
- How do phase-interface tracking and static/dynamic contact angle modeling impact the interfacial area?
- How accurate CFD-based single-REU reactive absorption rate compared with literature based experimental study by incorporating mass transfer models?

Hypothesis: If turbulence model carefully tuned in a calibrated dry-gas simulation in six-REU's, then a high-resolution single REU model can predict:

(a) the dry-gas pressure-drop behavior [2, 16],

(b) two-phase hydrodynamic conditions varying gas/liquid flow rates such as: liquid holdup, wet pressure drop and phase interfacial area [2, 15, 17, 18].

(b) the overall $\mathrm{CO_2}$ mass transfer performance [19–21].

1.4 Objectives and Scope

Below in the Table 1.1 objective of the research is given including the success metrics and motivation:

Table 1.1 Research objectives

#	Objective	Motivation & Metrics
O1	Calibrate dry pressure drop in a CFD framework for single-phase gas flow using Sulzer Mellapak 500.Y. structural packing model.	The validated dry pressure drop model could be a ground for two phase hydrodynamics and reactive absorption study. Validation criterion: predicted $\Delta P/\mathrm{m}$ within $\pm 20\%$ of experimental data.
O2	Quantify liquid hold-up, wet pressure drop, and interfacial area under counter-current and varying gas–liquid flow.	These hydrodynamic parameters govern mass transfer efficiency. Compare CFD results with reliable literature correlations and experiments for h_L, $\Delta P/\mathrm{m}$ and $a_{\mathrm{if}} = f(G, L, \theta)$.
O3	Integrate an MEA–$\mathrm{CO_2}$ absorption model into the CFD and evaluate overall mass transfer rates.	Solving hydrodynamics with mass transfer in CFD study would enable close observation to local mass transfer effects in Structural Packing. Validation: incorporate mass transfer correlation with $K_G a_e$ experimental study and/or pilot-plant data.

Table 1.2 provides understanding approach to the study and the scope of the thesis and the out of scope points,

Table 1.2 Scope and assumptions

Aspect	In Scope	Assumptions & Out of Scope
Packing Geometry	Sulzer Mellapak 500 Y; periodic REU's.	Other type of structured or random packings; sheet surface embossing (modelled as smooth with equivalent contact-angle).
Flow Regime	Counter-current air/water at 25 °C or air/CO_2–MEA at 36 °C, 1 atm; gas F-factor 0.3 – 4.5 $Pa^{0.5}$; liquid load 3.8 – 75.0 $m^3\ m^{-2}\ h^{-1}$.	Foaming, flooding and other type of solvents.
Physical Models	SST $k-\omega$ for turbulence model; VOF for interface capturing; pseudo-first-order CO_2 absorption kinetics.	LES/DNS; degradation chemistry of MEA; inert-gas solubility.
Validation Data	Experimental studies and correlations used from literature.	Lab/pilot experimental studies conducted for this study.
Scale Bridging	REU geometry.	Full-scale column study.

1.5 Organization of the Thesis

Chapter 2 – Literature Review: Experimental and modeling studies on structured packings, CFD methodologies for single-phase flow, two-phase flow, and reactive CO_2 absorption and other type of studies on separation processes.

Chapter 3 – Theoretical Background: General knowledge of equations which are used for hydrodynamics and reactive absorption.

Chapter 4 – Computational Methodology: Geometry, mesh, governing equations, turbulence models, boundary conditions, and phase-interface discussed. Further, determination of property modeling explained. The developed framework (methodology) and UDF implementation for Reactive Absorption was also discussed in this chapter.

Chapter 5 – Results & Discussion: Parametric results of the work: Model calibration by validating single phase pressure drop. Literature comparison/validation with two-phase hydrodynamics and reactive absorption.

Chapter 6 – Conclusions: Key findings, outlook, contribution to the literature, limitations and recommendations for future research.

2
LITERATURE SURVEY

2.1 Hydrodynamics

2.1.1 Experimental

As reported in [2],the liquid hold-up in three metal-sheet structured packings—Mellapak 250.X, 250.Y, and 500.Y—using an air/water system in a 1-meter diameter column and a γ-ray absorption technique that captures total holdup. They mapped holdup across wide liquid loads (5–200 $m^3m^{-2}h^{-1}$) and gas loads (expressed as the F-factor) and showed that, below the loading point, holdup remains almost constant with gas velocity, but rises sharply when gas–liquid interaction increases. This phenomena generally explained as a regime, namely "flooding". They reported the liquid hold-up in Mellapak structured packings was measured as a function of gas load and liquid load in their work. As illustrated in Figure 2.1, the structured packing layers are arranged in a cross-channel pattern that enhances liquid redistribution between packing sheets. Below the loading point, the holdup profile remains stable, while above it, liquid accumulation increases sharply at the layer intersections, indicating the onset of the flooding regime. Analysis at zero gas flow revealed two liquid-load regimes (≤ 40 and $> 40 m^3m^{-2}h^{-1}$) with exponents 0.37 and 0.59, respectively; incorporating packing surface area ($a_p^{0.83}$) and viscosity ($\mu_L^{0.25}$) led to a correlation predicting holdup within $\pm 10\%$ for all Mellapak structural packing types [2]. Since the study investigated the holdup for Mellapak 500.Y as a function of the F-factor at several liquid loads, therefore the study is found to be a good candidate as robust experimental baseline. Thus their study is used as an experimental baseline for the current study. Following correlation as reported in [2] predicts the liquid holdup h_L as a function of the packing-specific surface area a_p, the liquid load L, and the viscosity ratio $\mu_L/\mu_{L,0}$, using empirically determined exponents and coefficient c. for $L > 40$, $x = 0.59$ and $c = 0.0075$; $L < 40$; $x = 0.37$, $c = 0.0169$.

$$h_L = c\, a_p^{0.83}\, l^x \left(\frac{\mu_L}{\mu_{L,0}}\right)^{0.25} \tag{2.1}$$

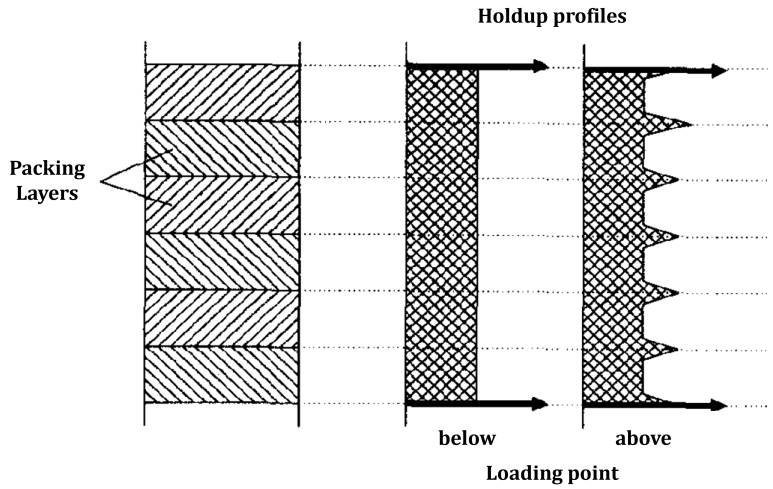


Figure 2.1 Schematic packing layers and holdup profiles below and above the loading point (Adapted from [2])

Experimental investigation was conducted for Montz-pak B1-250 corrugated-sheet structured packing using an air–water system at ambient conditions to the columns of 0.192 m, 0.45 m, 0.8 m, and 1.4 m internal diameter in order to experiment how the column size affects pressure drop and capacity. The packing consisted of non-perforated metal sheets at a 45° angle and was equipped with wall-wiper rings and narrow pit liquid distributors. Measurements of dry and wet pressure drop versus F-factor were measured to the flooding point by using calibrated flowmeters along with a U-tube manometer. It was observed that pressure drop increases and capacity decreases become significant as column diameter approaches packing element height, with the diameter effect pronounced below about 1 m and stronger under wet conditions, implying that scale-up from small-diameter data can lead to overestimation of pressure drop and oversizing of industrial columns. The Delft Overall Performance Model, which partitions pressure losses into gas–liquid, gas–gas, and direction-change components, captured the diameter effect reasonably well but failed to predict the shift in loading point. [22]

Olujic reported that they developed a geometry-based model for corrugated-sheet structured packings that predicts liquid hold-up, h_L, simply as the product of packing surface area, a, and mean film thickness, d, which is estimated via a Nusselt-type falling-film expression adapted to the corrugation angle [23]. They confirm experimentally that in the preloading regime, hold-up is essentially independent of gas load and correlates well with liquid load through so that increasing L yields thicker films and leading to a larger h_L.

$$h_L \;=\; a\left[\frac{3\,\mu_L\,u_L}{\rho_L\,g\,a\,\sin\alpha}\right]^{\frac{1}{3}} \tag{2.2}$$

Billet-Schultes [1] correlations are validated for countercurrent gas–liquid columns with both random (dumped) and structured (arranged) packings across >3,500 data points, >50 systems, and >70 packing types. Their correlations are applicable over gas capacity factors $F_G = u_G\sqrt{\rho_G}$ spanning 0.003–$5.09\ \mathrm{Pa}^{1/2}$ and liquid loads L spanning 0.256–$144\ \mathrm{m^3\,m^{-2}\,h^{-1}}$. As reported by [1], the liquid holdup correlation was given as follows:

$$a_P = 250\ \mathrm{m^2/m^3}, \quad C_h = 0.554\ (For\ Mellapak\ 250.Y.) \tag{2.3}$$

$$h_{\mathrm{th}} = \left(\frac{12\,\mu_L\,u_L\,a_P^2}{g\rho_L}\right)^{1/3} \tag{2.4}$$

$$\mathrm{Re}_L = \frac{\rho_L\,u_L}{a_P\,\mu_{L,\mathrm{other}}}, \qquad \mathrm{Fr}_L = \frac{u_L^2\,a_P}{g}, \frac{a_h}{a_P} \tag{2.5}$$

$$\frac{a_h}{a_P} = \begin{cases} C_h\,\mathrm{Re}_L^{0.15}\,\mathrm{Fr}_L^{0.10}, & \mathrm{Re}_L < 5, \\ C_h^{0.85}\,\mathrm{Re}_L^{0.25}\,\mathrm{Fr}_L^{0.10}, & \mathrm{Re}_L \geq 5, \end{cases} \tag{2.6}$$

$$h_{\mathrm{L}} = h_{\mathrm{th}}\left(\frac{a_h}{a_P}\right)^{2/3} \tag{2.7}$$

According to [24], X-ray computed tomography (CT) was used to generate a digital replica of half-elements of plastic Sulzer Mellapak 250.Y structured packing (perforated, wiper-banded, surface-enhanced; $a_p = 250\ \mathrm{m^2/m^3}$). Adaptive polyhedral meshing was applied to create CFD-ready models in STAR-CCM+ on a 544-core HPC system employing a two-layer realizable k–ε turbulence model. Simulations covered F-factors between 0.61 and 3.36 $\mathrm{m/s}\cdot(\mathrm{kg/m^3})^{1/2}$, mirroring randomized, triplicate single-phase nitrogen experiments for pressure-drop validation. On average, nitrogen CFD under-predicted experimental data by $\approx 7\%$, whereas water simulations at equivalent Reynolds numbers under-predicted by $\approx 40\%$, discrepancies attributed to geometry deviations introduced during sample preparation [24].

As reported in [25], a CFD study was conducted to characterize the hydraulic performance of structured packing under both single-phase and gas–liquid flow conditions. The Mellapak 250.Y geometry was reconstructed via X-ray CT and meshed with prism layers to resolve near-wall effects. Single-phase nitrogen flow through a three-element bed was validated against experimental pressure-drop

data, with deviations below 15% and reduced to $\approx 7\%$ when prism layers were employed [25]. Subsequently, periodic REUs of the packing featuring variations in channel corrugation angle, opening angle, and side length, were simulated across a range of F-factors. Multiphase flow was modeled using the Volume-of-Fluid (VOF) approach for both small-scale REUs and the CT-derived geometry. Transient simulations initialized with a uniform liquid film and tracked liquid holdup, wetted area, and irrigated pressure drop under varying liquid density, viscosity, surface tension, and static contact angle.

Figure 2.2 illustrates the effect of prism layer count on liquid holdup and wetted area (Adapted from [25]). The upper plot shows that liquid holdup increases with liquid load across 10, 15, and 20 prism-layer meshes, while the lower plot indicates that the fractional wetted area correlates positively with holdup, approaching complete wetting at higher liquid loads.

As illustrated in Fig. 2.3, the effect of contact angle on liquid spreading and film distribution was investigated (Adapted from [25]). For a perfectly wetting surface ($\theta_{wall} = 0°$), the liquid film uniformly coats the structured surface, resulting in a high fractional wetted area ($a_f = 0.80$) and moderate holdup ($h_L = 6.6\%$) at a liquid load of $46\ \mathrm{m^3/m^2\text{-}hr}$. Increasing the contact angle to $30°$ reduces surface adhesion, leading to thinner liquid films and a decrease in wetted area ($a_f = 0.48$), while maintaining similar holdup levels. At a hydrophobic condition of $75°$, liquid pathways become more discontinuous and channelized, corresponding to a further reduction in a_f to 0.27 despite higher liquid load ($L = 94\ \mathrm{m^3/m^2\text{-}hr}$). These results indicate that increasing contact angle significantly impedes film spreading and surface wetting, making θ_{wall} a dominant parameter in predicting wetted-area behavior.

In transient simulations, Basden reported [25] that the contact angle proved to be the dominant factor governing wetted area prediction, while irrigated pressure drop and holdup were substantially over-predicted throughout the study.

Rocha et al. developed a mechanistic hydraulic model for distillation columns packed with corrugated sheet structured packings, treating each flow channel as a wetted-wall column and defined effective gas and liquid velocities and gravity to couple liquid holdup, pressure drop, and flooding in a unified framework. Static and operating holdup are predicted via modified falling-film correlations, and irrigated and dry pressure drops are linked through a channel-based friction-factor approach. The model was validated against extensive air-water data (gas velocities 0.0068–$4.367\ \mathrm{m/s}$) on packings such as Flexipac, Gempak, Sulzer BX, and etc.,

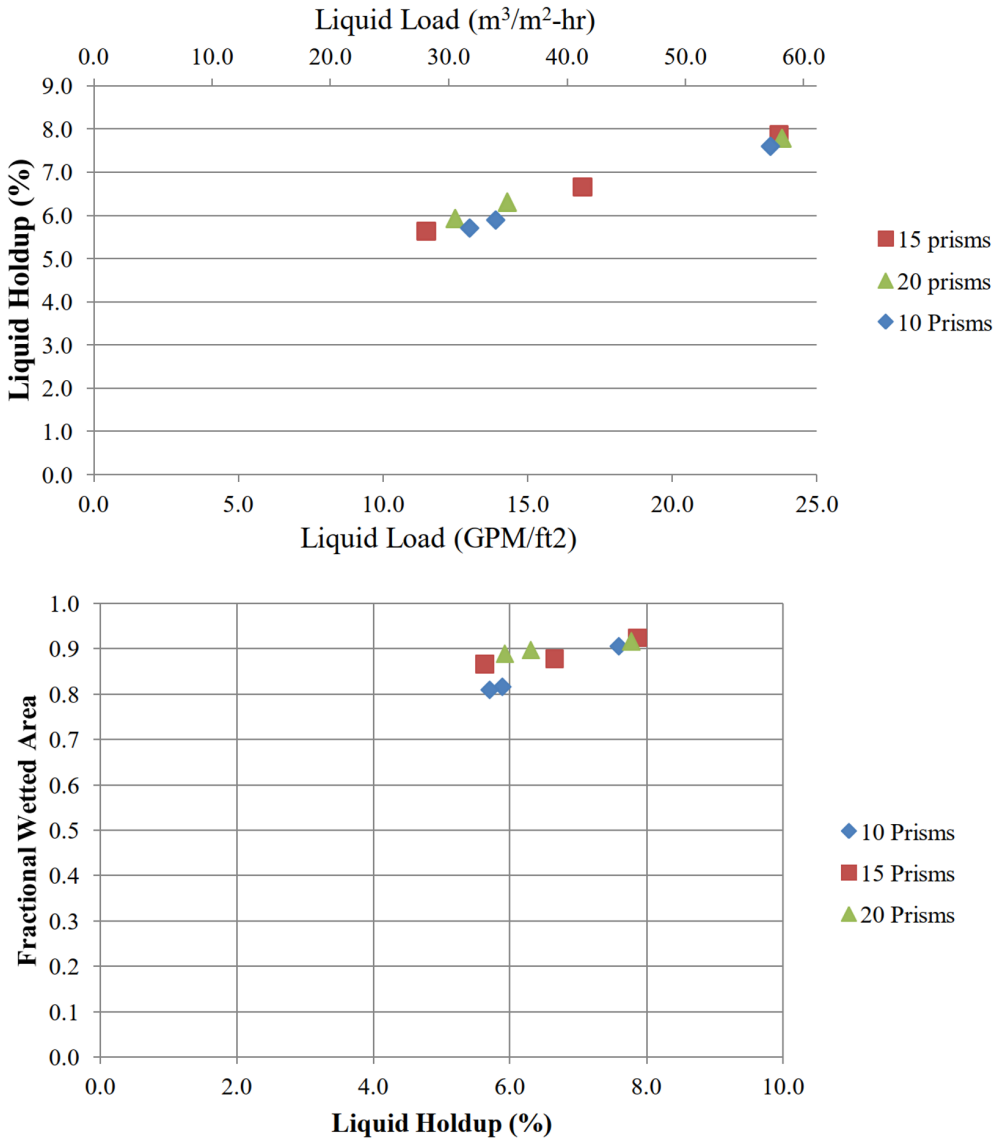


Figure 2.2 Liquid holdup (%) and wetted area as function of the number of prism layers [25].

and further tested in cyclohexane/n-heptane distillations at 0.33-4.14 bar with a good agreement. [26]

The effective interfacial area a_{ph} is predicted according to the correlation proposed by Billet and Schultes [27], which relates it to the geometric surface area a of the packing. For absorption and desorption processes under neutral or positive wetting conditions, the ratio was given:

$$\frac{a_e}{a_p} = C_L \left(a_p\, d_h\right)^{-1/2} \mathrm{Re}_L^{1/6}\, \mathrm{Sc}_L^{-1/2} \tag{2.8}$$

$$d_h = \frac{4\,(1-\varepsilon)}{a_p} \tag{2.9}$$

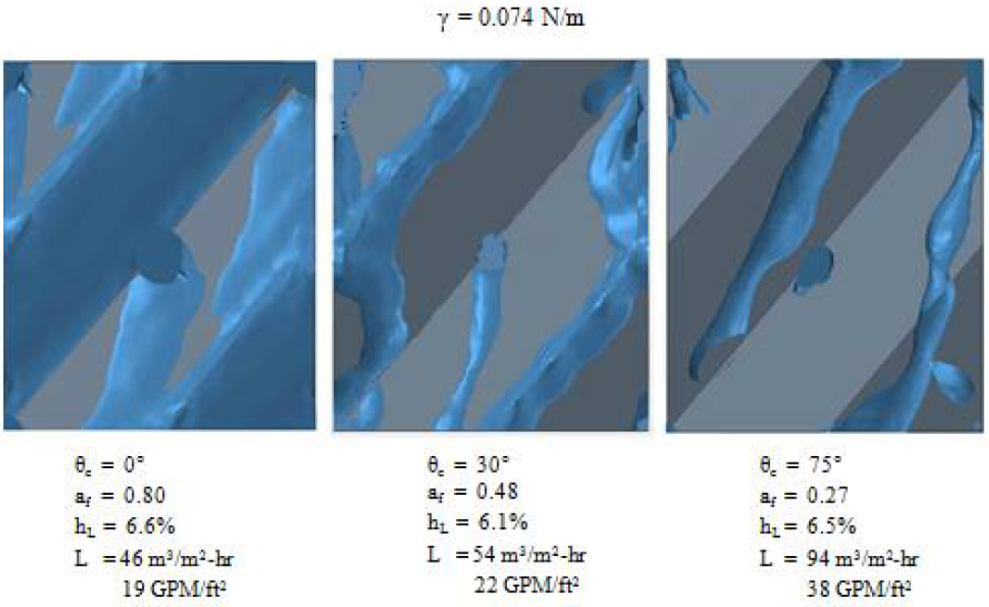


Figure 2.3 Effect of contact angle (θ_{wall}) on liquid film distribution (Adapted from [25])

$$a_e = 1.34 \left[\frac{\rho_L}{\sigma} g^{1/3} \left(\frac{Q}{L_p} \right)^{4/3} \right]^{0.116} a_p \tag{2.10}$$

In [16], the effective mass-transfer area of nine commercial structured packings (M250.Y, M500.Y, M250.X, MP252.Y, M250.YS, M125.Y, M2.Y, F1.Y, and P500) was determined by chemical absorption of CO_2 from ambient air into 0.1 mol L^{-1} NaOH in a 0.427 m ID packed column. Prior to packing tests, CO_2–NaOH reaction kinetics were measured in a wetted-wall column to decouple mass-transfer coefficients. In the packed-column studies, liquid load was varied from 2.5 to 75 $m^3\,m^{-2}\,h^{-1}$, superficial gas velocity was ranging from 0.6 to 2.3 m s^{-1}, liquid viscosity from 1 to 15 mPa s (utilizing POLYOX WSR N750), and surface tension from 72 to 30 mN m^{-1} (utilizing TERGITOL NP-7). Following the Fig. 2.4-a, the photograph illustrates the experimental absorption column used, while the schematic 2.4-b depicts the overall process configuration of the absorption system.

Furthermore, they observed that the fractional area increased by approximately 10% when the surface tension was reduced. A global correlation for the fractional area, a_e/a_p, as a function of $(\mathrm{We}_L)(\mathrm{Fr}_L)^{-1/3}$ (incorporating liquid density, surface tension, gravity, and flow rate per wetted perimeter) represents the entire database within $\pm 13\%$.

In Figure 2.5, several literature correlations for the fractional wetted area $(a_\mathrm{e}/a_\mathrm{p})$ are compared as a function of liquid load under identical model conditions

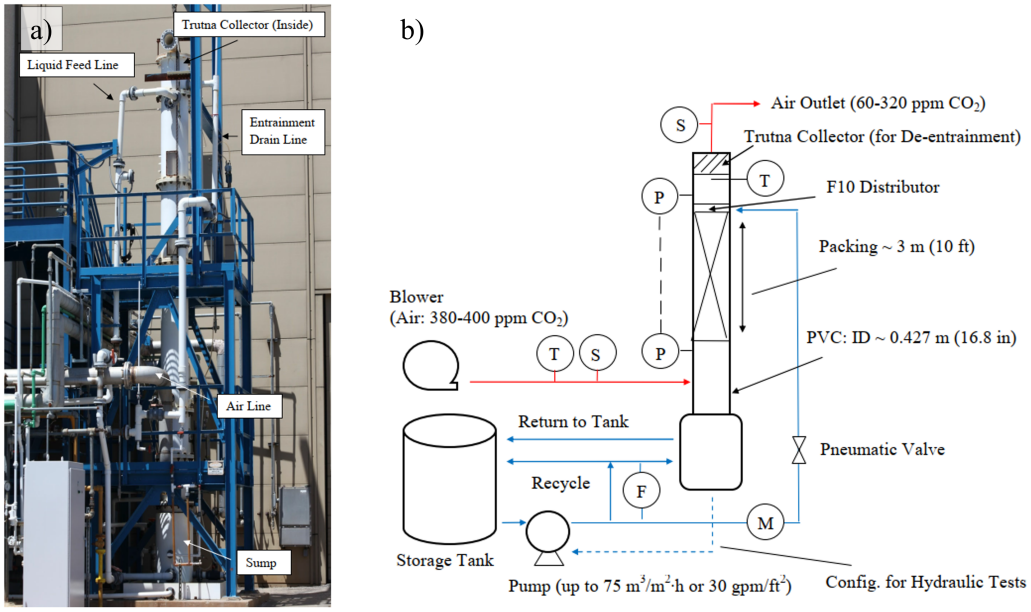


Figure 2.4 Experimental absorption column used and overall process configuration of the system [16].

(ρ_L, μ_L, σ), together with his own correlation and corresponding experimental data, which provide an intermediate prediction between the existing models [16].

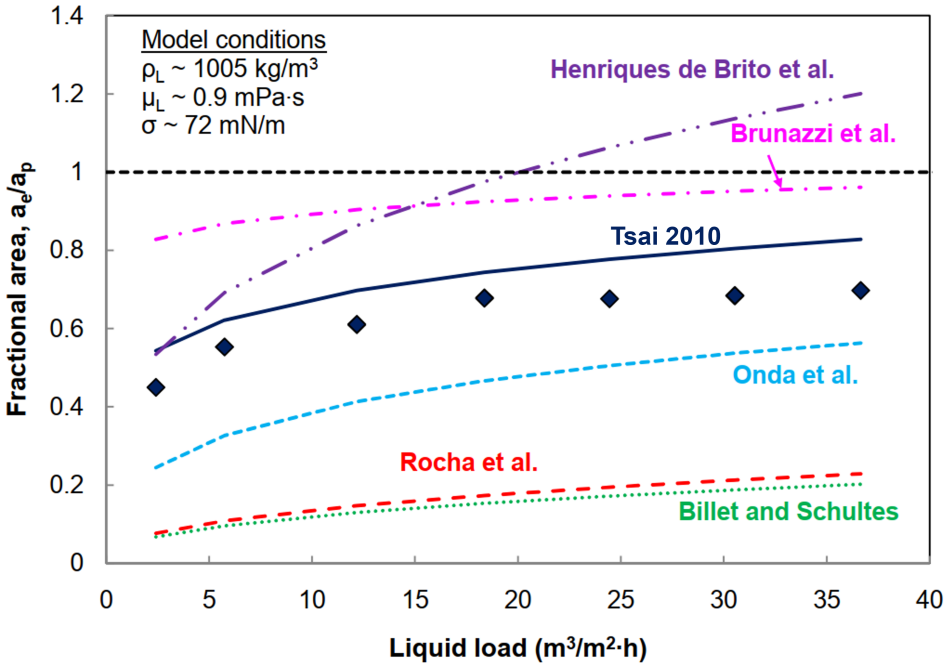


Figure 2.5 Comparison of fractional area correlations for Mellapak 500.Y reported by [16] with respect to the liquid load [16, 26–29].

Tsai [16] summarized the packed bed type hydraulics model of Stichlmair et al.[30] to predict irrigated pressure drop in packed columns. For Mellapak 500.Y, Tsai

reported the packing specific constants as $C_1 = 12.14$, $C_2 = -0.30$, and $C_3 = 0.49$ [16]. The dry pressure drop per unit packed height is [16]:

$$\frac{\Delta P_{\mathrm{dry}}}{Z} = f_0 \left(\frac{1-\varepsilon}{\varepsilon^3} \right) \frac{\rho_G u_G^2}{d_p} \tag{2.11}$$

$$f_0 = \frac{C_1}{Re_G} + \frac{C_2}{\sqrt{Re_G}} + C_3 \tag{2.12}$$

The wet to dry pressure drop ratio is correlated with the total liquid holdup h_L [16, 30]:

$$\frac{\Delta P_{\mathrm{wet}}}{\Delta P_{\mathrm{dry}}} = \left[\frac{1 - \varepsilon \left(1 - \dfrac{h_L}{\varepsilon} \right)^{\frac{2+c}{3}}}{1-\varepsilon} \right]^2 \left(1 - \frac{h_L}{\varepsilon} \right)^{-4.65}, \tag{2.13}$$

with [16]:

$$c = \frac{-\dfrac{C_1}{Re_G} - \dfrac{C_2}{2\,Re_G^{0.5}}}{f_0}. \tag{2.14}$$

Below loading, the holdup is [16]:

$$h_0 = 0.555\, N_{Fr}^{1/3}, \qquad N_{Fr} = \frac{u_L^2 a_p}{g\, \varepsilon^{4.65}}, \tag{2.15}$$

and above loading it is coupled to pressure drop [16]:

$$h_L = h_0 \left[1 + 20 \left(\frac{\Delta P_{\mathrm{wet}}}{Z\, \rho_L\, g} \right)^2 \right]. \tag{2.16}$$

Equations (2.13) and (2.16) are solved by iteration until ΔP_{wet} converges; the result is reported as $\Delta P_{\mathrm{wet}}/Z$.

Brito et al. determined the effective interfacial area a_e of structured packings (e.g., Mellapak 125.Y/250.Y/500.Y) using a reactive absorption method with the fast pseudo–first-order system $\mathrm{CO_2} + \mathrm{NaOH}$ in a pilot column (inner diameter $\approx 295\,\mathrm{mm}$, packed height $\approx 420\,\mathrm{mm}$, liquid distributor density $\approx 527\,\mathrm{orifices/m^2}$). They correlated a_e to the specific geometric area a_p with the liquid Reynolds number:

$$\frac{a_e}{a_p} = 0.465\, \mathrm{Re_L}^{0.30} \tag{2.17}$$

$$\mathrm{Re_L} = \frac{\rho_l\, u_L\, d_h}{\mu_L} \tag{2.18}$$

Their experimental results showed that with the help of the wave formation, rivulets, and droplet entrainment, the measured a_e can exceed a_p under certain hydrodynamic conditions. [29]

As reported in [18], they employed high-resolution X-ray computed tomography to capture 3D images at 31 equal distance heights in columns packed with structured packings (Mellapak 500.Y and Raschig SuperPak350Y, each with various surface modifications) and random packings (Raflux rings, RMSR, and Raschig Super-Rings). In 2.6, a 3D view of the Mellapak 500.Y structured packing with the water/air system at a liquid load of 28 $\mathrm{m^3\,m^{-2}\,h^{-1}}$ without counter-current air flow was shown [18].

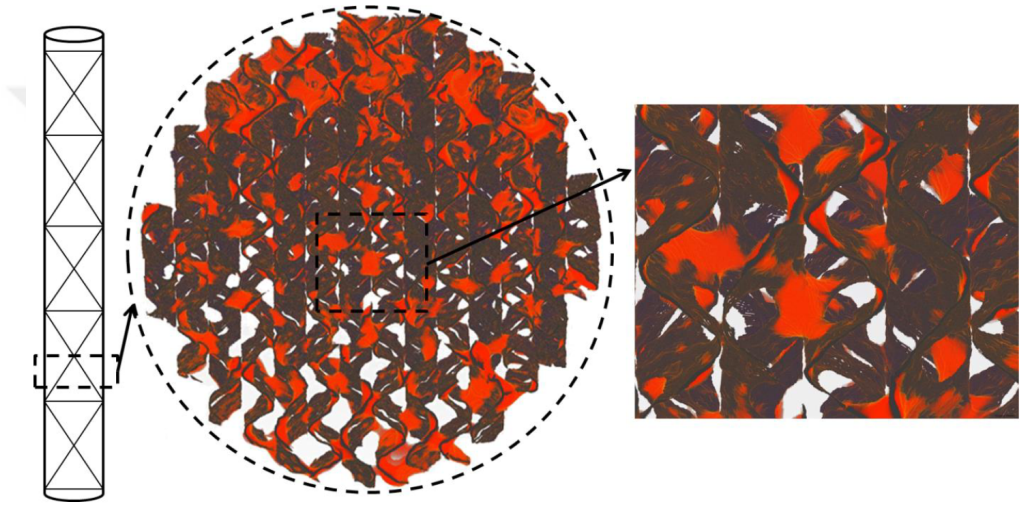


Figure 2.6 3D view of Mellapak 500.Y (30 mm); water/air, 28 $\mathrm{m^3\,m^{-2}\,h^{-1}}$; packing (gray), liquid (red-orange)[18].

Experiments conduct liquid loads from 2 to 70 $\mathrm{m^3\,m^{-2}\,h^{-1}}$ and gas loads (F-factor) up to 2 $\mathrm{Pa^{0.5}}$, using water/air, isopropanol, and dichlorobenzene at a constant 20 °C. The results reveal pronounced axial and radial variations in holdup, quantify partial wetting of packing surfaces, demonstrate non-uniform liquid-film thickness with rivulet-dominated flow, and isolate mass-transfer areas that diverge from literature-based predictive models. The Figure 2.7 shows liquid holdup profiles along the height of a Mellapak 500.Y under different liquid loads ($B = 7,\ 21,\ 42\ \mathrm{m^3\,m^{-2}\,h^{-1}}$). The holdup increases with liquid load and exhibits local maxima near the junctions of the packing elements, where liquid accumulation occurs.

Wehrli employed X-ray computed tomography (CT) to investigate liquid distribution, holdup, and specific interfacial area in Mellapak 500.Y and 250.Y structured packings. Three-dimensional datasets obtained via 2D and helical 3D scans in columns of 100 mm and 200 mm inner diameters, using water and

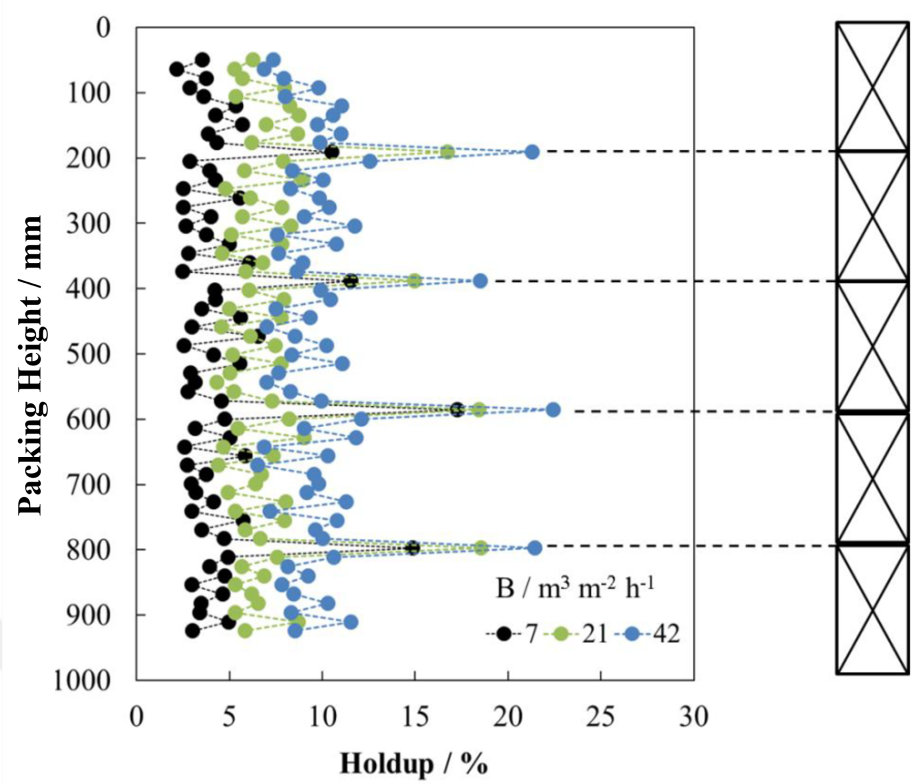


Figure 2.7 Holdup values along the packing height with the water/air system without counter-current gas flow (Adapted from [18]).

isopropanol, demonstrated that experimental studies from the smaller column could be transferred to the larger columns. Average holdup values agreed well across both diameters, while geometric scaling based solely on line load failed; the lower-specific-area 250.Y packing exhibited higher holdup and interfacial area at the same line load, indicating superior wetting characteristics. Flow morphology images revealed that liquid in 500.Y formed rivulets and bridges within narrow channels, whereas 250.Y achieved a more uniform film coverage. These results highlight the critical influence of packing geometry on flow dynamics and underscore the limitations of simple similarity relations[17].

In Figure 2.8, they illustrated the liquid distribution patterns within Mellapak 500.Y and 250.Y packings at half height of the fourth element under a liquid load of $L = 20\ \mathrm{m^3/m^2h}$ and no gas flow. The images reveal that holdup is predominantly concentrated along the contact lines between adjacent corrugations, with more pronounced accumulations occurring at the intersection points of the sheets. Comparison between water and isopropanol demonstrates that the latter, due to its lower surface tension, promotes thinner films and more extensive rivulet formation. The localized regions of intensified holdup, indicated in the magnified

view, correspond to liquid films, rivulets, and bridges that form preferentially at the sheet junctions [17].

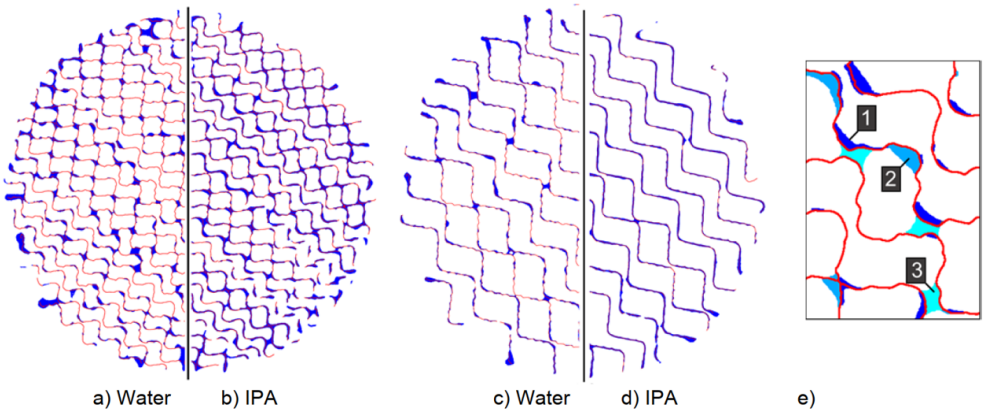


Figure 2.8 Representative CT images of packing element for $B = 20\ \mathrm{m}^3/\mathrm{m}^2\mathrm{h}$ and $F_g = 0$. (a,b) Mellapak 500.Y with water and isopropanol, respectively; (c,d) Mellapak 250.Y with water and isopropanol. (e) Examples of liquid films (1), rivulets (2), and bridges (3) are highlighted. [17]

2.1.2 Numerical

Isoz carried out the study to assess the performance of the structural packing. In the study, Sulzer's Mellapak 250.X, 250.Y, 350.Y and 500.Y. structural packings were used. He, N2 and SF6 chemicals were used as service for gases. It was studied in a broad gas flow range (Re: 100-10,000) [31]. The relationship between dry pressure loss and gas flow was examined. These can be listed as follows:

- inclination of the packing channels to the horizontal plane,
- specific area of the packing,
- perforation density of the packing.

In their study, geometry was generated in Blender and simulations were conducted in OpenFOAM using the steady-state RANS equations with SST $k-\omega$ turbulence model. The study revealed that one packing element is generally sufficient to predict the dry pressure drop across a column, as inter-element transition effects were minor. In the study, unstructured hexahedral meshes with local refinement down to 2 mm near walls was used. Experimental validation used ethanol manometry and calibrated orifices in a 150 mm i.d. column, measuring ΔP_{dry} for He, N_2, and SF_6 over Reynolds numbers (Re) of 10^2–10^4. The model automates geometry creation and meshing, enabling rapid parametric studies of channel angle (α_{ch}), specific area density (a_G), and perforation spacing (a_{pr}) [31].

The illustration (Fig. 2.9) reveals cellular vortices that repeat along the main flow direction inside corrugated structured packing. Streamlines colored by speed and pressure colored slices expose the spatial organization of these vortical cells [31].

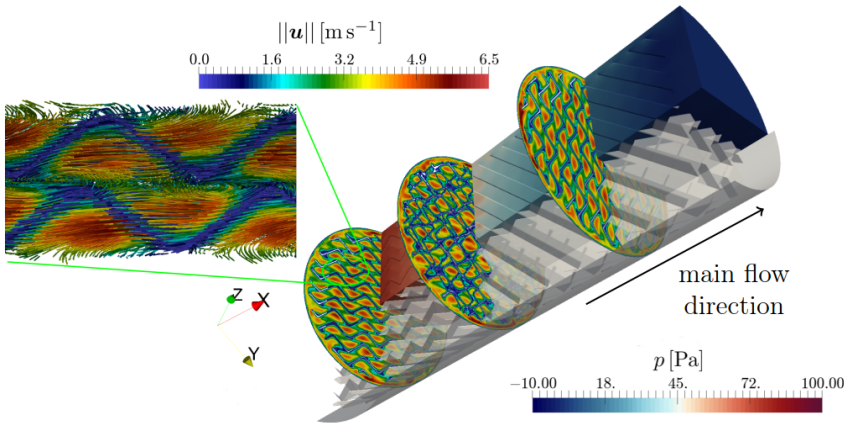
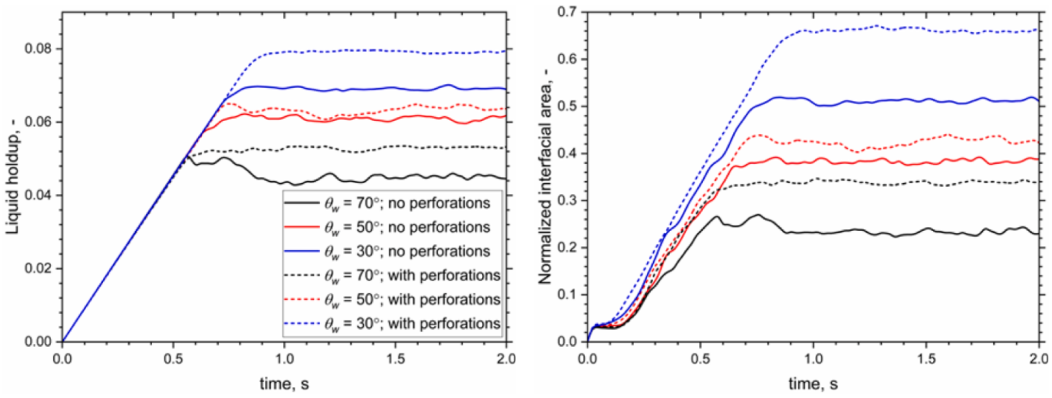


Figure 2.9 Three dimensional flow in a corrugated packing channel with streamlines colored by velocity and cross sections colored by pressure. Adapted from [31]

In Ambekar et al.'s study, the authors performed structure-resolved two-phase simulations of gas–liquid flow through periodic REUs of Sulzer Mellapak 250 structured packing using the Volume-of-Fluid (VOF) method in OpenFOAM v6. They created detailed computational domains both with and without 4 mm perforations on corrugated sheets (base 26.7 mm, height 12 mm, corrugation angle 45°), meshing each with 1.8–3.7 million cells (refined around perforations) to ensure grid independence. Simulations covered inclination angles β = 45° and 90°, liquid loads u_L = 31, 62, 110 m³/m²·h, and static contact angles θ_{wall} = 30°, 50°, 70°. Their results show that perforations promote flow separation and droplet formation, increasing liquid holdup, interfacial area, and wetted area across all conditions. Lower θ_{w} or higher liquid viscosity transitions flow from droplets toward a full-film regime, enhancing connectivity and wetted coverage [11].

Their study [11] showed that explicitly modeling sheet perforations increases wetting prediction and yields higher liquid holdup and normalized interfacial area for all examined contact angles, as seen in Fig. 2.10. Accounting for perforations therefore improves the realism of the CFD predictions.

Ataki and Bart investigated the three-dimensional wetting behavior of a single element of Rombopak 4M structured packing by integrating experimental dye-flow visualization and CFD simulations. Experimentally, they observed liquid rivulet formation and bridging on a multi-element sheet under superficial liquid loads of



(a) (b)

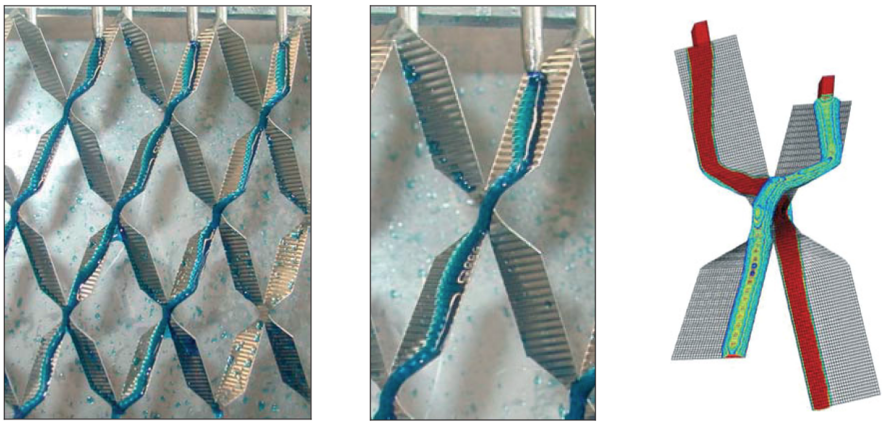
Figure 2.10 Effect of sheet perforations on transient liquid holdup (a) and normalized interfacial area (b) for static contact angles 30°, 50°, and 70° (Adapted from [11]).

12.8–51.2 m^3/m^2h (20.9–83.6 mL/min per plate). Numerically, they generated the geometry in GAMBIT and performed transient VOF simulations in FLUENT (6.2) using the continuum surface force model for surface tension, constant static contact angles, laminar flow, and a segregated solver with time steps of 1×10^{-5}–5×10^{-5} s, first-order upwind and body-force weighted schemes. Mesh independence was ensured across grids ranging from 35,330 to 268,112 hexahedral cells to accurately resolve thin liquid films and rivulet profiles. The CFD results closely matched the experimental wetting patterns, demonstrating that higher viscosity and lower contact angles increase wetting degree, interfacial area, and liquid holdup. From the simulations, they derived empirical correlation which is given as following equation [12],

$$\frac{a_h}{a_p} = 1.279\,\mathrm{Fr}_L^{0.044}\,\mathrm{We}_L^{0.243}\,\mathrm{Re}_L^{0.0266}\,(\cos\theta_{wall})^{0.927} \tag{2.19}$$

In Figure 2.11, experimental and CFD views of rivulet flow on structured packing are contrasted at 53.8 and 41.8 mL/min, with Figure 2.11-b providing a close up of Figure 2.11-a [12].

Bertling et al. employed high-resolution CFD simulations using the VOF method to investigate gravity-induced liquid flow and tracer transport in two types of Mellapak structured packings (250 m^2/m^3 and 500 m^2/m^3). The computational domain consisted of seven REUs between adjacent corrugated sheets (22.2 cm tall for 250Y and 11.1 cm for 500.Y), with periodic side boundaries, a 1 mm pre-wetted inlet film profile defined via user-defined functions, and an outlet at 1 bar. A one-field formulation solved the incompressible continuity and momentum equations with a



a) b) c)

Figure 2.11 Rivulet flow on structured packing [12]: (a) 53.8 mL/min, (b) close up of a, (c) CFD at 41.8 mL/min.

continuum surface force model for surface tension, while phase distribution was tracked by VOF and interfacial microstructure effects captured through effective static contact angles on smooth surfaces and local contact angles at perforations. A passive tracer scalar equation was added to determine residence time distributions by convective transport, enabling direct comparison with high-resolution CT and tomographic tracer measurements for validation. [32]

Shojaee et al. conducted a CFD study on multiphase flow in structured packings using the VOF method to evaluate the effective interfacial area and liquid film behavior. Their CFD simulations revealed that both gas and liquid flow rates significantly influence the effective area, with higher velocities enhancing interfacial contact. The CFD results were validated against experimental data and empirical models [2, 27, 29], showing good agreement. The study demonstrated the capability of CFD to predict pressure drop and liquid film thickness, highlighting its utility for understanding mass transfer phenomena in complex packing geometries. [13]

Building on the computational framework of Singh et al., who simulated countercurrent gas–liquid flow in a Sulzer Mellapak 250.Y Representative Elementary Unit with the VOF method in STAR-CCM+ [10, 33], using periodic lateral boundaries, a pressure outlet at the base, and static or Kistler model dynamic contact angles to capture wetting, panels in the Figure 2.12a-d summarize the transient wetting and interfacial area dynamics obtained for a three REU stack. Their simulations covered liquid loads from 31 to $62\,\mathrm{m^3\,m^{-2}\,h^{-1}}$ at a fixed gas velocity of $1.0\,\mathrm{m\,s^{-1}}$, considered both a low viscosity solvent $(0.10\,\mathrm{M\ NaOH})$ and a more viscous $40\,\mathrm{wt\%}$ MEA solution, and achieved grid convergence at about

3.2×10^6 cells; effective mass transfer areas computed via the Danckwerts method agreed closely with experiments across the liquid load range.

In Figure 2.12, an initially wetted configuration at $L = 62\,\mathrm{m^3\,m^{-2}\,h^{-1}}$ evolves from a near continuous film to rivulets and drops that drain toward a quasi steady coverage by $t \approx 1$–$2\,\mathrm{s}$ shown in Figure 2.12-a, whereas, in Figure 2.12-b shows a snapshot at $t = 2.0\,\mathrm{s}$ for an initially dry start at the same L) and dynamic contact angle settings, highlighting the slower formation of connected pathways. Figure 2.12-c compares the temporal evolution of the normalized interfacial area $a_{int}(t)$ for wetted versus dry starts, with the inset repeating the comparison at $(\theta_A, \theta_R, \theta_E) = (85°, 60°, 70°)$. Figure-2.12-d presents $\Delta a_{int}(t)$ at two liquid loads, indicating a slightly larger change at the lower liquid load $(31\,\mathrm{m^3\,m^{-2}\,h^{-1}})$ for the same dynamic contact angle settings [10].

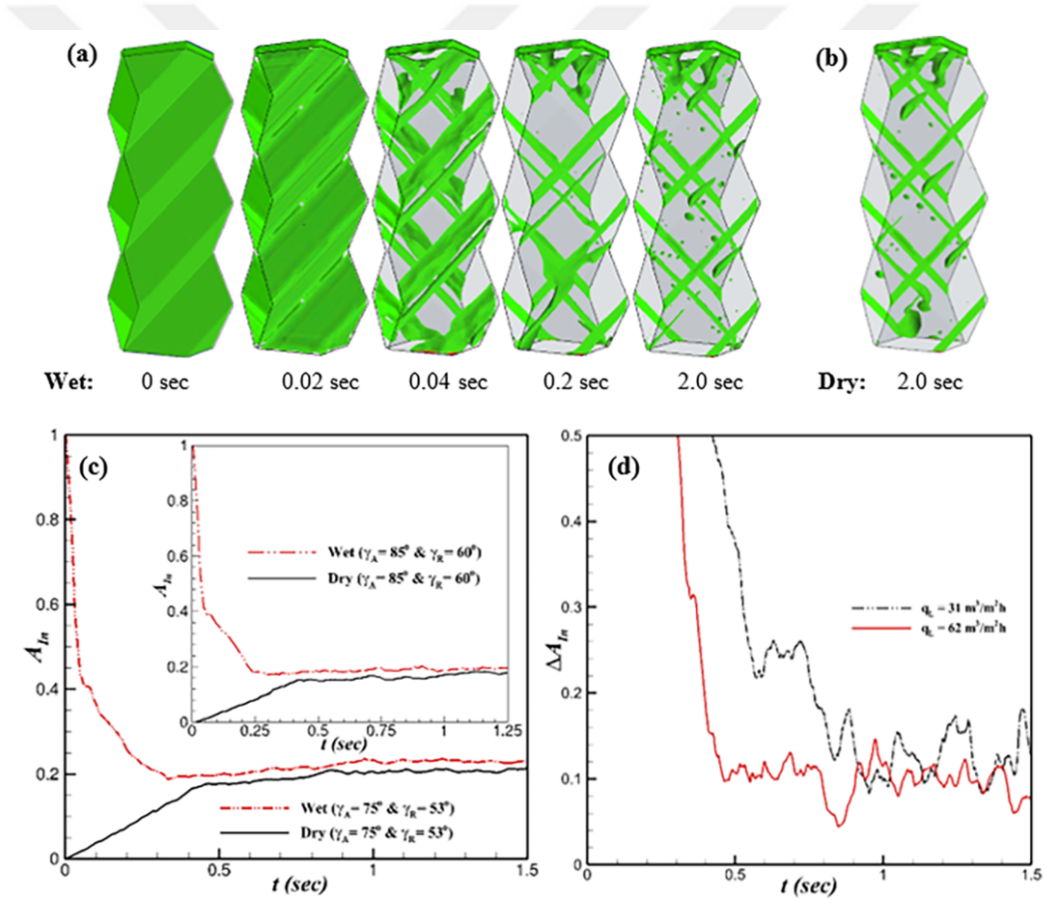


Figure 2.12 Transient wetting of a three REU stack at $L = 62\,\mathrm{m^3\,m^{-2}\,h^{-1}}$: (a) initially wetted evolution; (b) initially dry snapshot at $t = 2.0\,\mathrm{s}$; (c) comparison of $a_{int}(t)$ for wetted and dry starts; (d) $\Delta a_{int}(t)$ showing a slightly larger change at lower liquid load for the same dynamic contact angle settings.

In the study [34] Flexipac 1Y structured packing, implemented four turbulence closures-standard k–ϵ, RNG k–ϵ, k–ω, and the baseline (BSL) k–ω model with

up to 7 million cells for hydrodynamics and 1 million for scalar transport. The comparison of the dry pressure drop results were given in the Figure 2.13. Furthermore, they compared simulated dry and irrigated pressure drops, mass-transfer efficiency (via HETP), and heat-transfer profiles against experimental data. While both k–ϵ variants systematically underpredicted pressure drops and overestimated transfer resistances, the k–ω and BSL formulations significantly improved accuracy, with the k–ω model yielding mean absolute relative errors of 16.9% (dry drop), 10.7% (irrigated), 8.1% (mass transfer), and 0.9% (heat transfer), and was ultimately recommended for its robustness and superior predictive capability.

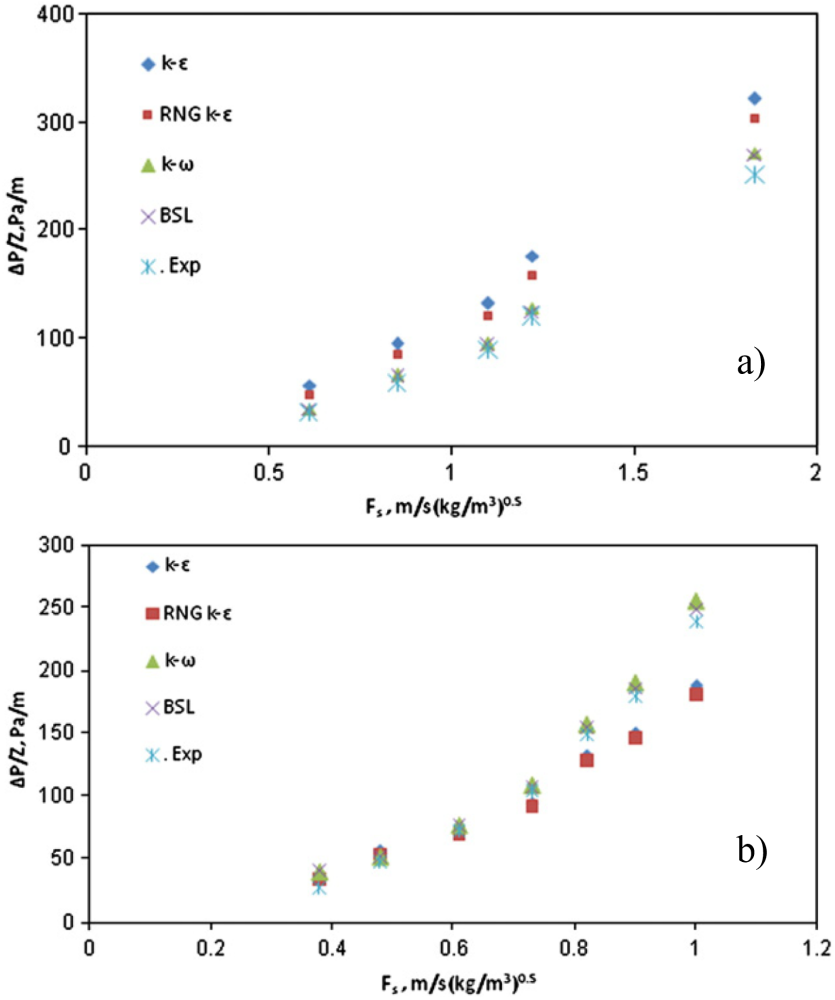


Figure 2.13 Irrigated pressure drop with respect to different F_G along with (a) $u_L = 0.0033$ m/s and (b) $u_L = 0.0203$ m/s (Adapted from [34])

2.2 Reactive Absorption

2.2.1 Experimental

In the 1996, Rocha et al. [35] introduced mass-transfer model based on a two-resistance approach which is based on their 1985 model a Sherwood-type gas-phase correlation as following:

$$Sh = C_1 \, Re_g^m \, Sc_g^n \tag{2.20}$$

$$\frac{k_g S}{D_g} = 0.054 \left(\frac{(U_{ge} + U_{Le}) \, \rho_g \, S}{\mu_g} \right)^{0.8} \left(\frac{\mu_g}{D_g \, \rho_g} \right)^{0.33} \tag{2.21}$$

Using the same effective velocities, a modified penetration model for the liquid phase, and an effective interfacial area from the Shi-Mersmann relationship, adjusted for surface enhancement and wettability, were employed [35]. The model was benchmarked against a broad data bank—covering Flexipac-2, Gempak 2A/2AT, Intalox 2T, Maxpak, Sulzer BX, and Mellapak 250Y/350Y/500Y—in distillation and absorption tests (cyclohexane/n-heptane at 0.02–4.14 bar; i-butane/n-butane up to 20.4 bar) in columns 0.07–12 m in diameter, yielding strong HETP predictions across most conditions [35].

The influence of operating and design variables on CO_2 absorption performance in columns equipped with four stainless-steel structured packings (Gempak 4A, Mellapak 500Y, Mellapak 500X, and Optiflow) was investigated [19]. Pilot-scale experiments were conducted in 0.1 m diameter columns packed to 0.98–2.21 m, where counter-current gas–liquid contact occurred between air/CO2 mixtures and either NaOH (1–2 kmol,m^{-3}) or MEA (3 kmol,m^{-3}) solutions. Gas-phase CO2 profiles were measured along each column via an IR analyser and converted into overall mass-transfer coefficients ($K_G a_e$). By systematically varying liquid load (3.8–29.3 m^3,m^{-2},h^{-1}), liquid CO_2 loading (0.25–0.50 mol,mol^{-1}), temperature (25–50 °C), packing-element rotation (0°, 45°, 90°), and distributor drip-point density, the individual effects of each parameter on column efficiency were identified. [19]

In their investigation of CO2 absorption using MEA solutions, Aroonwilas et al. [19] reported that $K_G a_e$ for Mellapak 500Y nearly doubled as the liquid load increased from 3.8 to 22.9 m^3,m^{-2},h^{-1}, while a less pronounced response was observed for Mellapak 500X and an even weaker one for Optiflow. These variations were attributed to geometric differences such as corrugation angle and open area.

Furthermore, higher CO2 loading in the solvent was found to severely hinder mass-transfer performance; increasing the loading from 0.25 to 0.50 mol,mol^{-1} decreased $K_G a_e$ by nearly 90%. Temperature was observed to have an asymptotic influence, where heating the MEA solution from 25 °C to 36 °C improved reaction kinetics and increased $K_G a_e$, while a further rise to 45 °C caused an efficiency reduction of about 10% owing to the lower equilibrium driving force.

Conventional 90° rotation of successive packing elements—even a relaxed 45° rotation—smoothed lateral liquid spreading and sustained high uptake, whereas aligning elements without rotation limited CO_2 absorption at the column top to only 27% of the benchmark case. Variations in distributor drip-point density produced only minor local differences, confirming the packings' intrinsic ability to redistribute liquid. Overall, the authors conclude that optimal CO_2 column design should prioritize adequate liquid irrigation, moderate solvent temperatures and at least 45° cross-rotation of structured elements; among the candidates, Mellapak 500Y offers the most favourable trade-off between throughput and mass-transfer enhancement. [19]

In the literature, several studies have systematically characterized and modeled the effective mass-transfer area (a_e) along with the individual liquid- and gas-film coefficients (k_L, k_G) for both structured and random packings employed in reactive absorption processes. It has been consistently reported that a_e rises predominantly with liquid velocity and only weakly with gas velocity, exhibiting a sub-proportional growth relative to the nominal specific surface area of the packing. Building on these findings, Tsai et al. proposed a dimensionless framework that successfully correlates a_e across various packing geometries by emphasizing the influence of liquid flow rate, density, and surface tension, while revealing limited sensitivity to the gas flow rate. Furthermore, the study highlighted persistent deficiencies in classical empirical a_e/k correlations and underlined the importance of mechanistic models grounded in simultaneous measurements of a_e, k_L, and k_G [36].

In their dissertation, high-temperature (80–190 °C) CO_2 solubility and amine volatility for MEA, PZ, and blends, and builds empirical/rigorous models for process design in Aspen Plus was measured. Reported heats of absorption are typically 66–73 kJ mol^{-1} for representative MEA/PZ/MDEA blends over the studied range, with limited temperature sensitivity. A new MEA model ("Model B") introduces the MEACOOH species, improving predictions of CO_2 solubility, MEA volatility, and speciation relative to prior formulations. The model remains predictive at rich loading and elevated temperature where additional species materially affect p_{CO_2} and ΔH_{rxn}. [37]

In their experimental study, Aboudheir et al. investigated CO_2 absorption into monoethanolamine (MEA) using a laminar jet absorber over the temperature range of 293–333 K, MEA concentrations between 3 and 9 M, and solvent loadings up to approximately 0.49 mol CO_2/mol MEA. The results indicated that only the termolecular reaction mechanism could consistently reproduce the measured kinetics at high CO_2 loadings. Based on this mechanism, temperature-dependent rate constants for both amine- and water-catalyzed reactions ($k_{\mathrm{RNH_2}}$, $k_{\mathrm{H_2O}}$) were determined, leading to a reversible overall rate law applicable for absorber simulations. The proposed kinetic formulation successfully reconciles earlier discrepancies in the literature and enables reliable prediction of the apparent rate constant (k_{app}) across diverse datasets, providing a robust framework for modeling concentrated, highly loaded MEA systems [38].

A mechanistic framework was developed to integrate reaction kinetics, thermodynamics, liquid irrigation behavior, and packing geometry, enabling simultaneous prediction of gas- and liquid-side mass-transfer coefficients (k_G, k_L), effective interfacial area (a_e), and local species and temperature distributions within structured packings. The model accurately reproduced pilot-scale absorption data for reactive systems such as NaOH and MEA under varying gas and liquid loads, CO_2 concentrations, temperatures, and inlet distribution patterns, using packings representative of Gempak 4A and Mellapak 500Y/500X. The results demonstrated that interfacial area formation and overall mass-transfer performance are governed primarily by the quality of liquid distribution and the geometric configuration of the packing, providing spatially resolved insight for the design and scale-up of reactive CO_2 absorbers [39].

In wetted-wall measurements at $5\,\mathrm{mol\,L^{-1}}$ MEA, K_G values at $333\,\mathrm{K}$ were observed to exceed those at $313\,\mathrm{K}$ across the loading range, and a systematic decline of K_G with increasing CO_2 loading was recorded. As shown in Fig. 2.14, comparatively high K_G was sustained for $\alpha \leq 0.30$, followed by a pronounced drop beyond $\alpha \approx 0.45$; independent data reported by Dugas and Rochelle at identical conditions were found to coincide within experimental scatter. These observations highlight the sensitivity of overall mass-transfer performance to loading and temperature in MEA systems and can be used to inform absorber sizing and operating temperature selection. [40]

An improved spray-tower configuration (diameter-varying, opposed dual-nozzle impingement) is proposed to intensify CO_2 absorption with MEA. The measured overall mass-transfer performance ($K_G a_e$) increases with liquid flow rate, MEA concentration, and total gas flow, and decreases with inlet CO_2 fraction; a maximum

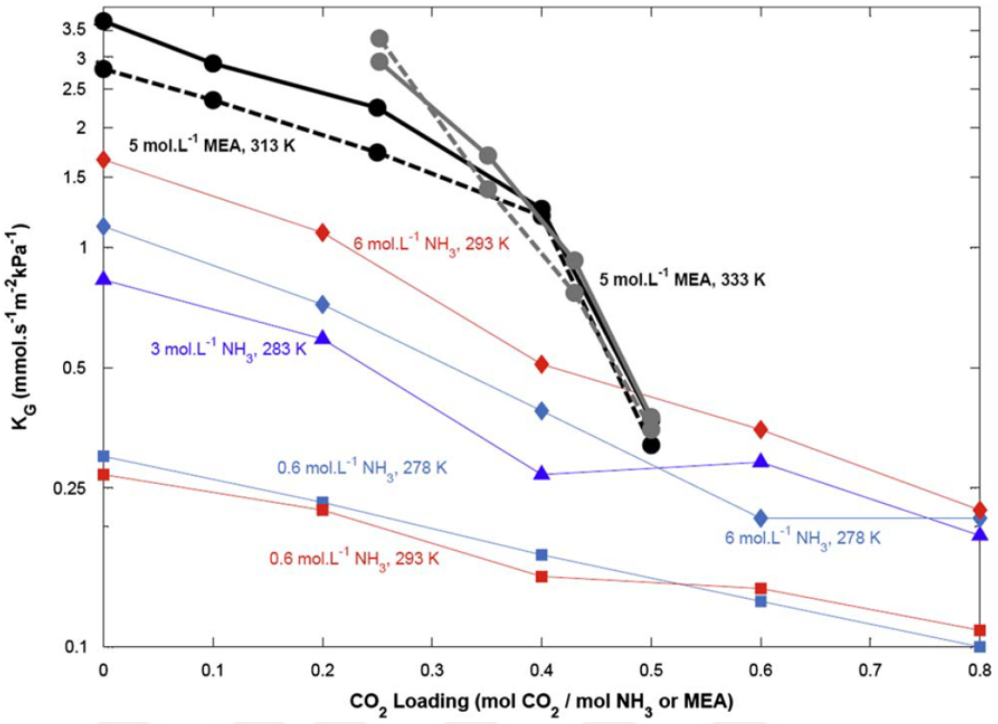


Figure 2.14 K_G versus CO_2 loading for 5 mol L^{-1} MEA at 313 and 333 K [40]

of 0.4773 kmol m^{-3} h^{-1} kPa^{-1} is reported under tested conditions. The study frames $K_G a_e$ as a practical, lumped performance metric combining thermodynamics, kinetics, and hydrodynamics for reactive absorption study. [20]

A fully-instrumented MEA post-combustion capture pilot with 0.125 m i.d. columns packed with Sulzer Mellapak 250Y (4.2 m absorber, 2.52 m stripper) processed 30–110 kg/h flue gas to study parameter impacts on capture and regeneration energy. The work establishes a detailed experimental baseline for MEA and a framework for scale-up and solvent benchmarking. [41] A 0.10 m i.d. glass absorber with adjustable packed height (1.6–8.2 m, Mellapak 250Y) treating ∼10% CO_2 synthetic gas validated a rate-based model; 80% recovery was achieved at 3.3 m packing and 2.1 L/min solvent. Results map how height, liquid flow, and lean loading shape capture efficiency and temperature bulges. [42] A mobile PDU at Laziska (up to 200 m^3/h) compared 30% MEA with 30/40% AEEA across standard, multi-absorber-feed, and split-flow configurations. The best case achieved a reboiler duty of 3.45 MJ kg^{-1} (CO_2) using 40 wt% AEEA in a split-flow configuration, while maintaining ≈90% CO_2 recovery [43].

2.2.2 Numerical

A VOF-based three-dimensional two-phase CFD framework, coupled with the RNG k–ε turbulence model and a two-component double-equation turbulence mass

transfer model (2CC), was employed to simulate the flow and mass transfer behavior within a representative unit of structured packing. Liquid holdup, wetted surface area, and HETP were determined from the calculated velocity distribution, phase fraction, and concentration fields. The model was validated against experimental data for Mellapak 350Y packing in a 150,mm diameter column under pressures ranging from 0.6 to 1.8,MPa, yielding a mean absolute deviation of 25.4%. It was observed that the CFD-based predictions provided a more accurate estimation of mass transfer efficiency than the conventional Gualito model. These results confirm the capability of CFD methodologies as effective tools for analyzing the performance of packed columns. [44]

A validated CFD framework was employed in which a passive–scalar model with a constant turbulent Schmidt number ($Sc_T = 0.7$) was calibrated against semi-empirical correlations obtained from wetted-wall pipe and pilot-scale SO_2–NaOH scrubbing experiments, achieving mass-transfer predictions within 5% of experimental values. Hydrodynamic simulations were conducted in Simcenter STAR-CCM+ utilizing the lag elliptic-blending $k - \epsilon$ RANS turbulence model with an all-y+ wall treatment. Comprehensive mesh-sensitivity analyses confirmed convergence for both pressure drop and mass-transfer coefficients. Systematic variation of specific packing area, channel inclination, and opening angle revealed that an opening angle near 90° maximizes mass transfer while increasing pressure losses, whereas enlarging the specific packing area reduces the height of a transfer unit (HTU) and enhances mass-transfer performance at the expense of higher pressure drop. [45]

A three-dimensional Eulerian porous-media CFD model of an MEA absorber packed with nine Mellapak 500X elements was implemented in ANSYS Fluent. Porous resistance, gas–liquid momentum exchange, liquid dispersion, interphase mass transfer, and a single-step reaction were included via calibrated coefficients, enabling reproduction of wet pressure drop, liquid holdup, and the CO_2 profile; the predicted gas-phase $y_{CO_2}(Z)$ closely follows measurements as illustrated in Fig. 2.15. The approach employed isotropic resistance and dispersion, constant-property kinetics, and an unresolved corrugated geometry without explicit turbulence resolution, which may limit hydrodynamic fidelity. [46]

A two-step, multi-scale modeling strategy was developed and validated to optimize the vapor–liquid mass-transfer layer in structured catalytic packings. At the micro-scale, a VOF model combined with a tracer method was utilized to quantify vapor and liquid Sherwood numbers as functions of operating conditions (vapor and liquid velocities) and four key geometrical

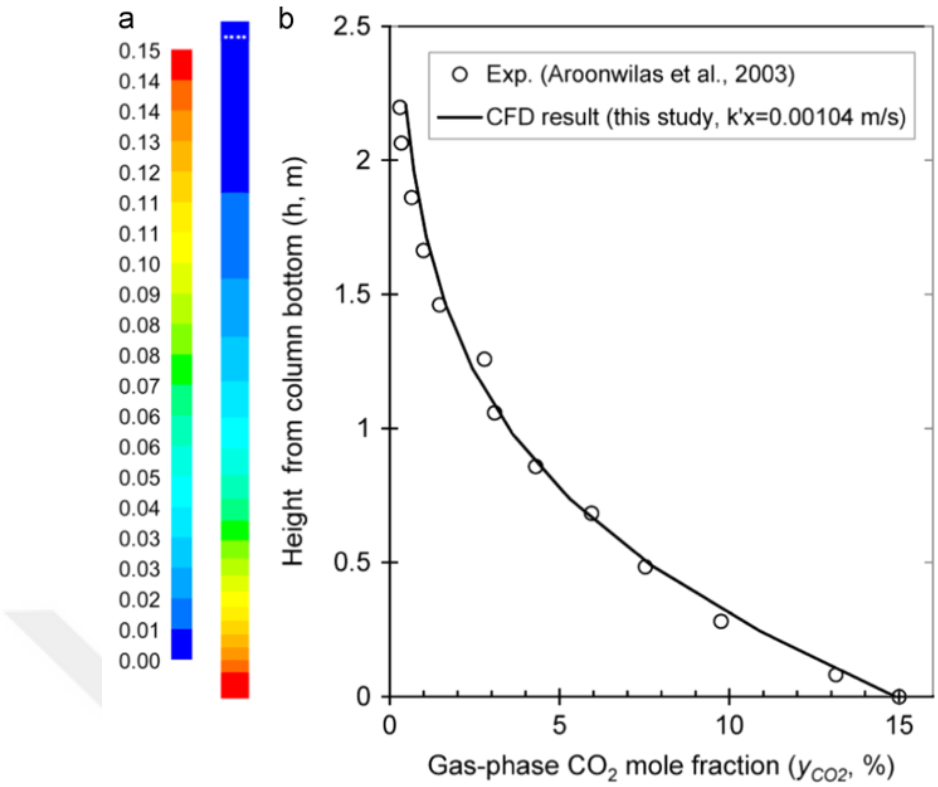


Figure 2.15 Gas-phase CO_2 mole fraction along column height: (a) CFD contours for the full column; (b) comparison of porous-media CFD predictions [46]

parameters of the mass-transfer layer—base length, wavy height, incline angle, and the mass-transfer-to-catalyst-layer area ratio. Universal correlations for mass-transfer coefficients were subsequently derived and integrated, together with a previously determined catalyst-layer efficiency factor, into a macro-scale non-equilibrium reactive-distillation model capable of accurately reproducing experimental conversions and temperature profiles. Analysis of the coupled model indicated that, among the four geometrical parameters, wavy height and area ratio exert the greatest influence on conversion, providing guidance for the optimal design of catalytic packings to enhance performance in industrial reactive-distillation applications. [14]

Their work [47] was applied for a VOF-based interfacial mass–transfer framework (Mass Fraction–Continuous Species Transfer (MF–CST) model) that tracks species mass fractions and enforces Henry-law concentration jumps via a solubility-flux term implemented with a density difference contribution. Validated in canonical 2D gas–liquid systems with single and dual film resistances, the model matches analytical solutions with $< 1\%$ absolute average deviation and is extended to a RANS-compatible turbulent formulation. A 3D demonstration on Mellapak-type structured packing shows numerically stable handling of $\sim 10^3$ concentration

discontinuities at the interface while predicting realistic hydrodynamic and NTU trends under typical F-factors and liquid loads. In Figure 2.16, liquid VOF and mass fraction of ammonia was given through the three stacked REU [47].

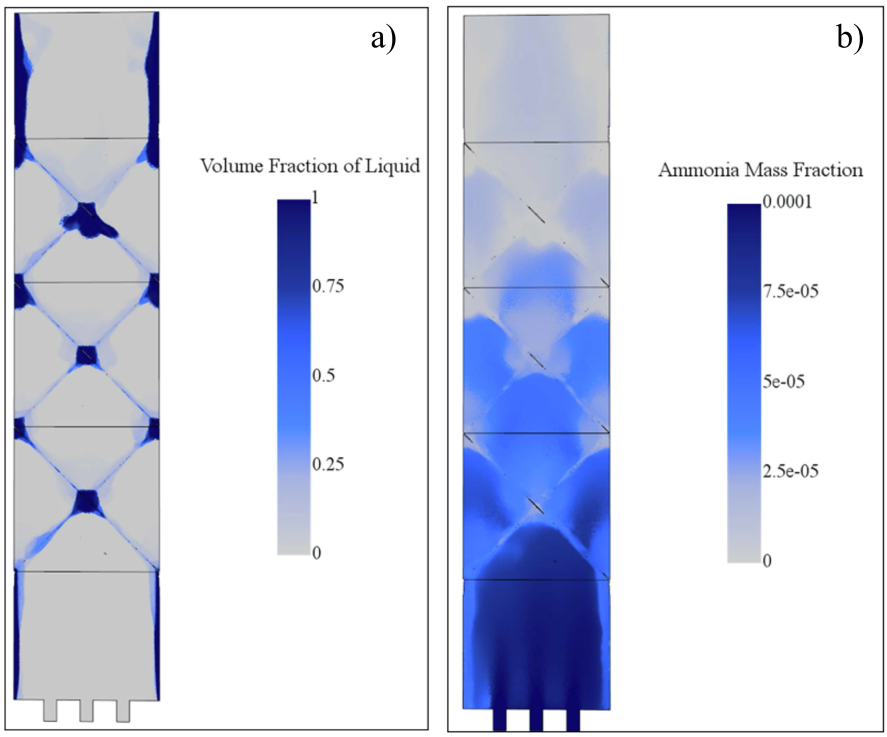


Figure 2.16 MF–CST with VOF Simulation over three stacked REU of Mellapak 250Y: (a) liquid volume fraction highlighting film and rivulet accumulation at corrugation junctions, (b) ammonia mass fraction alteration along the flow. (Adapted from [47]).

2.3 Other CFD Applications in Separation Process

State-of-the-art hydrodynamic CFD for structured packings increasingly couples carefully validated experiments with high-fidelity interface-capturing to isolate geometry effects and actionable metrics for design. Wire-mesh sensor–validated VOF models on commercial and 3D-printed replicas quantify how plate thickness, corrugation angle, perforations, and transition regions steer liquid distribution and pressure drop [48]

Beyond generic “wetted area”, separating static from dynamic interfacial area improves effective-area prediction and exposes contact angle (dynamic area) versus viscosity (static area) as the dominant levers [49]. Cryogenic contrast studies Liquid-oxygen (LOX) vs. water reveal regime shifts (rivulet to film), weak load-dependence of LOX interfacial area, and film-thickness–driven design criteria—guidance directly transferable to heat/mass-transfer scaling [50].

Additively-manufactured concepts such as SpiroPak demonstrate channelling suppression with $\approx$10% deviation and 50–70% lower dry pressure drops than comparable surface-area packings, alongside early-stage selection correlations [51]. On the methodology side, an AM-enabled loop (CAD-print-CFD-test) plus periodic OpenFOAM setups that include the column wall cut compute cost while preserving scale-critical maldistribution physics; these workflows underpin miniaturized designs (e.g., XW-Pak) that out-perform their parents at matched void fraction and area [52–54].

Pushing beyond hydrodynamic studies; fully coupled, first-principles multiphase frameworks now resolve the gas–liquid interface while co-solving interfacial mass transfer, reaction kinetics, heat release, and temperature/composition-dependent properties at packing-resolved scales-closing the gap between geometry optimization and absorber performance prediction on realistic structured packings [55]. Complementing geometry-resolved studies, a two-fluid Eulerian CFD model for a lab-scale MEA absorber (random packing) co-solves counter-current gas–liquid flow, reaction-heat effects, and rate-based mass transfer, matches experiments, and maps trends with lean loading, L/G, and inlet CO_2 fraction-providing compact, design-oriented guidance for reactive column performance [56]. Beyond CFD studies above, baffle-vortex demisters show an $\sim 40^\circ$ baffle angle maximizing efficiency and boosting $10\,\mu$m capture by ~ 2.7–$5.8\times$ versus wave-plates via DES-resolved vortical transport [57]; and JT-separator retrofits with reversed inlet deflectors raise droplet separation from $\approx$ 6–10% to $\approx$ 48–50%, underscoring inlet/baffle geometry as a dominant lever for two-phase separation [58].

3
THEORETICAL BACKGROUND

3.1 Hydrodynamics

3.1.1 Gas Load

Reporting gas load as F_G instead of u_G separates hydraulic loading from kinetic corrections such as Schmidt or Reynolds numbers that follow later. By implementing density inside a single variable, F_G uses data taken at different pressures and molecular weights easing scale-up and CFD/experiment comparison. For this reason F-Factor incorporated for Gas flow calculations. It is defined as:

$$F_G = u_G \sqrt{\rho_G} \tag{3.1}$$

where u_G is the superficial gas velocity and ρ_G is the bulk-average gas density [45].

3.1.2 Liquid Load

The superficial liquid load, L, is defined as the volumetric liquid flow rate per unit column cross-sectional area,

$$L = \frac{\dot{V}_L}{A_c}, \tag{3.2}$$

with $\dot{V}_L$ the liquid volumetric flow rate and A_c the column cross-sectional area. L is typically expressed in $\mathrm{m^3\,m^{-2}\,h^{-1}}$ and is widely used to characterize operating conditions in packed columns because it directly influences liquid film thickness, holdup, wetting behavior, and pressure drop [16, 27].

For structured packings, most semi-empirical correlations for pressure drop, liquid holdup, and effective interfacial area are regressed in terms of L and the superficial gas load (discussed in the Section 3.1.1), together with packing-specific geometric parameters such as specific surface area and corrugation angle [10, 11, 16, 18, 23, 27, 29, 32, 33]. At fixed gas conditions, increasing L generally thickens the liquid film, increases dynamic holdup, and enhances the fraction of the surface that is

effectively wetted, therefore enlarging the available gas–liquid interfacial area. It should be noted that higher liquid holdup also increases the wet pressure drop, and potentially causing "Flooding" phenomena.

3.1.2.1 Hydraulic Capacity, Loading, and Flooding

In addition to film hydrodynamics and holdup, the hydraulic capacity of a packed column is governed by the interaction between gas and liquid loads. At moderate gas velocities the pressure drop typically increases smoothly with the gas F–factor, while the liquid flows as a relatively stable falling film on the packing surfaces. As the gas load is raised at a fixed liquid rate, gas–liquid interactions intensify, the liquid film becomes swollen, and a characteristic change of slope appears in the pressure-drop curve; this onset of strong interaction is commonly referred to as the loading point [59, 60].

Further increase in gas velocity eventually leads to partial entrainment of liquid in the upward gas stream and the formation of froth-like flow structures, accompanied by a sharp rise in pressure drop; this regime is described as flooding, and it defines the upper operating limit of countercurrent packed columns [59, 61]. For structured packings, hydraulic models and capacity correlations typically relate the loading and flooding F–factors to liquid load, physical properties, and packing geometry, and are calibrated against large experimental databases covering a wide range of packing types and operating conditions [62]. In the present work, the CFD-predicted wet pressure drop is interpreted in this classical framework to assess how the simulated hydrodynamics approach loading and flooding conditions.

As shown in Figure 3.1, flooding corresponds to the regime where increasing gas load causes liquid holdup to rise sharply after a relatively flat pre-loading region (see the original Suess–Spiegel [2] plot in Appendix A.17).

3.1.2.2 Dimensionless Groups for Film and Gas Flow

The hydrodynamics of gas–liquid flow in packed columns are governed by the balance of inertia, viscous, gravitational, and capillary forces, which are conveniently expressed in terms of dimensionless groups [8]. The generic Reynolds number is defined as

$$\mathrm{Re} = \frac{\rho\, u\, d}{\mu}, \tag{3.3}$$

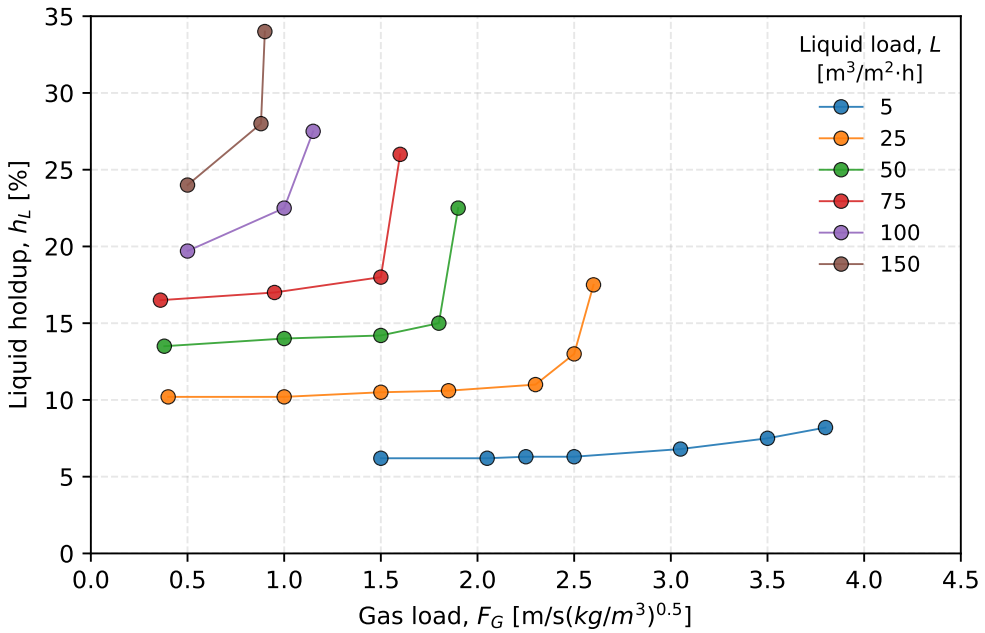


Figure 3.1 Liquid holdup h_L as a function of gas load F_G for various liquid loads L for Mellapak 500Y structural packing. Reproduced from [2].

with ρ the fluid density, u a characteristic velocity, d a characteristic length scale, and μ the dynamic viscosity. In the present work, it is useful to distinguish explicitly between liquid- and gas-based Reynolds numbers,

$$\mathrm{Re}_L = \frac{\rho_L u_L d_\mathrm{h}}{\mu_L}, \qquad \mathrm{Re}_G = \frac{\rho_G u_G d_\mathrm{h}}{\mu_G}, \tag{3.4}$$

where the subscript L refers to the falling liquid film on the packing and G to the gas core flowing through the channels. Correlations for film thickness, liquid holdup, and effective interfacial area typically employ Re_L as the relevant hydrodynamic parameter, whereas hydraulic capacity and flooding correlations often use Re_G or an equivalent gas F–factor that can be written in terms of ρ_G and u_G [62].

For the liquid film, additional dimensionless groups are defined using a characteristic liquid velocity u_L, density ρ_L, dynamic viscosity μ_L, surface tension σ, gravitational acceleration g, and a characteristic length d_h (for example, a hydraulic diameter or mean film thickness) [63],

$$\mathrm{We}_L = \frac{\rho_L u_L^2 d_\mathrm{h}}{\sigma}, \qquad \mathrm{Fr}_L = \frac{u_L^2}{g d_\mathrm{h}}, \qquad \mathrm{Ca} = \frac{\mu\,|\boldsymbol{u}|}{\sigma}. \tag{3.5}$$

The liquid Weber number, We_L, compares inertial and capillary forces and is relevant for rivulet formation, droplet detachment, and liquid redistribution at corrugation intersections [64]. The Froude number, Fr_L, characterises the relative

importance of inertia and gravity along the inclined packing channels, while the Capillary number, Ca, compares viscous and capillary forces and is often used in conjunction with dynamic contact-angle models to describe contact-line motion on wetted surfaces [33]. In structured-packings correlations, combinations of Re_L, We_L, Fr_L, and Ca_L are frequently employed to represent the dependence of holdup and effective interfacial area on operating conditions and fluid properties [64].

3.1.3 Static and Dynamic Liquid Holdup

The liquid holdup in a packed column quantifies the volume of liquid retained within the packing per unit column volume. A distinction is commonly made between static and dynamic holdup [27]. The static holdup corresponds to the liquid that remains on the packing surfaces after the flow has been stopped and the column has been allowed to drain under gravity; it reflects capillary retention and surface roughness effects. In contrast, the dynamic holdup denotes the total liquid present in the packing under operating conditions, including both the static fraction and the flowing film.

Static holdup is primarily governed by surface tension, wettability, and surface roughness, whereas dynamic holdup also depends strongly on the superficial liquid and gas loads [16]. Higher L typically increases dynamic holdup by thickening the film, while higher gas loads can partially strip liquid from the surfaces, reducing holdup in some regimes [64]. Holdup is directly related to the residence time distribution of the liquid phase and thus affects both the utilization of the packing volume and the effective interfacial area available for mass transfer in reactive absorption processes [19, 39].

3.1.4 Role of Surface Tension and Wettability

Surface tension, together with the static and dynamic contact angle, sets the capillary force scale that controls wetting, film stability, and the transition between continuous films and rivulets on corrugated sheets. Consequently, σ influences We and Ca. Further, surface tension is also affects the static liquid retention after drainage and the degree of effective wetting under operation. This effect is particularly relevant for high specific area structured packings, where reduced surface tension increases the accessible effective area by promoting spreading across the packing sheet corrugations [64–66].

3.1.5 Static Contact Angle

The static (equilibrium) contact angle, θ_{wall} (measured through the liquid), quantifies the force balance at the three–phase contact line. On an ideal, smooth, chemically uniform surface at equilibrium it obeys Young's relation,

$$\gamma_{SG} - \gamma_{SL} = \gamma_{LG} \cos\theta_{wall} \tag{3.6}$$

with γ_{ij} the solid–gas, solid–liquid, and liquid–gas interfacial tensions.

As shown in Figure 3.2, the equilibrium (static) contact angle θ_{wall} results from a balance of the solid–liquid, solid–gas, and liquid–gas interfacial tensions at the three-phase contact line. It should be noted that for a non-uniform surfaces the optically observed (apparent) angle θ^* generally differs from θ_{wall}.

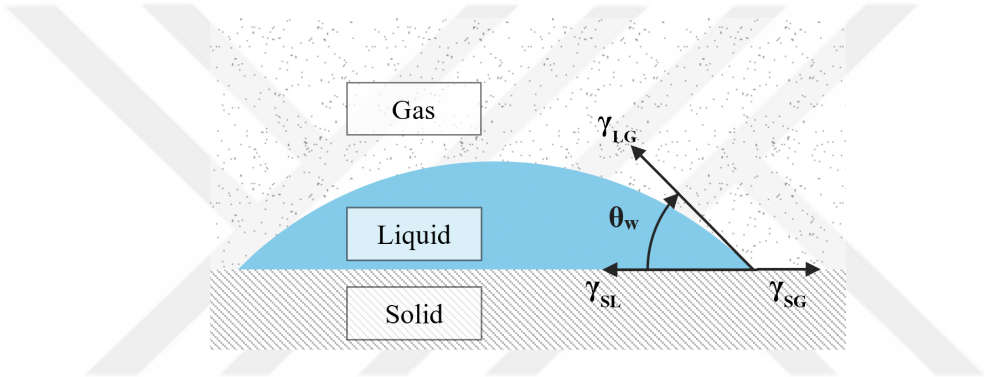


Figure 3.2 Definition of the static contact angle θ_{wall} on a horizontal solid surface.

3.1.6 Dynamic Contact Angle

In VOF, the wall–adhesion boundary uses the contact angle at solid walls to set the interface normal; thus prescribing a dynamic angle improves moving contact line behavior [67, 68]. Linear law driven by the local Capillary number,

$$\mathrm{Ca} = \frac{\mu\,|\boldsymbol{u}|}{\sigma} \tag{3.7}$$

As shown in Figure 3.3, real surfaces typically exhibit contact angle hysteresis between advancing and receding limits, θ_A and θ_R, especially on inclined or rough substrates. This hysteresis plays a key role in determining the onset of liquid motion, film breakup, and rivulet formation on structured packings.

Therefore, θ_S is the nominal (static) angle and Δ an amplitude defining advancing/receding bounds:

$$\theta_A = \theta_S + \Delta, \qquad \theta_R = \theta_S - \Delta. \tag{3.8}$$

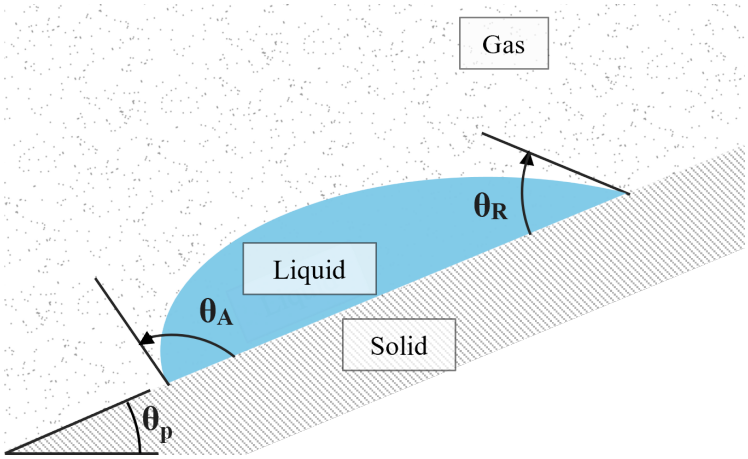


Figure 3.3 Definition of the dynamic contact angle θ_A and θ_R on an inclined solid surface.

The dynamic angle is then specified as

$$\theta_{\mathrm{A}}(\mathrm{Ca}) = \theta_S + \Delta \, \frac{\min(\mathrm{Ca},\, \mathrm{Ca}_{\max})}{\mathrm{Ca}_{\max}}, \tag{3.9}$$

$$\theta_{\mathrm{R}}(\mathrm{Ca}) = \theta_S - \Delta \, \frac{\min(\mathrm{Ca},\, \mathrm{Ca}_{\max})}{\mathrm{Ca}_{\max}}. \tag{3.10}$$

and clamped to the admissible interval

$$\theta_{dyn} \in [\,\theta_R,\ \theta_A\,]. \tag{3.11}$$

Equation (3.9) and (3.10) yields θ_{dyn}=θ_A at Ca=0 and saturates to θ_{dyn}=θ_R for $\mathrm{Ca} \geq \mathrm{Ca}_{\max}$, providing a numerically robust variation with velocity. Lastly, in implementation to ANSYS Fluent, θ_{dyn} is supplied in radians:

$$\theta_{dyn(rad)} \ = \ \theta_{dyn}[^\circ] \times \pi/180. \tag{3.12}$$

For lower θ the interfacial area and liquid holdup increase, improving $K_G a_e$ in absorbers; conversely, larger θ favors rivulet formation and localized breakup. In corrugated channels the lateral motion of the contact line is constrained by geometry, so the effect of θ_{DCA} on interfacial area may be weaker than on an open inclined plate. When calibrating θ_A, θ_R for simulations, values should be anchored to sessile-drop measurements on the actual packing surface (or close surrogates) and adjusted within reported hysteresis ranges to match observed regimes (film/rivulet/droplet) and interfacial areas.

3.2 Interface Capturing and Capillarity Modeling

Gas–liquid interfaces are captured using a Volume-of-Fluid (VOF) formulation, in which the primary phase indicator is the liquid volume fraction $\alpha_l \in [0,1]$ [69]. Cells with $\alpha_l = 0$ and $\alpha_l = 1$ correspond to pure gas and liquid, respectively, while interfacial cells satisfy $0 < \alpha_l < 1$. For incompressible, immiscible phases without phase change, α_l is advected by

$$\frac{\partial \alpha_l}{\partial t} \; + \; \nabla\cdot(\alpha_l \, \mathbf{u}) = 0, \tag{3.13}$$

where $\mathbf{u}$ is the shared velocity field. Mixture properties such as density and viscosity are then obtained by volume-fraction weighting of the pure-phase properties, ensuring sharp but conservative jumps across the interface.

Capillarity is modeled by the Continuum-Surface-Force (CSF) approach [68], which represents surface tension as a body force distributed over the finite-thickness numerical interface. The capillary force per unit volume acting on the gas–liquid interface is written as

$$\mathbf{F}_{\mathrm{S}} = -\,\gamma\,\kappa\,\nabla\alpha_l, \tag{3.14}$$

where γ is the surface-tension coefficient, κ is the local interface curvature, and $\nabla\alpha_l$ provides a smoothed approximation of the interface normal direction. This formulation concentrates the forcing in cells with $0 < \alpha_l < 1$, thereby recovering the correct pressure jump across the interface in the sharp-interface limit.

The curvature κ is evaluated from the divergence of the unit normal,

$$\kappa = \nabla\cdot\hat{\mathbf{n}}, \qquad\qquad \hat{\mathbf{n}} = \frac{\nabla\alpha_l}{|\nabla\alpha_l|}, \tag{3.15}$$

which links the geometrical description of the interface directly to the VOF field. Using α_l in both the normal and the CSF term ensures a consistent coupling between interface advection and capillary forcing.

Wettability at solid boundaries is imposed through a contact-angle condition that rotates the interface normal at the wall to enforce the prescribed static contact angle θ_w (measured through the liquid). Denoting by $\hat{\mathbf{n}}_w$ and $\hat{\mathbf{t}}_w$ the wall-normal and wall-tangent unit vectors, respectively, the modified interface normal at the wall is

$$\hat{\mathbf{n}} \;=\; \hat{\mathbf{n}}_w \cos\theta_w + \hat{\mathbf{t}}_w \sin\theta_w, \tag{3.16}$$

which aligns the reconstructed interface with the equilibrium contact angle used in Sections 3.1.5 and 3.1.6 and consistently couples wall wettability to the capillary force model.

3.3 Reactive Absorption

3.3.1 Overall Mass Transfer Coefficient

The classical expression obtained from integrating the overall driving force along the gas–phase height;

$$k_G a_e = \frac{u_G}{Z} \ln\left(\frac{c_{G,in} - c_G^*}{c_{G,out} - c_G^*}\right) \tag{3.17}$$

Under the fast–reaction assumption, $c_G^* \approx 0$ is applied since:

- the column height is relatively short (REU approach), and
- the chemical reaction is sufficiently fast to maintain negligible gas–phase CO_2 concentration.

Consequently, the overall gas-side coefficient through an inlet–outlet log-mean driving force expressed as following [21, 45]:

$$k_G a_e = \frac{u_G}{Z} \ln\left(\frac{c_{G,\text{in}}}{c_{G,\text{out}}}\right) \tag{3.18}$$

or,

$$K_G a_e = \frac{Q_G}{A_\text{i} Z} \ln\left(\frac{c_{G,\text{in}}}{c_{G,\text{out}}}\right) \tag{3.19}$$

Because the area term a_e already includes packing geometry, $k_G a_e$ cleanly compares very different structured packings without estimating individual a_e values. Furthermore, the experimentally accessible quantity that can be fed directly to height of transfer unit correlations.

3.3.2 Interfacial Area

Packed-column performance is often described in terms of the overall volumetric mass-transfer coefficient, $K_\text{G} a_\text{e}$, where a_e is the effective gas–liquid interfacial area per unit packed volume. The packing manufacturer typically reports a geometric (or specific area), a_p, based purely on the developed surface of the dry packing.

However, under realistic operating conditions only a fraction of this surface is wetted and actively participates in mass transfer (typically, $a_{\mathrm{e}} \leq a_{\mathrm{p}}$) [16, 27].

The ratio,

$$\text{Relative Interface Area } = \frac{a_{\mathrm{e}}}{a_{\mathrm{p}}} \tag{3.20}$$

is often referred to as the wetting efficiency or wetting fraction. It depends on liquid load, fluid properties (viscosity, surface tension, wettability), and packing geometry, and is commonly correlated as a function of Reynolds, Weber, and Froude numbers for a given packing family [16, 27, 28]. Experimentally, a_{e} is frequently inferred from absorption experiments using a well-characterised gas–liquid reaction and the two-film concept (e.g. Danckwerts' method), whereas in modern CFD and VOF-based simulations it can be estimated directly from the resolved gas–liquid interface area within a representative elementary unit of the packing [16, 33].

In the present work, an analogous numerical interfacial area, a_{int}, is extracted from the VOF liquid volume-fraction field, α_L. The reconstructed interface is identified using an isosurface of $\alpha_L \approx 0.5$ to $\alpha_L \approx 0.01$ as the nominal phase boundary. The total area of this VOF interface within the representative packing element is then normalized by the packed volume to obtain a_{int}. Although a_{int} is not strictly identical to the experimentally inferred a_{e}, it mimics the the actively wetted liquid on the packing surface.–liquid area on the structured packing—and is therefore used as a CFD-based surrogate for a_{e} when comparing simulation results with correlations [16, 33].

$$\text{Relative Interface Area (VOF Interface)} = \frac{a_{\mathrm{int}}}{a_{\mathrm{p}}} \tag{3.21}$$

3.3.3 CO_2–MEA Reaction Mechanism

The absorption of CO_2 into aqueous monoethanolamine (MEA) proceeds through a sequence of acid–base and zwitterion-formation reactions that can be represented by two kinetic pathways. In the primary route, CO_2 directly reacts with free MEA to form carbamate via a zwitterion intermediate, while the secondary route involves hydrated CO_2 (carbonic acid) reacting with MEA. The overall rate is strongly influenced by MEA concentration and local availability of CO_2 at the gas–liquid interface.

$$\text{(R1)} \quad \mathrm{CO_2} + 2\,\mathrm{MEA} \xrightarrow{k_1} \mathrm{MEACOO^-} + \mathrm{MEAH^+} \tag{3.22}$$

$$\text{(R2)} \quad \mathrm{CO_2} + \mathrm{H_2O} + \mathrm{MEA} \xrightarrow{k_2} \mathrm{MEACOO^-} + 2\,\mathrm{H^+} \tag{3.23}$$

Both reactions are modeled as volumetric processes following the Arrhenius rate expression:

$$k_i = A_i \exp\left(-\frac{E_{a,i}}{R\,T}\right), \qquad i = 1, 2, \tag{3.24}$$

where A_i and $E_{a,i}$ are the pre-exponential factor and activation energy, respectively.

3.3.3.1 Film and Penetration Theory

For gas absorption accompanied by a liquid phase reaction, the absorption flux of CO_2 is commonly written using the two film concept as

$$N_{\mathrm{CO_2}} = k_G\,(c_{G,b} - c_{G,i}) = E\,k_L\,(c_{L,i} - c_{L,b})\,, \tag{3.25}$$

where E is the enhancement factor, defined as the ratio of the absorption flux with reaction to the physical absorption flux (no reaction).

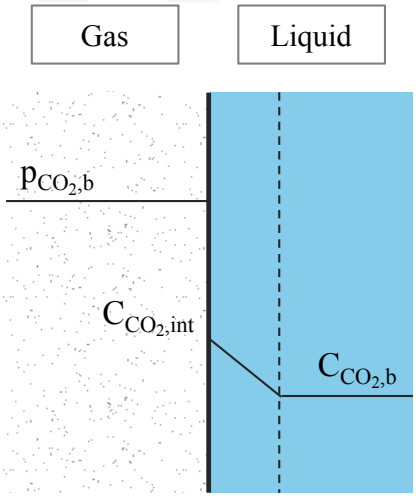


Figure 3.4 Concentration and partial pressure profiles in the two film concept.

Under conditions relevant to CO_2–MEA absorption, the liquid phase reaction can often be treated as pseudo first order in dissolved CO_2,

$$r_{\mathrm{CO_2}} = k_{\mathrm{app}}\,c_{\mathrm{CO_2},L} \qquad k_{\mathrm{app}} \approx k_2\,c_{\mathrm{MEA,free}} \tag{3.26}$$

This relationship leads directly to the Hatta number; therefore, the Hatta number is defined as follows:

$$Ha = \frac{\sqrt{k_{\text{app}}\, D_{\text{CO}_2,L}}}{k_{L,0}} \tag{3.27}$$

Here, $D_{\text{CO}_2,L}$ is the molecular diffusivity of dissolved CO_2 in the liquid phase, and $k_{L,0}$ denotes the baseline liquid side mass transfer coefficient in the absence of chemical reaction.

For an irreversible pseudo first order reaction and negligible bulk dissolved CO_2 (i.e. $c_{L,b} \approx 0$), the enhancement factor can be expressed as a function of Ha. Within the classical film theory, a common expression is

$$E \approx \frac{Ha}{\tanh(Ha)} \tag{3.28}$$

In surface renewal or penetration based formulations, an alternative approximation is often used,

$$E \approx \sqrt{1 + Ha^2} \tag{3.29}$$

In the present CO_2–MEA system, absorption is expected to lie in the fast reaction regime (large Ha). Therefore, both approximations, Eq. 3.28 and Eq. 3.29, reduce to the same asymptotic behavior ($E \sim Ha$) and yield nearly identical enhancement factors.

The regime classification is commonly summarized as [70]:

- Slow reaction: $Ha < 0.3$
  $E \approx 1$ (reaction provides negligible enhancement)
- Intermediate reaction: $0.3 \leq Ha \leq 3$
  E departs from unity and increases with Ha
- Fast reaction: $Ha > 3$
  $E \approx Ha$, and the absorption rate becomes weakly dependent on $k_{L,0}$

In the fast reaction regime, the bulk liquid CO_2 concentration remains small due to rapid consumption in the liquid, which is consistent with applying $c_G^* \approx 0$ in the log mean driving force formulation used to evaluate $K_G a_e$ from inlet and outlet gas phase CO_2 concentrations.

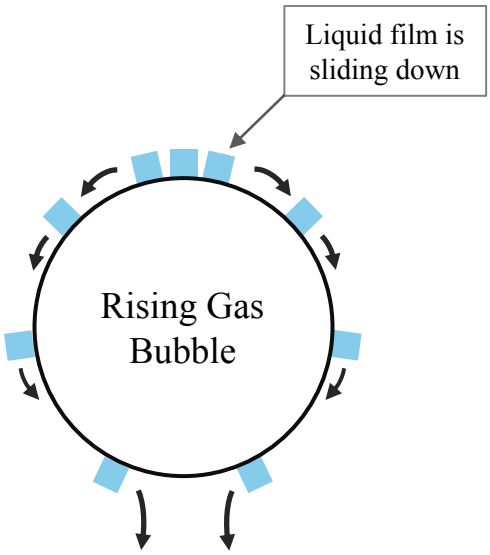


Figure 3.5 Schematic representation of penetration and surface renewal concepts.

In the present CFD–UDF implementation, the reaction enhancement is incorporated by defining the liquid side coefficient as

$$k_L = E\, k_{L,0} \tag{3.30}$$

Consistent with the penetration or surface renewal approximation adopted in the UDF, Eq. 3.29 is used, yielding

$$k_L = k_{L,0}\sqrt{1 + Ha^2} \tag{3.31}$$

In the present work, the penetration-based formulation is adopted to avoid imposing an external surface-renewal limitation at the VOF resolved interface. Instead, the penetration process is expressed in terms of renewal for the VOF solution, thereby providing a more physically grounded prediction of liquid-side mass transfer.

3.3.4 Interfacial Equilibrium and Henry's Law

At infinite dilution, the interfacial equilibrium between the gas and liquid phases for CO_2 is written using Henry's law in the (p/x) convention:

$$x_{eq} = \frac{p_{CO_2}}{H_{px}(T)}, \qquad p_{CO_2} = y_{CO_2}\, P_{\text{abs}}, \tag{3.32}$$

where $H_{px}(T)$ has units of pressure and P_{abs} is the absorber pressure [71].

The (p/x) Henry constant relates to the (c/p) convention through the liquid molar density. For dilute CO_2 in water, the solvent molar density is approximated as $C_L = \rho_L / M_{H_2O}$, hence:

$$H_{px}(T) \;=\; \frac{C_L}{H_{cp}(T)} \;=\; \frac{\rho / M_{H_2O}}{H_{cp}(T)}. \tag{3.33}$$

3.3.4.1 Temperature Dependence of Henry's Constant

The solubility of CO_2 in aqueous solutions is commonly described using the (c/p) Henry constant $H_{cp}(T)$, which follows an Arrhenius type dependence on temperature. Using the van't Hoff form [72, 73], the temperature dependence is:

$$H_{cp}(T) \;=\; H_{cp,ref}\, \exp\!\left[\beta \left(\frac{1}{T} - \frac{1}{T_{\mathrm{ref}}}\right)\right] \tag{3.34}$$

where $H_{cp,ref}$ is the reference value at T_{ref} (typically 298 K), and β is an empirical constant that represents the slope of $\ln H_{cp}$ versus $1/T$ (with reported values in the range 2200 to 2600 K for CO_2).

The liquid side driving force in mole fraction is defined as:

$$\Delta x \;=\; x_{eq} - x_L \qquad \text{(liquid side)}. \tag{3.35}$$

3.3.5 CO_2–MEA Kinetics and Apparent First Order Rate

The intrinsic kinetics of CO_2 absorption into MEA can be expressed as two parallel termolecular reactions representing the direct amine and the water catalyzed pathways. Each pathway follows an Arrhenius type dependence:

$$k_{\mathrm{RNH_2}}(T) = A_1 \exp\!\left(-\frac{E_1}{RT}\right) \times 10^{-6}, \tag{3.36}$$

$$k_{\mathrm{H_2O}}(T) = A_2 \exp\!\left(-\frac{E_2}{RT}\right) \times 10^{-6}, \tag{3.37}$$

where the factor 10^{-6} converts the concentration basis from mol to kmol in the rate constant.

The overall apparent first order rate constant is obtained by summing the contributions:

$$k_1 \;=\; k_{\mathrm{RNH_2}}\,[\mathrm{MEA}]^2 \;+\; k_{\mathrm{H_2O}}\,[\mathrm{H_2O}]\,[\mathrm{MEA}]. \tag{3.38}$$

With concentrations expressed in $\mathrm{kmol\,m^{-3}}$ and $k_{\mathrm{RNH_2}}, k_{\mathrm{H_2O}}$ in $\mathrm{m^6\,kmol^{-2}\,s^{-1}}$, k_1 has units of $\mathrm{s^{-1}}$. The CO_2 consumption rate in the liquid phase is:

$$r_{\mathrm{CO_2}} \;=\; k_1\, c_{\mathrm{CO_2,liq}}, \tag{3.39}$$

where $c_{\mathrm{CO_2,liq}}$ is the dissolved CO_2 concentration in the liquid phase.

The CO_2 mass fraction in the liquid phase (Y_{CO_2}) is converted to mole fraction (x_L):

$$x_L \;=\; \frac{Y_{CO_2}/M_{CO_2}}{Y_{CO_2}/M_{CO_2} + (1 - Y_{CO_2})/M_{H_2O}}. \tag{3.40}$$

The average molecular weight of the liquid mixture is computed from the mole fractions:

$$M_{\mathrm{mix}} \;=\; \left(\frac{x_L}{M_{CO_2}} + \frac{1 - x_L}{M_{H_2O}}\right)^{-1}. \tag{3.41}$$

The molar density of the liquid mixture is then:

$$c_L \;=\; \frac{\rho_L}{M_{\mathrm{mix}}}. \tag{3.42}$$

In the film theory framework, the volumetric molar absorption rate is modeled as:

$$N \;=\; k_{L0}\, a_{\mathrm{eff}}\, \Delta x\, c_L \qquad \left[\mathrm{mol\,m^{-3}\,s^{-1}}\right]. \tag{3.43}$$

Only cells containing a gas–liquid interface (VOF) and adjacent to the packing are counted for mass transfer. Accordingly, the effective specific area is expressed as:

$$a_{\mathrm{eff}} \;=\; a_0\, \Phi, \qquad a_0 \approx 500\ \mathrm{m^2\,m^{-3}}\ \text{(Mellapak 500Y)}, \qquad 0 \le \Phi \le 1. \tag{3.44}$$

The corresponding mass source term used in the UDF is:

$$\dot{m} \;=\; N\, M_{CO_2} \qquad \left[\mathrm{kg\,m^{-3}\,s^{-1}}\right], \tag{3.45}$$

where a positive $\dot{m}$ indicates transfer from gas to liquid.

4
COMPUTATIONAL METHODOLOGY

4.1 Geometrical Representation of the Packing

In the computational domain, the representative elementary units (REUs) were stacked periodically to reproduce the periodic structure of the Mellapak 500Y packing. As illustrated in Figure 4.1, three different computational configurations were constructed, namely single-, four-, and six-REU models, in order to examine the influence of the domain length on the hydrodynamic and mass transfer predictions.

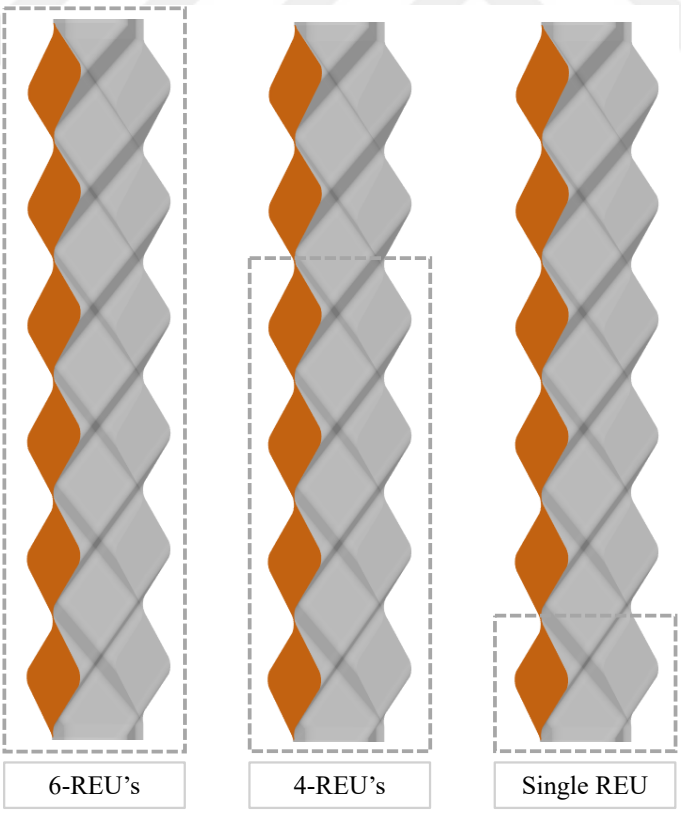


Figure 4.1 Representation of six-REU's, four-REU's and single-REU

The schematic (Fig. 4.2) illustrates a single corrugated packing element defined by a repeating unit cell with vertical height $B = 11.25\ mm$ and corrugation spacing $S = 8.0\ mm$ to represent Sulzer Mellapak 500.Y. Each corrugation ridge is formed by two inclined facets meeting at an apex angle $\theta = 45°$. The local bend at each apex has a radius $R = 1.0\ mm$, ensuring a smooth transition between facets [31]. As will be discussed in detail in the Section 5.1, the face-to-face spacing between adjacent corrugated sheets was finally set to $F = 0.24$ mm. The spacing was adjusted to calibrate the pressure-drop predictions in order to ensure the consistency between dry and wet pressure-drop measurements.

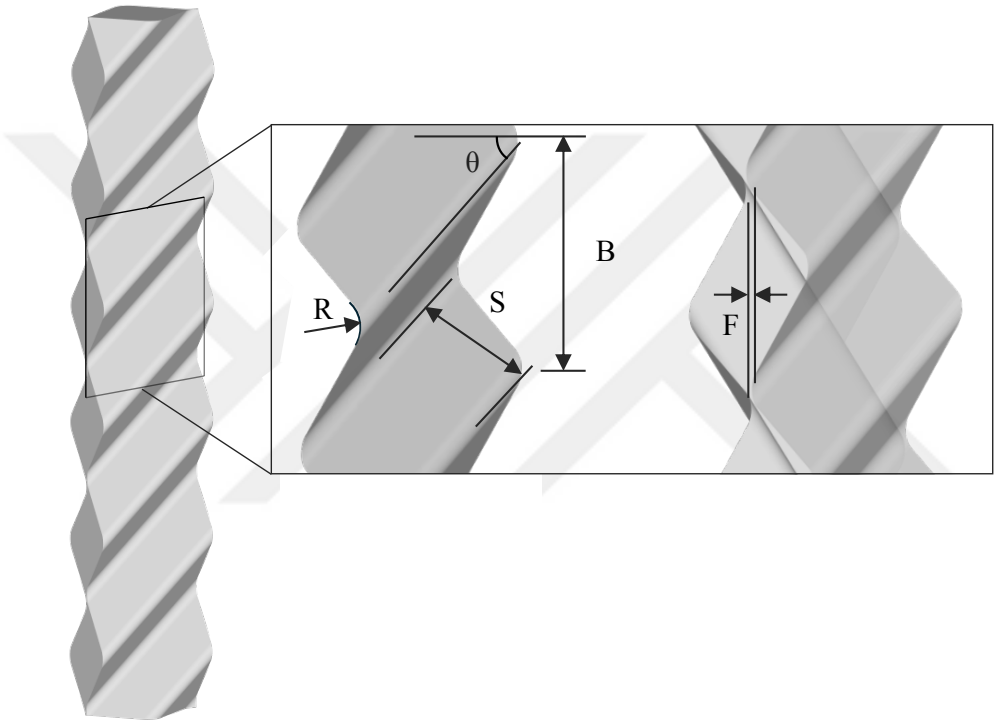


Figure 4.2 Dimensions defined to represent Sulzer Mellapak 500.Y

4.2 Mesh Generation

4.2.1 Pressure Drop Benchmarking and Calibration

The computational domains were 3D-modeled in SpaceClaim v24 R2, yielding three primary geometries containing six, four, and one REU's. A corrugation gap of 0.24 mm between neighboring sheets was adopted as the optimum spacing. This value is an order of magnitude smaller than the 0.24 mm clearance used by Singh [10, 33] and Ambekar [11], which would otherwise result in unrealistically low pressure-drop predictions. All meshes were produced with ANSYS Fluent 24 R2 Meshing. Two unstructured algorithms were benchmarked:

- Hex–core: a surface–triangular skin is first generated; a hexagonal core region is then extruded normal to the surface, finally transitioning to polyhedral cells in the outer zones. The approach limits cell count while retaining surface fidelity.
- Poly–hexcore: an additional polyhedral refinement band is introduced around geometry before core extrusion, improving gradient resolution in complex junctions and connections.

For the six-REU model, four main grid densities were examined to demonstrate mesh independence: 3.5M cells (≈ 0.53M cells/REU), 2.4M cells (≈ 0.37M cells/REU), and 0.70M cells (≈ 0.10M cells/REU).

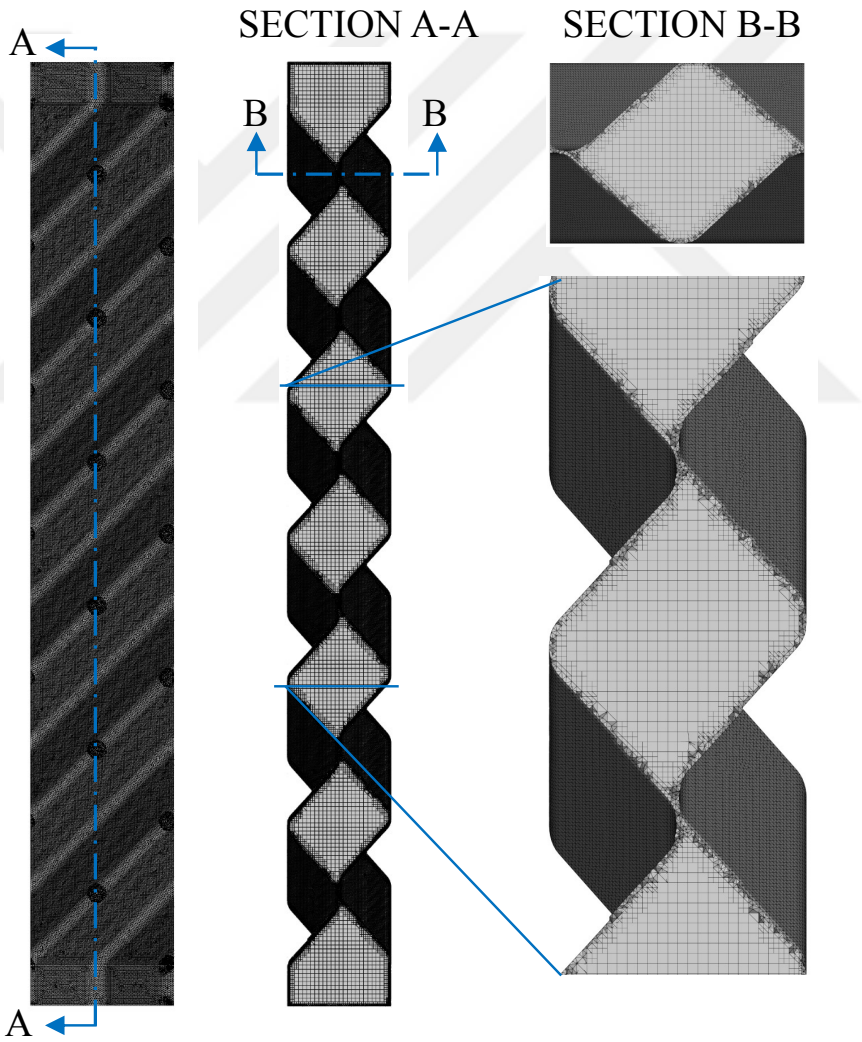


Figure 4.3 Dimensions defined to represent Sulzer Mellapak 500.Y

In addition to these meshes, to examine the influence of near-wall resolution, a further mesh refinement conducted.

The identical meshing strategy was applied to the four-REU geometry. It should be denoted that all meshes exhibit an orthogonal quality above 0.2 [74].

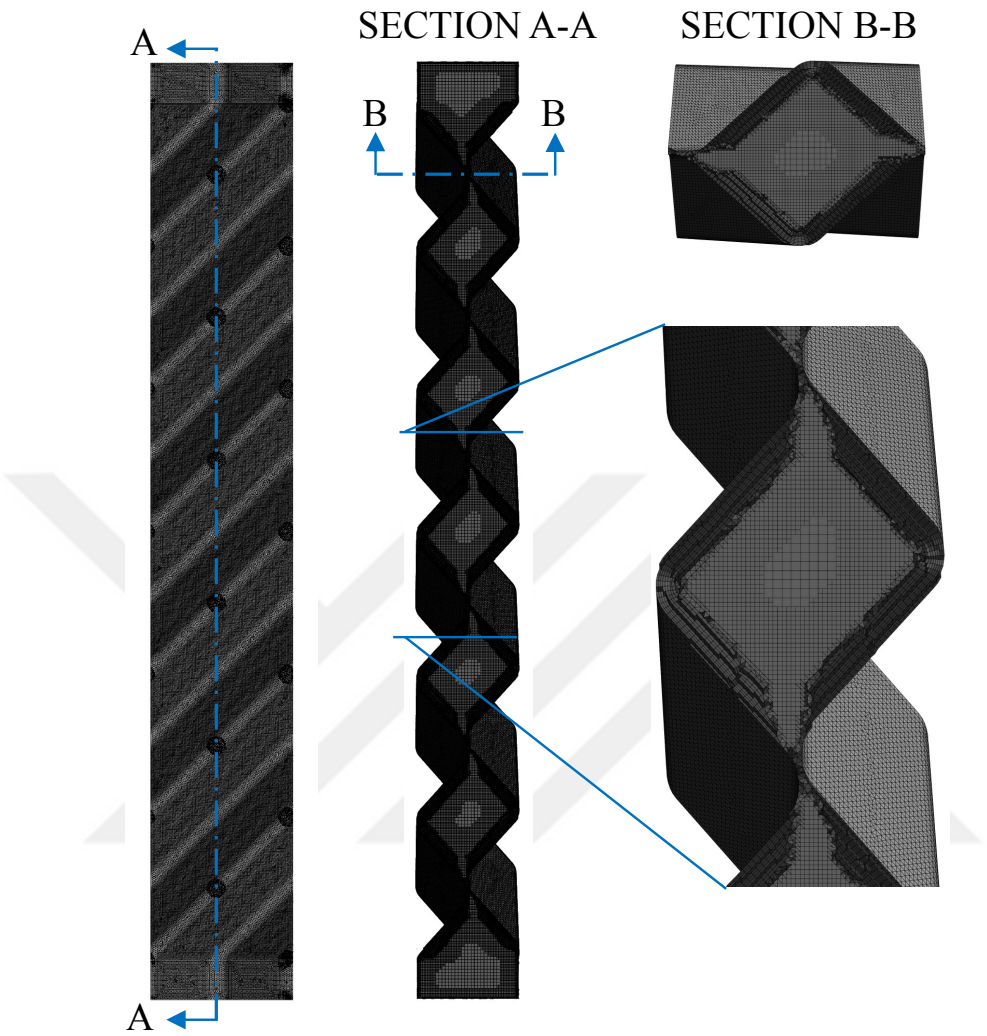


Figure 4.4 Dimensions defined to represent Sulzer Mellapak 500.Y

A summarizing table can be demonstrated as:

Table 4.1 Mesh configurations and cell counts for all single phase models

Mesh ID	Applied for: Single,4, 6-REU's	Cells per REU
M–A	Fine	≈0.53 M cells/REU
M–B	Fine: 8 and 12 prism layers	≈0.53 M cells/REU
M–C	Medium	≈0.37 M cells/REU
M–D	Coarse	≈0.10 M cells/REU

4.2.2 Two-Phase Hydrodynamic Analyses

Single REU configuration was used to simulate VOF studies. A variant created from the pressure drop geometry which includes a dedicated liquid inlet partition to conduct VOF studies. All grids were generated with the Hex–core procedure described above. Four different mesh resolutions were constructed:

Table 4.2 Mesh configurations and cell counts for all hydrodynamics two-phase models

Mesh ID	Description	
M4	Finest with 12 prism layers	≈1.02 M cells/REU
M3	Fine with 8 prism layers	≈0.71 M cells/REU
M2	Medium, no prism layers	≈0.44 M cells/REU
M1	Coarse, no prism layers	≈0.26 M cells/REU

4.2.3 Two-Phase Reactive Absorption Analyses

Single REU configuration was used to simulate Reactive Absorption studies. All grids were generated with the Hex–core procedure described above. Five different mesh resolutions were constructed:

Table 4.3 Mesh configurations and cell counts for all hydrodynamics two-phase models

Mesh ID	Description	
M5	Finest with 12 prism layers	≈2.22 M cells/REU
M4	Fine with 9 prism layers	≈1.12 M cells/REU
M3	Base with 9 prism layers	≈0.76 M cells/REU
M2	Medium, 7 prism layers, AR: 2	≈0.51 M cells/REU
M1	Coarse, 7 prism layers, AR: 2	≈0.19 M cells/REU

4.3 Governing Equations and Physical Models

Equation (4.1) allows mass conservation for each phase q in the VOF framework by balancing the temporal change and convective transport of the volumetric phase mass with the net interfacial mass exchange $(\dot{m}_{pq} - \dot{m}_{qp})$. The inclusion of density

allows the formulation to remain valid for lightly compressible fluids, while α_q keeps the description bounded between 0 and 1 for each computational cell.

$$\frac{\partial}{\partial t}(\rho\,\alpha_q) + \nabla\cdot(\rho\,\alpha_q\,\mathbf{u}_q) = \sum_{p=1}^{N}(\dot{m}_{pq} - \dot{m}_{qp}) \tag{4.1}$$

Equation (4.2) transports the phase indicator α_q with the bulk velocity $\mathbf{u}$, optionally augmented by a numerical or physical source S_{α_q} that promotes interface sharpening. Accurate resolution of this term is important for sharp liquid–gas interfaces in Eq. (4.3).

$$\frac{\partial \alpha_q}{\partial t} + \mathbf{u}\cdot\nabla\alpha_q = S_{\alpha_q} \tag{4.2}$$

The SIMPLE (Semi-Implicit Method for Pressure-Linked Equations) algorithm was employed to couple pressure and velocity. SIMPLE method ensured mass conservation (continuity) by iterating momentum–pressure corrections until convergence. Low-mach and incompressible nature of the study made it a natural choice. The one-fluid momentum equation (4.3) solves a single velocity field weighted by the local mixture density. On the right-hand side, the pressure gradient drives the flow, the effective viscosity $\mu_{\text{eff}} = \mu + \mu_t$ combines molecular and turbulent stresses, $\rho\mathbf{g}$ incorporates body forces, and $\mathbf{F}_\sigma$ introduces surface-tension forces computed from the interface curvature given by the VOF field. This coupling enables the model to capture complex interfacial hydrodynamics such as rivulet flow over structural packings.

$$\frac{\partial}{\partial t}(\rho\mathbf{u}) + \nabla\cdot(\rho\mathbf{u}\mathbf{u}) = -\nabla p + \nabla\cdot(\mu_{\text{eff}}\nabla\mathbf{u}) + \rho\mathbf{g} + \mathbf{F}_\sigma \tag{4.3}$$

Equation (4.4) tracks the mass fraction Y_i of each chemical species. Convective and diffusive fluxes are complemented by the net production term R_i, which embeds homogeneous or heterogeneous reactions. The diffusive flux $\mathbf{J}_i$ follows Fick's law corrected for turbulent mixing through the turbulent Schmidt number S_c, ensuring that scalar transport is consistent with the turbulence field.

$$\frac{\partial}{\partial t}(\rho Y_i) + \nabla\cdot(\rho\mathbf{u}Y_i) = -\nabla\cdot\mathbf{J}_i + R_i, \qquad \mathbf{J}_i = -\left(\rho D_{i,m} + \frac{\mu_t}{S_c}\right)\nabla Y_i \tag{4.4}$$

Since the local Reynolds number in the structured packing ranges in laminar to transitional regime the turbulence model should capture transitional, laminar and mild turbulent regions. Nikou [34] showed that the k-ω and BSL models

yielded the lowest mean absolute relative error in predicting dry pressure drop compared to experimental data. In their study the k-ω model demonstrated robust performance across varying flow conditions ($F_g = 0.38 - 1.00$). Therefore, the k-ω model is selected for its demonstrated accuracy and stability in structured packing simulations. The model provides a good resolution in the viscous sublayer at low Reynolds numbers with a blending to the k–ϵ behavior in the free stream [31].

The overall heat of reaction is expressed for the reactive source term as follows:

$$\Delta H^{\circ}_{\mathrm{rxn}} \;=\; \sum_{k} \nu_k \, h^{\circ}_f(k), \tag{4.5}$$

where ν_k and $h^{\circ}_f(k)$ denote the stoichiometric coefficient and the standard heat of formation of species k, respectively.

The chemical source term for reactive absorption is incorporated into the species transport equations as R_i, which represents the local rate of mass consumption or generation due to reaction. The detailed carbamate formation mechanism is demonstrated here into an apparent first-order rate with respect to dissolved CO_2, written in a compact form as:

$$R_{\mathrm{CO_2}} \;=\; -k' \, C_{\mathrm{CO_2}}, \qquad k' = f(T,\, C_{\mathrm{Reactants}},\, C_{\mathrm{Products}}). \tag{4.6}$$

The exothermic heat of absorption is not added as an explicit source term. Instead, it is accounted for through the species formation enthalpies: reactants are assigned $h^{\circ}_f = 0$ (reference), while the products carry a constant offset of $h^{\circ}_f = -8.0 \times 10^7\,\mathrm{J\,kmol^{-1}}$ to reproduce the global heat of reaction. With stoichiometric sources $R_i = \nu_i\, r$ ($\nu_i > 0$ for products, $\nu_i < 0$ for reactants), the reactive heat contribution in the energy equation becomes

$$S_h^{\mathrm{rxn}} = -\sum_i h_i \, R_i = -\sum_i \nu_i h^{\circ}_f(i)\, r \equiv -\Delta H_{\mathrm{rxn}}\, r \tag{4.7}$$

$$\Delta H_{\mathrm{rxn}} = -8.0 \times 10^7\ \mathrm{J\,kmol^{-1}} \tag{4.8}$$

Since the temperature increment along the column is not considerably high, therefore the value of $\Delta H^{\mathrm{eff}}_{\mathrm{rxn}}$ is taken as constant, neglecting temperature and solution non-idealities.

All residuals were set to converge below 1.0×10^{-3}. Although transitional flows sometimes trigger convergence difficulties, the model was provided sufficiently robust iterations and no oscillatory behavior was observed.

A generalized error formulation is given in the below equation 4.9:

$$\epsilon_r = \frac{[CFD\ Results] - [Correlation\ or\ Experimental\ Results]}{[Correlation\ or\ Experimental\ Results]} \tag{4.9}$$

4.4 Property Modeling

4.4.1 Property Correlations for Dry Pressure Drop

According to the data obtained from [16], the density and viscosity values are listed in Table 4.4. Since there is no temperature-dependent solution conducted for Single-phase case, therefore corresponding F_g values were directly assigned in Fluent.

Table 4.4 Operating air gas density and viscosity as a function of temperature and F_g.

T (°C)	F_g ($Pa^{0.5}$)	ρ (kg m^{-3})	μ (Pa s)
18.8	0.719	1.209	1.810×10^{-5}
19.5	1.082	1.206	1.837×10^{-5}
19.6	1.444	1.206	1.837×10^{-5}
19.4	1.803	1.206	1.837×10^{-5}
19.9	2.164	1.206	1.837×10^{-5}
22.2	2.884	1.195	1.838×10^{-5}
25.4	3.603	1.182	1.839×10^{-5}
30.1	4.317	1.164	1.840×10^{-5}

4.4.2 Property Correlations for Two-Phase Model

Table 4.5 summarizes the constant thermophysical properties employed in the CFD simulations for the two-phase model. For the hydrodynamics-only simulations, operating conditions corresponding to $25,^{\circ}\mathrm{C}$ were adopted. In this context, the properties of air at $25,^{\circ}\mathrm{C}$ are reported in Table 4.4 in the previous section.

For the reactive absorption simulations, the material properties were evaluated at an operating temperature of $36,^{\circ}\mathrm{C}$ in order to ensure consistency with the experimental studies of Aroonwilas [19].

It is assumed to be no binary interactions modeled for the system, since the reactive area has very low total reaction amount

Table 4.5 Constant thermophysical properties used in the two-phase model. Water properties at 25°C and 36°C were computed at atmospheric conditions.

Component	ρ kgm^{-3}	μ Pa.s	c_p kJkg^{-1} K^{-1}	k Wm^{-1} K^{-1}	M gmol^{-1}
H_2O @ 25°C[75, 76]	997.3	8.9e-04	4.18	0.61	18.015
H_2O @ 36°C[75, 76]	994	7.1e-04	4.18	0.63	18.015
MEA [76, 77]	1015	2.0e-03	3.20	0.48	61.08
CO_2 @ 36°C[76–79]	1.748	1.5e-05	0.86	0.016	44.01
Air @ 36°C[76–79]	1.142	1.8e-05	1.009	0.027	28.966
Prod 1 (est.)[80, 81]	1200	3.5e-03	3.75	0.48	105.09
Prod 2 (est.)[80, 81]	1050	3.0e-03	3.75	0.48	123.1052

4.4.3 Mixture Property Models

In this work, mixture and transport properties for the reacting MEA–CO_2 system are evaluated using Fluent's built-in mixing laws (Fig. [82]). The selected models are documented in the Appendix via screenshots of the Fluent interface (Fig. A.18). The following section then states the constitutive relations actually used by the solver and summarizes the assumptions underlying each selection.

Thermodynamic non-ideality was not modeled in this study. The liquid phase was treated as an ideal mixture and no binary interaction parameters were introduced in the property model. This simplification is adopted as a scope limitation, since the reactive zone is geometrically short and the overall CO_2 uptake within the simulated domain is small. Therefore, the impact of non-ideal thermodynamics on the reported hydrodynamic and global performance metrics is expected to be secondary compared with the uncertainties associated with flow regime, interfacial area, and mass transfer closure.

4.4.3.1 Density ρ: Volume-Weighted Mixing Law

For a VOF multiphase formulation with N_p phases of (piecewise) incompressible density ρ_q, Fluent evaluates the mixture density as the volume-average

$$\rho_m = \sum_{q=1}^{N_p} \alpha_q \rho_q, \qquad \sum_{q=1}^{N_p} \alpha_q = 1. \tag{4.10}$$

This choice is consistent with the definition of phase volume fractions and preserves the correct hydrostatic response and interfacial jump conditions in VOF.

4.4.3.2 Specific Heat Capacity c_p: Mass-Weighted Mixing Law

Mixture heat capacity at constant pressure follows directly as the mass-weighted average

$$c_{p,m}(T) \;=\; \left(\frac{\partial h_m}{\partial T}\right)_p \;=\; \sum_{i=1}^{N_s} Y_i\, c_{p,i}(T). \tag{4.11}$$

Default mixing-law option and is thermodynamically consistent with the enthalpy formulation used in the energy equation.

4.4.3.3 Thermal Conductivity: Mass-Weighted Mixing Law

When the "mass-weighted mixing law" is selected for laminar conductivity,

$$k_m \;=\; \sum_{i=1}^{N_s} Y_i\, k_i, \tag{4.12}$$

and the conductivity appearing in the energy equation is

$$k_{\text{eff}} \;=\; k_m \;+\; k_t, \tag{4.13}$$

where k_t is the turbulent conductivity from the selected turbulence model (via $k_t = \mu_t c_p / \mathrm{Pr}_t$ with turbulent Prandtl number Pr_t). Mass-averaging is recommended for reacting liquid mixtures where property contrast between components tracks composition by mass.

4.4.3.4 Viscosity: Mass-Weighted Mixing Law

With the 'mass-weighted mixing law' for laminar viscosity,

$$\mu_m \;=\; \sum_{i=1}^{N_s} Y_i\, \mu_i, \tag{4.14}$$

and the momentum equations use the effective viscosity

$$\mu_{\text{eff}} \;=\; \mu_m \;+\; \mu_t, \tag{4.15}$$

with μ_t supplied by the turbulence closure. The mass-weighted law provides a consistent baseline tied to composition.

4.4.3.5 Basis for the Surface Tension

Surface tension values were prescribed to represent the liquid phase properties used in the simulations. For both water and aqueous MEA, σ was treated as constant because the temperature variation along the absorber was negligibly small.

Table 4.6 Surface tension values used in the present work.

Fluid	Temperature (°C)	σ (N m^{-1})	Reference
Water	25	0.072	[83]
Aqueous MEA (20 wt%)	36	0.055	[66]

4.4.3.6 Mass Diffusivity: Multicomponent

ANSYS Fluent solves the Maxwell–Stefan form of multicomponent diffusion for all transported species simultaneously when the *Multicomponent* option is selected. Using the set of binary diffusion coefficients D_{ij}, the solver internally computes the coupled diffusive mass fluxes, thereby capturing cross-diffusion effects without extra model parameters beyond the supplied D_{ij}. The material-interface selections (mixture species, reaction model, and mixing laws for density, heat capacity, conductivity, viscosity, and diffusivity) are documented in Fig. A.18.

4.4.3.7 Basis for the binary diffusivities

For neutral–neutral pairs (e.g., CO_2 in water, MEA in water), representative magnitudes follow the Stokes–Einstein scaling and the Wilke–Chang correlation; for ionic amine–CO_2 reaction products (e.g., carbamate/bicarbonate with aminium counter-ions), reduced values in the 10^{-10} m^2/s range are used.

$$D_{AB} \;=\; \frac{k_{\mathrm{B}}\,T}{6\pi\,\mu_B\,r_A}, \tag{4.16}$$

$$D_{AB}\;[\mathrm{cm}^2/\mathrm{s}] \;=\; 7.4\times10^{-8}\;\frac{(\phi_B\,M_B)^{1/2}\,T}{\mu_B\,V_A^{0.6}}, \tag{4.17}$$

where k_{B} is the Boltzmann constant, T the absolute temperature, μ_B the solvent viscosity, r_A the solute hydrodynamic radius, ϕ_B the solvent association factor (for water ≈ 2.6), M_B the solvent molar mass, and V_A the solute molar volume at its normal boiling point.

These diffusivities were specified as constants to the Fluent for the operating temperature ranging 308–312 K; multicomponent fluxes are then assembled internally from the binary inputs during the coupled species-transport solution.

Table 4.7 Binary liquid-phase diffusion coefficients used in the multicomponent (Maxwell–Stefan) model.

Species Pair	D_{ij} [m^2 s^{-1}]	Reference
$H_2O_{(L)} \leftrightarrow CO_2$	1.9×10^{-9}	Eq. (4.16)
MEA $\leftrightarrow H_2O_{(L)}$	8.0×10^{-9}	Eq. (4.17)
$H_2O_{(L)} \leftrightarrow$ Product (ionic)	4.0×10^{-10}	Eq. (4.16)
MEA $\leftrightarrow CO_2$	2.3×10^{-9}	Eq. (4.17)
Product (ionic) $\leftrightarrow CO_2$	1.0×10^{-9}	Eq. (4.17)
MEA $\leftrightarrow$ Product (ionic)	6.0×10^{-10}	Eq. (4.16)

4.5 Reactive Absorption Methodology

4.5.1 Framework Development

At each time step, the incompressible two-phase flow is advanced with a VOF formulation, updating the velocity–pressure fields and the phase indicator; this resolves the gas–liquid interface and yields the interfacial area density a_i needed by the mass-transfer model. Given the gas-side composition y_{CO_2} and the absorber pressure P_{abs}, the interfacial partial pressure is $p_{CO_2} = y_{CO_2} P_{abs}$. In this manner, the corresponding liquid-side equilibrium composition is obtained via the temperature-dependent Henry relation shown in the equation (3.32).

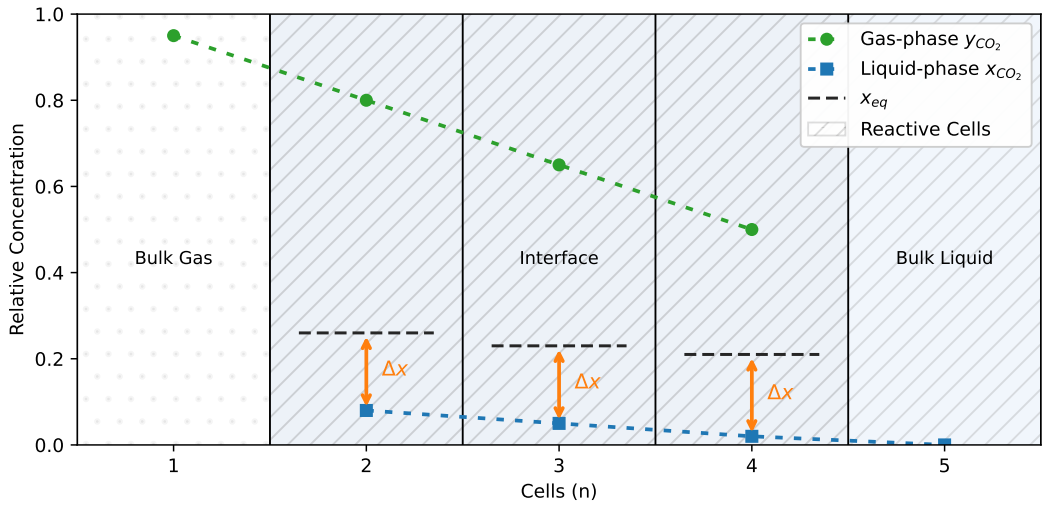


Figure 4.5 Reactive absorption framework developed for the study

Figure 4.5 summarizes the end-to-end framework that links the hydrodynamics (VOF), interfacial thermodynamics, and reactive mass transfer.

The driving force for absorption Δx is $x_{eq} - x_{CO_2}$, where x_{CO_2} is the local dissolved CO_2 composition in the liquid phase. The interfacial molar flux is modeled with a

film coefficient and interfacial area density, and is introduced as a volumetric source term in the CO_2 transport equation within interfacial and liquid cells.

In the reactive cells, the absorbed CO_2 is consumed through the CO_2–MEA reaction kinetics (See reaction in the Eqn. (3.22)). This consumption establishes a net sink for CO_2, while generating a corresponding source term for the reaction products according to the defined stoichiometry. Furthermore, the reaction enthalpy contributes to the energy equation through a volumetric heat source.

Species equations are solved with these sources to update the liquid composition and temperature fields. The procedure is repeated in time: VOF updates the interfacial geometry and a_{int}, interfacial equilibrium supplies x_{eq}, and the UDF-based coupling converts the interfacial flux into volumetric sources/sinks. This loop continues until the pseudo–steady regime is achieved.

Reaction calculations were coupled with an ideal mixture property model; non-ideality effects were not considered (see Section 4.4.3).

4.5.2 Volumetric Reaction Definition

In the CFD framework, the CO_2–MEA reaction was represented as two volumetric reaction between the reactants CO_2, MEA and H_2O, yielding $Carbamate$ and $Bicarbonate$ products. The rate followed an Arrhenius form as implemented in ANSYS Fluent, with the kinetic constants summarized in Table 4.8. The volumetric reactions defined to the ANSYS Fluent given in the Appendix A.20 and A.21.

The parameters implemented in the present model are summarized below, consistent with the references used [19, 38]:

Table 4.8 Kinetic parameters used for CO_2–MEA reactions.

Reaction	A ($m^3\,kmol^{-1}\,s^{-1}$)	E_a ($J\,kmol^{-1}$)
$CO_2 + 2MEA \rightarrow MEACOO^- + MEAH^+$	4.61×10^9	3.74×10^7
$CO_2 + H_2O + MEA \rightarrow MEACOO^- + 2H^+$	2.73×10^7	4.55×10^6

Since the direct carbamate formation (R1) is significantly faster, it governs the initial absorption rate, while the hydrated CO_2 route (R2) acts as a secondary, slower path contributing mainly at lower amine concentrations or high CO_2 loadings. These kinetic formulations are explicitly incorporated into the CFD model via user-defined source terms in the mass transport equations.

The kinetic expressions given above were implemented in the ANSYS Fluent reaction module as two volumetric reactions, as illustrated in Appendix A.20–A.21. These configurations define the rate constants, reactant exponents, and Arrhenius parameters consistent with the kinetic data summarized in Table 4.8.

4.5.3 Mass Transfer Definition

Interfacial absorption is modeled through a volumetric source term applied exclusively within the VOF interfacial cells. As detailed in Section 4.5.1 and summarized in Algorithm 1 (provided in the Appendix), the model evaluates the local CO_2 mass flux based on instantaneous gas–liquid compositions, pressure, and temperature, employing a temperature-dependent Henry constant. The liquid-side mass-transfer coefficient, $k_{L,0}$, is assumed to be spatially and temporally constant.

All numerical safeguards such as clamping/bounding of α_g, domain filtering, and are handled within the UDF routine. The setup in ANSYS Fluent, including the phase-interaction UDF assignment and species coupling, is shown in Figure A.19.

Table 4.9 Other thermodynamic, transport, and model parameters used in the mass-transfer UDF.

Parameter	Value	Units	Notes / source
$k_{L,0}$	1.24×10^{-3}	m s^{-1}	Physical liquid-side coefficient [40, 46].
$H_{cp,ref}$	3.6×10^{-4}	mol m^{-3} Pa^{-1}	Henry solubility constant at T_{ref}; CO_2 in water [71].
β	2300	K	Temperature dependence parameter 3.34; typical literature values for CO_2 in water [71].
T_{ref}	298.15	K	Henry reference temperature [71].
a_0	500	m^2 m^{-3}	Nominal packing specific area for Mellapak 500.Y packing.

4.6 Initialization and Boundary Conditions

The initialization and boundary conditions were defined separately for the single phase, two-phase non-reactive, and two-phase reactive simulation sets. The single phase cases were used exclusively for dry pressure drop calibration, whereas the two phase cases incorporated liquid loading and explicit tracking of the gas liquid interface. The reactive absorption cases further included liquid loading, interface tracking, volumetric reaction kinetics, and interphase mass transfer submodels.

4.6.1 Single Phase Boundary Conditions

For the single–phase pressure–drop simulations, the flow field was initialized using the "Hybrid Initialization" scheme available in ANSYS Fluent. For this case, no custom field initialization or profile mapping was applied; all variables were initialized from the hybrid solution.

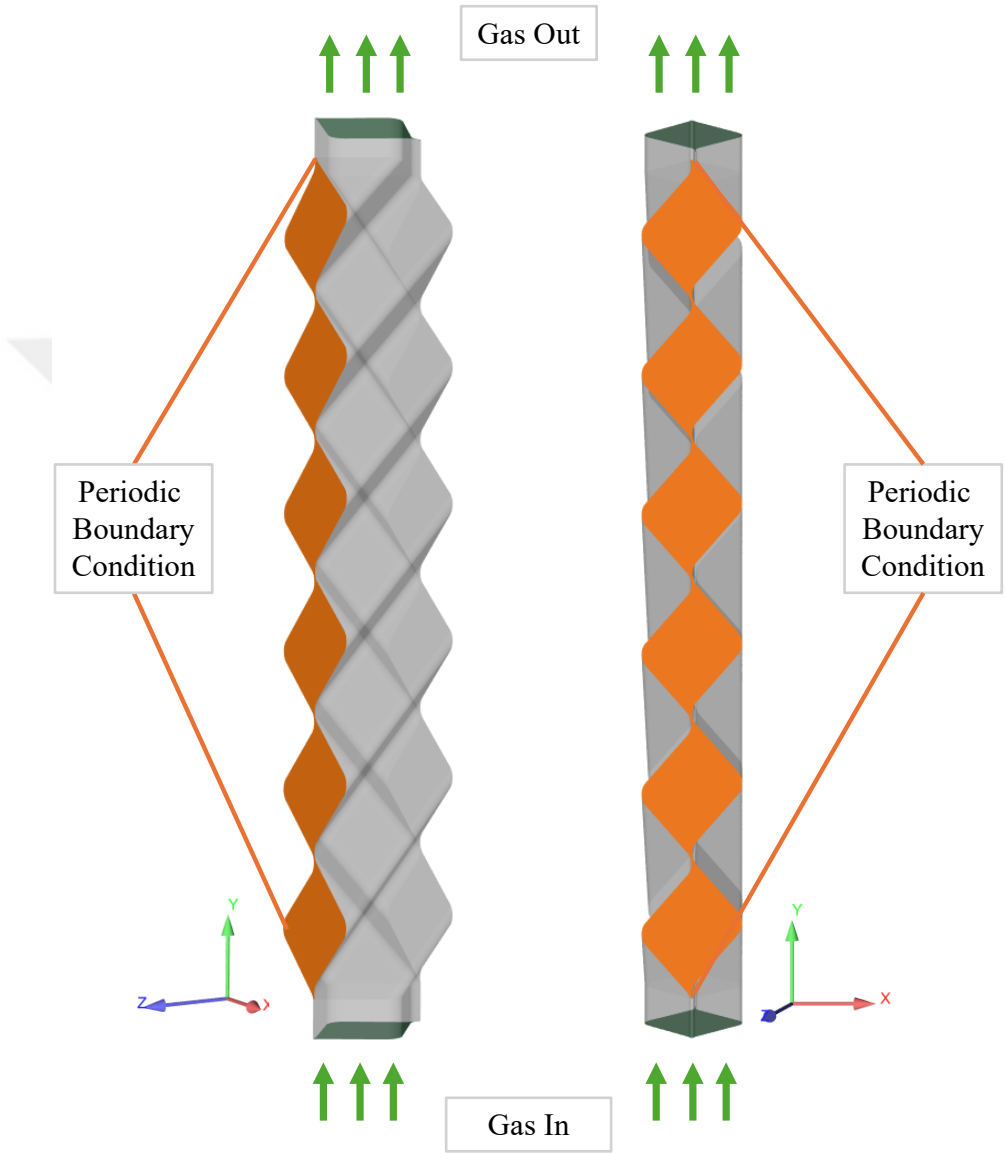


Figure 4.6 Multiple-REU's of Mellapak 500.Y. and associated boundary conditions for gas pressure drop

4.6.2 Two-Phase: Non-Reactive Hydrodynamics Boundary Conditions

The first time step was resolved with $\alpha_i = 0$ that filled with gas at $t = 0$. The inlet velocity (gas-phase) defined as in terms of m/s. In liquid inlet boundary condition, liquid injected through demonstrated region (Figure 4.7 with $\alpha = 1$ in terms of mass flux. Moreover, no-slip boundary condition is applied to the surface of the

walls in the area of interest (i.e. packing walls). Periodic boundary conditions are assigned to the repeating section (lateral sides) of the REU 4.7. Constant pressure was applied to the domain as $1\ atm$. There is no liquid allowed to escape from the gas outlet boundary. In other words liquid carry-over was prevented. Time step is dynamically adjusted to satisfy the Courant-Friedrichs-Lewy criterion 4.18:

$$\mathrm{CFL} = \frac{u\,\Delta t}{\Delta X} \leq 1 \tag{4.18}$$

Figure 4.7 shows a single REU extracted from the periodically repeating section of the packing. The lateral faces closed with *periodic* boundary conditions, ensuring fully-developed flow while permitting a constant driving pressure drop ΔP_{wet} across the cell.

Counter-current operation is integrated such that flue gas enters through two upper *velocity-inlet* slots at superficial velocity u_G and leaves through the opposing outlets, while the solvent film is introduced at the top of the corrugation via a *mass-flux inlet* that applies a prescribed interfacial mass flux L and subsequently drains from the lower edge.

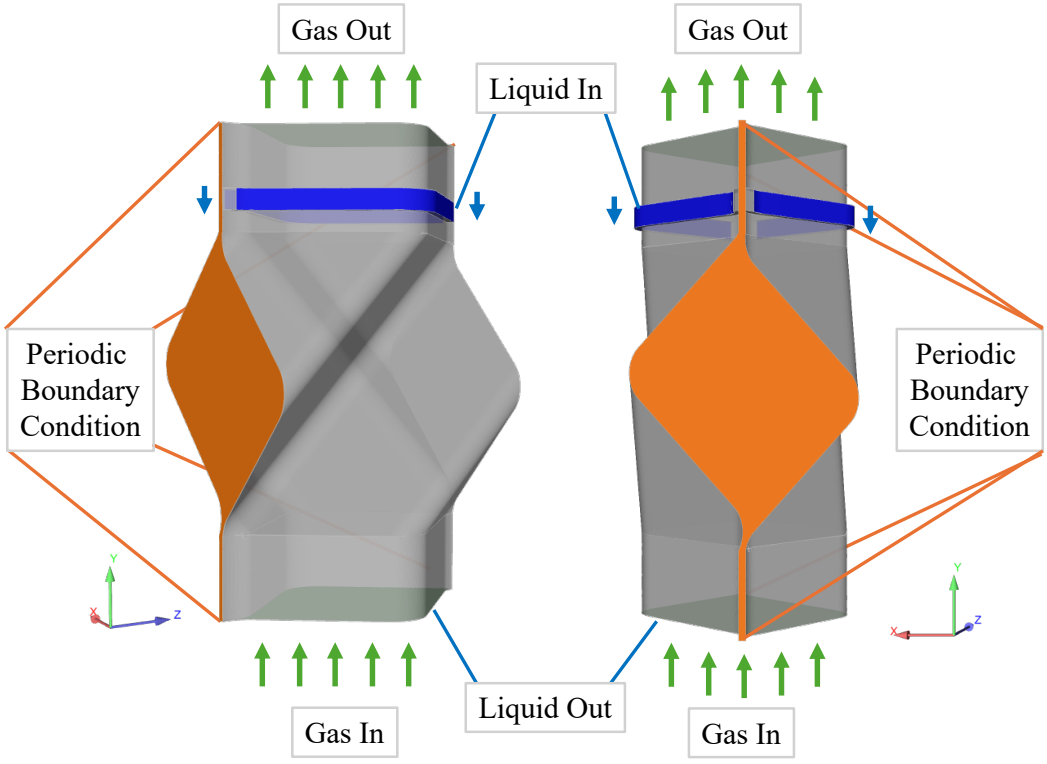


Figure 4.7 Single representative elementary unit (REU) of Mellapak 500.Y. and associated boundary conditions for two-phase studies

The equalities for the boundaries are given in the following equations,

Liquid inlet (Blue):

$$u\big|_{\text{liq-in}}(x,y,z) = u_L(x,y,z), \qquad \alpha_L\big|_{\text{liq-in}} = 1 \tag{4.19}$$

Gas inlet (Green):

$$u\big|_{\text{gas-in}}(x,y,z) = u_G(x,y,z), \qquad \alpha_L\big|_{\text{gas-in}} = 0 \tag{4.20}$$

Sides (Orange) – periodic:

$$\phi(0,y,z) \;=\; \phi(L_x,y,z), \qquad \forall\,\phi \in \{u,\alpha_L,p,\theta\} \tag{4.21}$$

Sides (Orange) – periodic:

$$\phi(x,y,0) \;=\; \phi(x,y,L_z), \qquad \forall\,\phi \in \{u,\alpha_L,p,\theta\} \tag{4.22}$$

Packing sheets (grey):

$$\left.\begin{aligned} u\big|_{\text{packing walls}} = 0, \quad \theta\big|_{\text{packing walls}} = \theta_{\text{wall}} \end{aligned}\right\} \qquad \text{Packing sheets (grey)} \tag{4.23}$$

$$p\big|_{\text{out}} = 1\ \text{atm} \qquad \text{Outlet (green)} \tag{4.24}$$

4.6.3 Two-Phase: Reactive Absorption Boundary Conditions

Aroonwilas [19] experimental data were used to calculate the CFD operating conditions by employing the measured liquid loading L and gas-phase mole-fraction change Δy. First, the column diameter $D = 0.10\ \mathrm{m}$ was used to compute the cross-sectional area as follows:

$$A_c = \tfrac{\pi}{4}\, D^2. \tag{4.25}$$

Each L value (in $\mathrm{m^3/m^2 \cdot h}$) was converted to a liquid volumetric flow rate

$$Q_L = \frac{L}{3600}\, A_c, \tag{4.26}$$

and, with the known MEA concentration $C_{\mathrm{MEA}} = 3\,\mathrm{kmol/m^3}$ and CO_2 loading $\alpha = 0.40\ \mathrm{mol/mol}$ [19], the liquid-phase molar flows $\dot{n}_{\mathrm{MEA}}$ and $\dot{n}_{\mathrm{CO_2}}$ were determined.

The experimental gas-phase change Δy then yielded the total gas molar flow via the following equation:

$$\dot{n}_G = \frac{\dot{n}_{\mathrm{CO_2}}}{\Delta y}. \tag{4.27}$$

Finally, the ideal-gas law applied,

$$Q_G = \frac{\dot{n}_G\, R\, T}{P}, \quad u_G = \frac{Q_G}{A_c}, \tag{4.28}$$

provided the superficial gas velocity u_G and volumetric flow rate Q_G for each case, which were imposed as the CFD inlet and operating boundary conditions to replicate the pilot-scale operating range.

As described in the previous section and illustrated in Figure 4.7, the identical boundary conditions were applied in the single-REU model. Specifically, the gas–liquid inlet and outlet locations, as well as the periodic boundaries, follow exactly the setup outlined above.

The velocity, volume–fraction and pressure boundary conditions are identical to those given in Section 4.6.1; only the species sets differ. Below, new equations are provided exclusively for the reactive absorption boundary conditions.

Liquid inlet (blue): The entering solution contains free MEA, pre-formed MEA–carbamate and water:

$$\begin{aligned} C_{\mathrm{MEA}}\big|_{\text{liq-in}} &= (1-\alpha_0)\, C_{\mathrm{MEA},0}, \\ C_{\mathrm{Carb}}\big|_{\text{liq-in}} &= \alpha_0\, C_{\mathrm{MEA},0}, \\ C_{\mathrm{H_2O}}\big|_{\text{liq-in}} &= C_{\mathrm{H_2O},0}, \end{aligned} \tag{4.29}$$

where $C_{\mathrm{MEA},0}$ is the total amine concentration ($\mathrm{kmol\,m^{-3}}$) and α_0 is the lean loading ($\mathrm{mol\ CO_2/mol\ MEA}$).

Gas inlet (green): A binary mixture of CO_2 and air (modelled as a single inert component) is imposed:

$$y_{\mathrm{CO_2}}\big|_{\text{gas-in}} = y_{\mathrm{CO_2,in}}, \qquad y_{\mathrm{air}}\big|_{\text{gas-in}} = 1 - y_{\mathrm{CO_2,in}}. \tag{4.30}$$

Periodic boundaries (orange): Species fields obey the same periodicity applied to the flow variables:

$$\begin{gathered}\phi_s(0,y,z)=\phi_s(L_x,y,z), \qquad \phi_s(x,y,0)=\phi_s(x,y,L_z),\\ \forall\,\phi_s\in\{C_{\mathrm{Reactants}},C_{\mathrm{Products}},y_{\mathrm{CO_2}},y_{\mathrm{air}}\}.\end{gathered} \tag{4.31}$$

Packing walls (grey): No-flux (impermeable and non-reactive) conditions are assumed:

$$\mathbf{n}\cdot\nabla\phi_s\big|_{\text{packing walls}}=0, \qquad \forall\,\phi_s. \tag{4.32}$$

Outlet (green): A zero-gradient condition is prescribed for all species:

$$\mathbf{n}\cdot\nabla\phi_s\big|_{\text{out}}=0, \qquad \forall\,\phi_s. \tag{4.33}$$

Equations (4.29)–(4.33), together with the hydrodynamic boundary set, fully define the inlet, periodic, wall and outlet constraints for the MEA–H_2O/Carbamate Bicarbonate and CO_2–Air reactive absorption simulations.

4.7 Post-Processing and Derived Quantities

The definitions below describe the post-processing procedure through which the hydrodynamic and mass transfer metrics used in this study are extracted from the VOF fields.

4.7.1 Liquid Holdup

Below equation (4.34), h_L is the cell-averaged liquid holdup, obtained by volume-integrating the VOF liquid volume fraction α_L over each computational cell.

$$h_L=\frac{1}{V_{\text{cell}}}\int_{V_{\text{cell}}}\alpha_L\,\mathrm{d}V \tag{4.34}$$

4.7.2 Pressure Drop per Unit

To ensure that the liquid film does not distort the result, the pressure gradient is formed from cell–centre pressures (which are averaged) that belong exclusively to

the pure-gas subset ($\alpha_G = 1$) given in the following equation (4.35) that are used both in single-phase and two-phase studies:

$$\left(\frac{\Delta P}{z}\right) = \frac{p_{G,in} - p_{G,out}}{z} \tag{4.35}$$

4.7.3 Interfacial Area

In the following equation (4.36), a_{int} is the specific interfacial area, defined as the total gas–liquid interface area S_{int} normalised by the domain volume.

$$a_{int} = \frac{1}{V_{\text{domain}}} \int_{S_{\text{int}}} \mathrm{d}S \tag{4.36}$$

5
RESULTS AND DISCUSSION

5.1 Single Phase Hydrodynamics

Firstly, a detailed mesh-sensitivity analysis was performed across a broad range of gas loads.
Secondly, to minimize the computational cost and effort of two-phase simulations, single-phase hydrodynamic analyses were first performed in order to investigate an optimal mesh size. Since there is no consensus in the literature regarding the face-to-face spacing (gap), number of REUs or number of Prism Layers, initial investigations focused on pressure-drop studies. For this purpose, experimental data and correlation parameters from Tsai [16] were incorporated into the Stichlmair [30] correlation.
Lastly, the post-processing results are presented in a single figure for a mid-range gas load.

5.1.1 Mesh Sensitivity Analysis

Mesh sensitivity analyses were performed across various parameters, including the number of prism layers, total cell count, and the number of REUs. Although the following section focuses on low gas loads ($F_g \approx 0.5$–1.5), the pressure-drop range is maintained broadly to capture the complete fluid behavior within the packing.

Grid independence was evaluated by benchmarking the predicted dry unit pressure drop against the semi empirical correlation of Stichlmair et al. [30] over the full gas load range reported by Tsai [16]. With the exception of the coarsest grid, all meshes reproduced the correlation within $\pm 20\%$, and the solutions obtained on the refined grids were essentially indistinguishable.

Across all cases, the simulations captured the expected monotonic increase of ΔP with F_G. In particular, the three finest discretizations (3.2M, 3.5M, and 7.1M cells) yielded pressure drop curves that practically overlap throughout the operating

window. The corresponding deviations from the Stichlmair et al. [30] reference remain within approximately 10% for most gas loads and show no consistent tendency toward underprediction. The intermediate 2.4M grid exhibits slightly larger deviation, whereas the 0.7M grid produces the largest discrepancies, most notably at high gas loads where the error exceeds 20%.

Overall, the results indicate that the pressure drop response of the representative packing unit can be predicted with high fidelity without employing the most computationally expensive mesh. The close agreement between the 3.2M and 3.5M grids, together with their consistent alignment with the Stichlmair et al. [30] correlation, suggests that a resolution on the order of 5×10^5 cells for each REU is sufficient for mesh independent pressure drop predictions. Further refinement to 7.1M and 13.2M cells does not provide a measurable improvement in correlation error, while it would substantially increase computational cost. In contrast, the pronounced overprediction observed for the 0.7M grid at high F_G indicates that overly coarse discretization distorts the inertial contribution within the inclined channels. Accordingly, the $\approx$ 0.5M cells per REU grid is selected as the best compromise between accuracy and computational efficiency.

The grid sensitivity study also highlights a change in the ΔP versus F_G slope around $F_G \approx 0.8$ to 1.0, which is consistent with a transition from predominantly laminar behavior toward transition or turbulence dominated flow in the inclined channels. In this regime, the gas phase Reynolds number increases such that inertial effects progressively outweigh viscous dissipation, and the ΔP response steepens. The CFD results reproduce this behavior as a marked amplification of the ΔP–F_G characteristic, where modest increases in gas load induce a disproportionate, near exponential rise in pressure drop, consistent with experimental observations for dry structured packings [16, 26, 27, 30].

Finally, experimental study [16] reported that, even for the original air water database, the Stichlmair et al. [30] correlation represents structured packing hydraulics only within finite experimental scatter, with typical deviations on the order of 10% to 20%. Therefore, the residual mismatch between the present CFD predictions and the correlation is compatible with the intrinsic uncertainty of the reference model.

5.1.2 Number of Prism Layers

Fig. 5.3 examines how near-wall prism layers affect the predicted dry pressure drop in the REU of Mellapak 500.Y. All three meshes have comparable total sizes ($\approx$

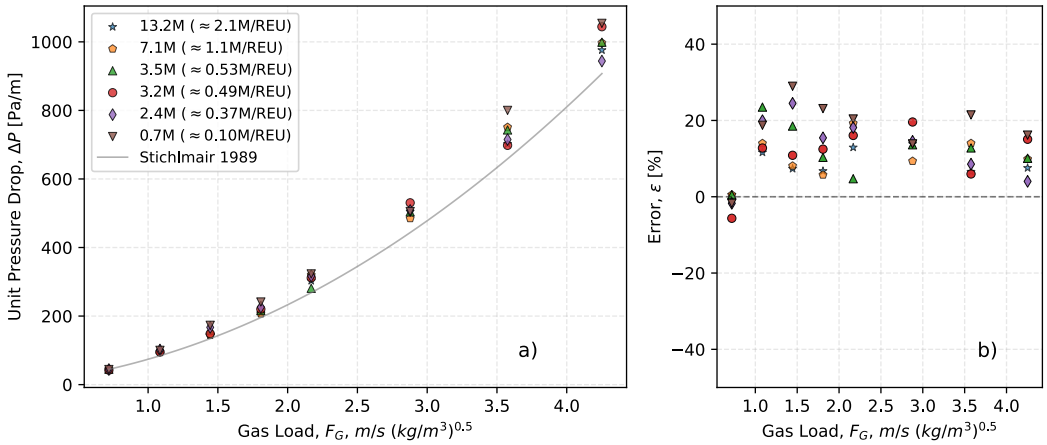


Figure 5.1 Dry unit pressure drop across different number of cells. Panel (a) compares numerical predictions with the Stichlmair et al. [30] correlation as a function of gas load F_G. Panel (b) Corresponding relative deviation from the correlation.

0.53M cells per REU) but differ in boundary-layer treatment, employing either zero, eight, or twelve prism layers adjacent to solid surfaces. As shown in panel (a), each mesh captures the expected monotonic rise of unit pressure drop with increasing gas load and reproduces the overall trend of the Stichlmair correlation [30] across the full operating range. The relative deviations in panel (b) remain within about 20% for all gas loads and prism-layer configurations, and no consistent improvement is observed when prism layers are introduced.

For the present REU geometry, the baseline mesh already provides near-wall resolution at the sublayer level, with y^+ values on the order of two even for the coarsest grid. Consequently, adding a dedicated boundary-layer mesh does not materially change the predicted dry pressure drop within the tested range, and comparisons among the 0, 8, and 12 prism-layer configurations indicate only marginal differences in integral quantities. This outcome is consistent with earlier REU-based studies [31, 33], where near-wall fidelity is achieved primarily through sufficiently fine global refinement rather than explicit inflation layers.

On this basis, the mesh without prism layers was selected as the reference configuration for the subsequent dry-flow parametric study, since it delivers essentially the same level of agreement with the correlation while simplifying mesh generation. Overall, the dry-flow results suggest that once adequate bulk resolution is attained, prism-layer addition has limited impact on the predicted unit pressure drop.

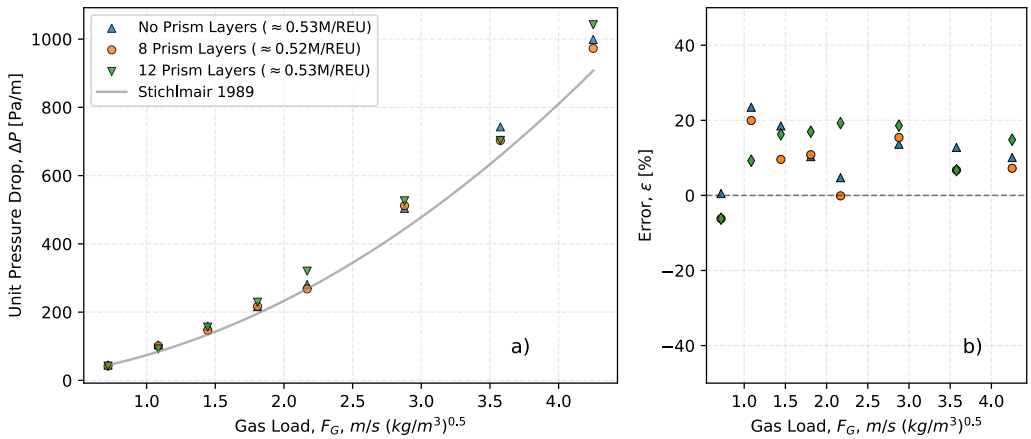


Figure 5.2 Effect of near-wall prism layers on the predicted dry unit pressure drop in the Mellapak 500.Y REU. (a) Meshes with 0, 8, and 12 prism layers compared against the Stichlmair et al. [30] correlation versus gas load F_G. (b) Corresponding relative deviation from the correlation.

5.1.3 Effect of Number of REUs

Fig. 5.3 evaluates the sensitivity of the predicted dry unit pressure drop to the computational domain length, expressed by the number of REUs. Although the total cell count increases by approximately a factor of six from the single REU case to the six REU case, all configurations closely track the Stichlmair correlation [30] and remain within roughly 20% over the investigated gas load range. Extending the domain from one to four or six REUs primarily introduces a minor offset in the pressure drop level, while the overall curve shape and the slope with respect to gas load are essentially preserved.

The corresponding deviation plot in Fig. 5.3(b) indicates relative errors that typically fall between 0 and 25 percent, without a consistent monotonic dependence on the number of REUs. At any given gas load, the spread among the three domain lengths is generally below about 10 percent, which is comparable to the experimental scatter reported for dry pressure drop measurements of Mellapak 500.Y [16]. These observations support the robustness of the periodic unit cell assumption and suggest that a single REU is sufficient to capture representative dry gas phase hydrodynamics.

From a practical standpoint, adopting a single REU reduces the mesh size by about a factor of six relative to the six REU domain, while yielding only marginal gains in agreement with the correlation. Accordingly, a one REU domain is selected for the subsequent parametric study as a balanced choice between accuracy and computational cost, whereas extended domains may be retained for targeted

validation cases or future two phase simulations that explicitly resolve liquid flow and potential maldistribution.

However, it is acknowledged that reducing the number of REUs may broaden the variability band observed in transient predictions, as shorter domains provide less spatial averaging and can amplify instantaneous deviations. Nevertheless, the one REU configuration is still considered appropriate for the intended pseudo steady state comparisons, because it provides a meaningful trade off between computational expense and accuracy for the present scope, while preserving the correct mean pressure drop response and trends with gas load.

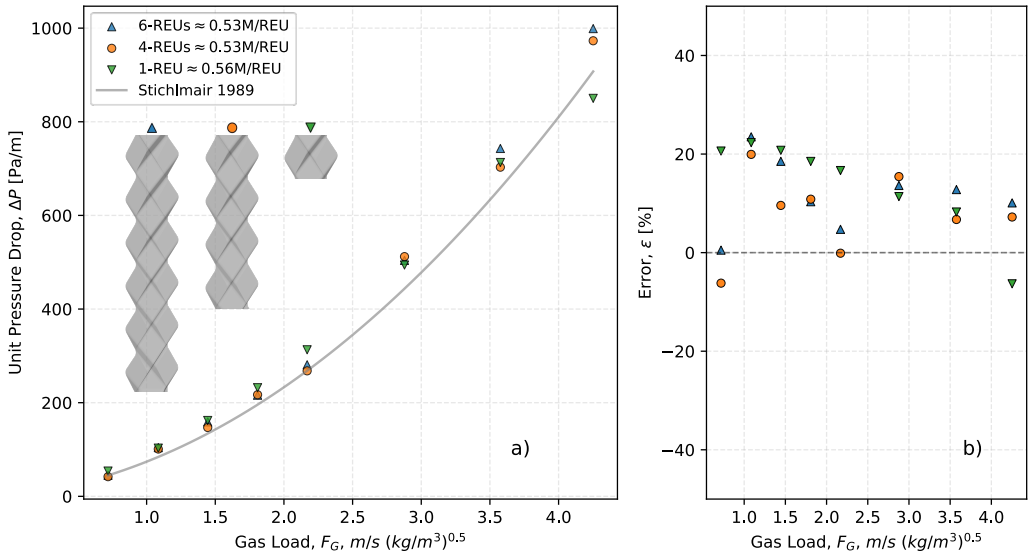


Figure 5.3 Dry unit pressure drop in Mellapak 500.Y REUs with 1, 4, and 6 repeating units at similar cell counts per REU. (a) CFD predictions compared with the Stichlmair et al. [30] correlation versus gas load F_G. (b) Corresponding relative deviation from the correlation.

5.1.4 Effect of Sheet Spacing

In previous studies [10, 11, 33], a face to face sheet spacing of 2 mm was commonly adopted; however, this geometric value does not provide an adequate basis for dry pressure drop calibration in the present idealized REU model. As shown in Fig. 5.4, all CFD cases reproduce the expected monotonic increase of dry unit pressure drop with gas load, yet the predicted magnitude is highly sensitive to the assumed sheet gap. For the smallest effective spacing of 0.24 mm, the numerical results closely follow the dry air experiments reported by Tsai [16] across the full operating window and remain consistent with the Stichlmair correlation [30], with particularly good agreement at medium and high gas loads where both references indicate a strong increase in pressure drop with F_G.

In contrast, larger face to face distances lead to a systematic under prediction of the pressure drop. At a spacing of 0.40 mm, the simulations capture the qualitative trend but remain below both the experiments and the correlation, with deviations that increase with gas load. The 2.00 mm case exhibits the largest discrepancy; at high gas loads, the computed unit pressure drop is approximately two to three times lower than the values suggested by Tsai [16] and Stichlmair [30]. To keep the comparison on an equal numerical basis, the meshes were generated with similar total cell counts.

These findings indicate that the effective sheet spacing is the dominant geometric control parameter for dry pressure drop within the present REU representation. The calibrated value of 0.24 mm can be interpreted as an effective spacing that compensates for unresolved geometric details, including sheet overlap, local contact and junction regions, manufacturing tolerances, and surface roughness, which are not represented explicitly in the REU geometry. Therefore, a 0.24 mm face to face sheet distance was adopted throughout this work to ensure accurate dry pressure drop predictions.

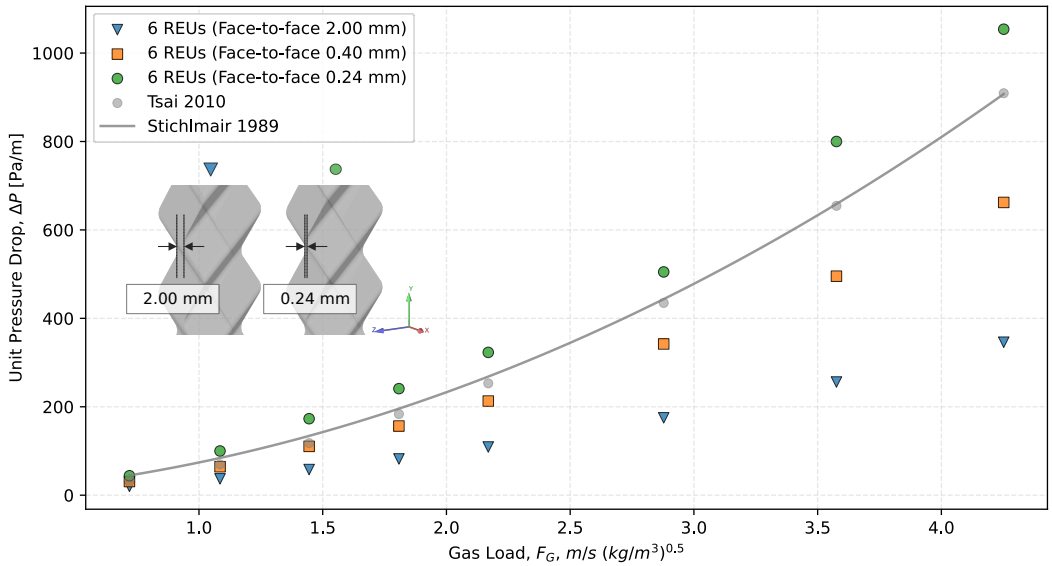


Figure 5.4 Dry unit pressure drop across 6 REUs versus gas load F_G for three face-to-face sheet spacings. Markers indicate CFD results for 2.00, 0.40, and 0.24 mm, grey circles show Tsai [16] experimental data, and the gray line denotes the Stichlmair [30] correlation.

5.2 Two-Phase Non-Reactive Hydrodynamics

All two-phase simulations were conducted using a single-REU mesh approach in order to speed up simulation time. The oscillated behavior of liquid was shown with

upper, lower and an average value of the error bars for the two-phase hydrodynamics investigation.

5.2.1 Model Selection

Accordingly, the final mesh was selected by balancing numerical accuracy and computational cost through a grid sensitivity analysis conducted on multiple two phase metrics, with particular attention to capillary dominated interfacial behavior. This multi criteria approach ensured that the adopted model offers a reliable accuracy versus cost trade off for the remainder of the study. Moreover, this multi-metric grid sensitivity framework enables identification of the quantity that imposes the most stringent mesh requirement, therefore demonstrating where increased spatial resolution is most critical and where additional refinement yields diminishing returns.

5.2.2 Mesh Sensitivity Analysis

A grid dependence test was performed for four different mesh densities, approximately 0.26×10^6, 0.44×10^6, 0.71×10^6, and 1.02×10^6 cells per REU. For the first two meshes, a high near-wall resolution was maintained without prism layers, whereas the remaining meshes employed 8 and 12 prism layers to better resolve near-wall gradients. As highlighted in the dry pressure-drop assessment, the base REU model already contains a relatively high cell count; therefore, evaluating prism-layer-free configurations is computationally meaningful and does not necessarily compromise the accuracy of the key bulk metrics. In addition, omitting prism layers allows the time step to be chosen more flexibly while keeping the Courant–Friedrichs–Lewy (CFL) number sufficiently low, which significantly improves the overall computational efficiency in transient two-phase simulations. The analysis conducted for the following sections such as:

- Liquid holdup,
- Wet pressure drop,
- Relative interface area.

This type of grid sensitivity analysis offers a more comprehensive approach, particularly in identifying which sections require higher computational effort.

5.2.2.1 Liquid Holdup Sensitivity Analysis

In the liquid holdup sensitivity analysis, Figure 5.5a, predicted liquid holdup values are effectively mesh-independent, and the corresponding error bars in panel Figure 5.5b. the simulation results recorded between 0.4 s and 0.8 s are represented by error bars: the midpoint of each bar corresponds to the mean value over this interval, while the upper and lower bounds denote the maximum and minimum values observed within that time window, respectively. Figure 5.5, each mesh qualifies as a valid candidate for further validation studies; M2 (0.44×10^6 cells/REU) was selected to ensure a conservative safety margin in the validation study.

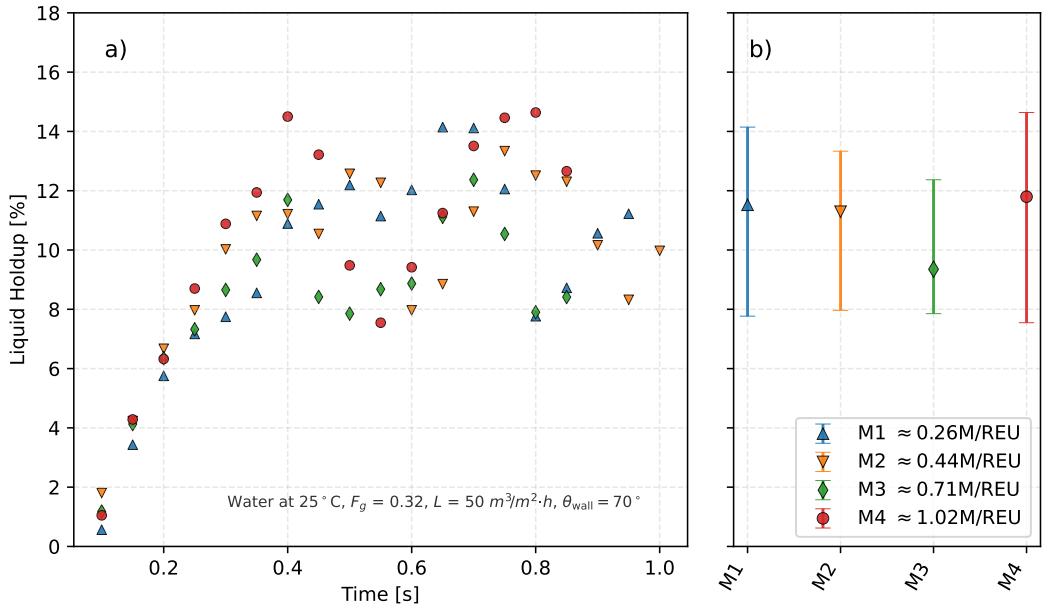


Figure 5.5 Liquid holdup sensitivity analysis with minimum maximum and mean values

5.2.2.2 Wet Pressure Drop Sensitivity Analysis

The same mesh models described in the liquid holdup sensitivity analysis were employed. The pressure drop decreases markedly as liquid discharges from the REU, but when liquid holdup within the REU is high, the pressure drop correspondingly increases as in the Figure 5.7a. Additionally, as shown in Figure 5.7b, mesh independence is observed between M3 and M4, whereas M1 and M2 exhibit notable discrepancies. Coarser meshes (M1 and M2) predict significantly higher wet pressure drop values, while the finest meshes (M3 and M4) yields the lower pressure drop. Furthermore, increasing the gas flow rate might amplify the difference between the coarse and fine meshes, particularly between M3–M4 and M1.

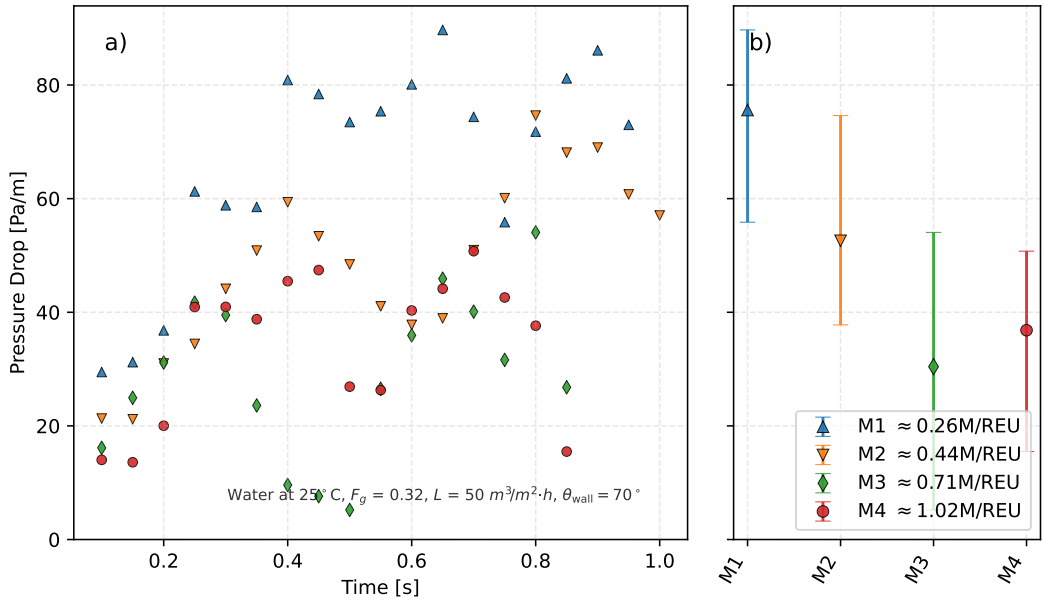


Figure 5.6 Wet pressure drop sensitivity analysis with minimum maximum and mean values

5.2.2.3 Interface Area Sensitivity Analysis

The relative interface area exhibits behavior closely correlated with liquid holdup: as holdup increases, the interface area increases, and vice versa. The finest mesh (M4) with prism layers demonstrates slightly higher average and maximum interface areas compared to the coarser mesh (M1), although the difference remains modest. Moreover, after the interface is first wetted at 0.4 s, the second wetting cycle around 0.7 - 0.8 s yields an even larger interface area, likely due to enhanced surface wettability.

5.2.3 Liquid Holdup

In this section, we briefly introduce the investigation of liquid load, gas load, and static contact angle. Among all validation metrics, liquid holdup is one of the most commonly compared parameter. Consequently, in the two-phase hydrodynamics part of the study, liquid holdup is selected as the primary variable for the analysis.

To benchmark liquid holdup correlations, the empirical expressions proposed by Spiegel and Sues [2], Olujic et. al.,[23] and the geometry-based formulation of Billet-Schultes [1], were implemented and evaluated over a representative liquid-load range of L = 5-150 $\mathrm{m^3\,m^{-2}\,h^{-1}}$ for the properties of water at 25°C. Figure 5.8 demonstrates this correlations in a single plot. Spiegel [2] and Olujić [23] correlate only the dynamic film holdup, whereas Billet–Schultes [1] also counts micro-droplets and explicit gas shear, thus predicting higher values. Although

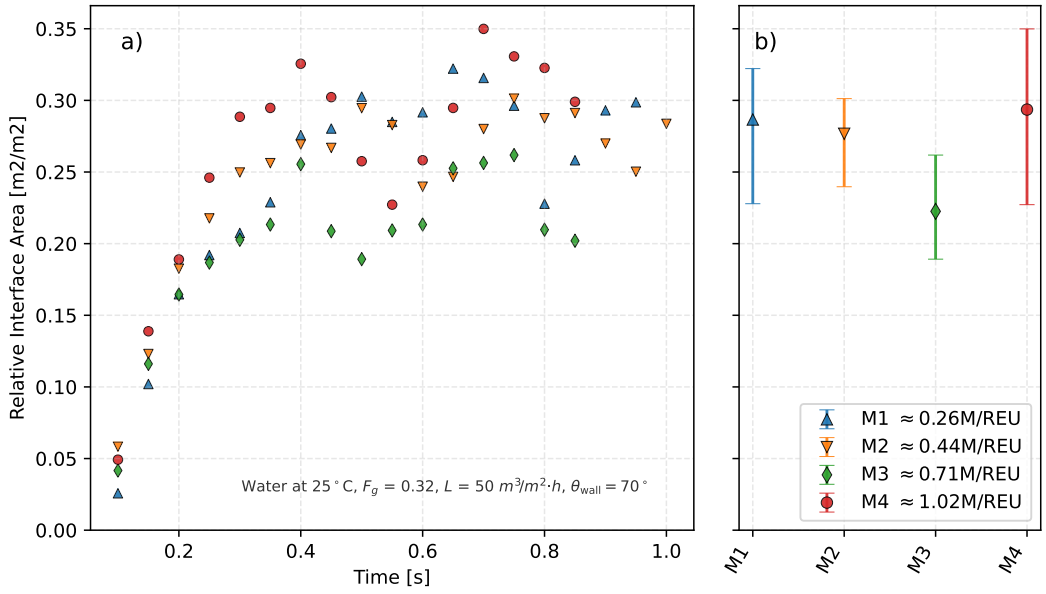


Figure 5.7 Interface area sensitivity analysis with minimum maximum and mean values

Mellapak 500.Y ($500\,\mathrm{m^2\,m^{-3}}$) was used throughout in this study, the Mellapak 250.Y correlation was employed in the Figure 5.8, since it served as a common basis across all three studies, corresponding to a packing type with $250\,\mathrm{m^2\,m^{-3}}$ specific surface area.

The three literature correlations, each derived from distinct experimental databases (as discussed in the Literature Survey section), yield regression exponents that are not directly comparable. Billet links the liquid holdup to both $\mathrm{Re_L}$ and $\mathrm{We_g}$, whereas Spiegel assumes a constant gas influence, and Olujić introduces a damped gas contribution within a channel-based model. Consequently, their predictions diverge as the liquid load increases. Despite their generally similar trends, the Billet–Schultes correlation [27] was adopted in this study, as it explicitly corresponds to a $500\ \mathrm{m^2\,m^{-3}}$ packing configuration, unlike the other models.

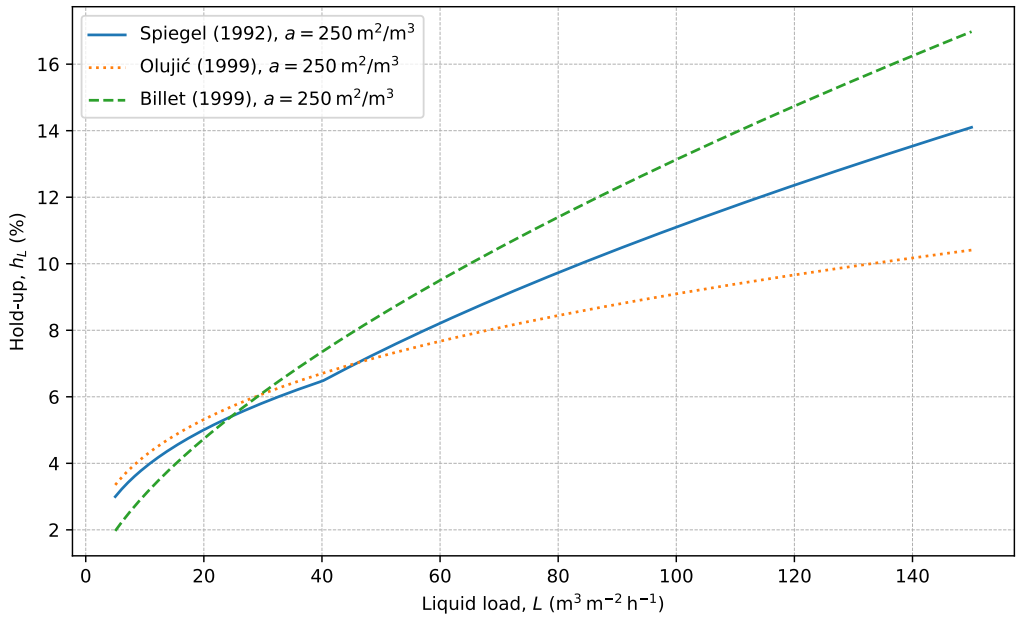


Figure 5.8 Three hold-up correlations compared in the range of 5-150 m3/m2-h liquid loads [2], correlations were computed for the present study.

5.2.3.1 Effect of Liquid Load

Figures 5.9 and 5.10 present holdup versus liquid load using time-averaged values over $t = 0.40$–0.85 s for water at $25°C$ and for $20\ wt\%$ MEA at $36°C$, respectively. For water, the CFD predictions follow the Tsai (Billet–Schultes–based) trend and remain within $\pm 10\%$ of the measured means for $L = 25$–$50\ m^3\,m^{-2}\,h^{-1}$, with a modest under-prediction at higher L that still lies inside the experimental scatter (see right-hand error panels).

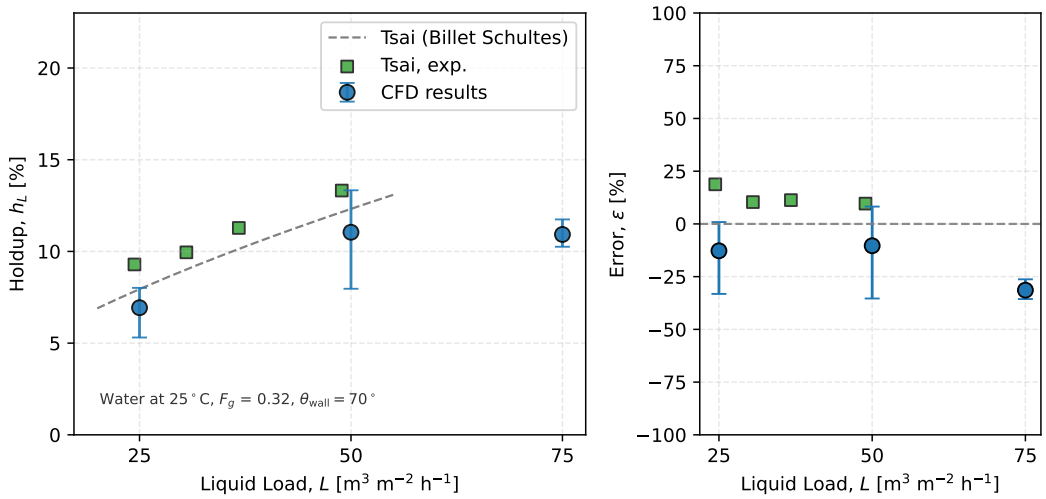


Figure 5.9 Effect of liquid load on holdup compared with correlation by Tsai based on Billet–Schultes [1, 16].

For the MEA system (Fig. 5.10), the CFD simulations reproduce the increasing trend of h with L in a consistent manner, based on time-averaged values over the selected sampling window, showing close agreement with the Billet-Schultes correlation at certain operating points and deviations of up to approximately 10 percent at higher liquid loads.

As elaborated in the Static Contact Angle section, decreasing the static contact angle reduces the observed interfacial angle and holdup; this wettability sensitivity accounts for a significant part of the residual bias. Despite short-time oscillations (occasionally up to $\pm 30\%$), the window-averaged holdup provides a stable and meaningful quantity for validation against correlation-based references in both systems.

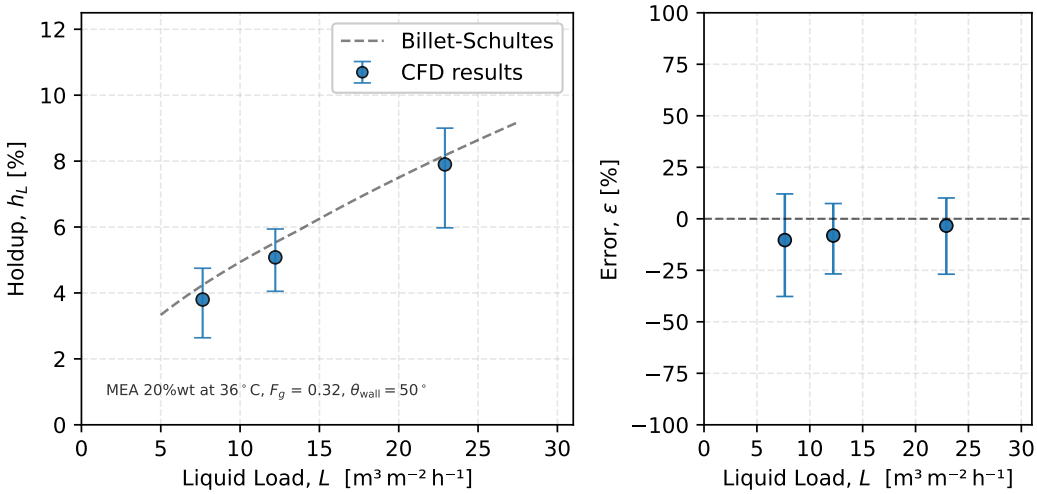


Figure 5.10 Effect of liquid load on holdup compared with correlation by Billet–Schultes for $20\%wt$ MEA at $36°\mathrm{C}$ [1].

5.2.3.2 Effect of Gas Load

Studies such as [2, 16, 27] indicate that liquid holdup is generally insensitive to alteration in gas loads. However, once the gas load surpasses a critical threshold, flooding phenomena may occur (see Literature Review for detailed discussion). As shown in Fig. 5.11, CFD results reproduce this behavior, with time-averaged holdup values remaining within a $\pm 10\%$ error band.

Although the mean holdup h_L percentage remains essentially constant across the studied gas-load interval, the minimum and maximum holdup values of the data grows beyond $F_g = 0.9\ \mathrm{m\,s^{-1}(kg\,m^{-3})^{0.5}}$, consequently, the widening error band is consistent with the onset of wave-induced film fluctuations reported by Billet [27] and the CFD results reported in the attachments such as in the Fig.A.12.

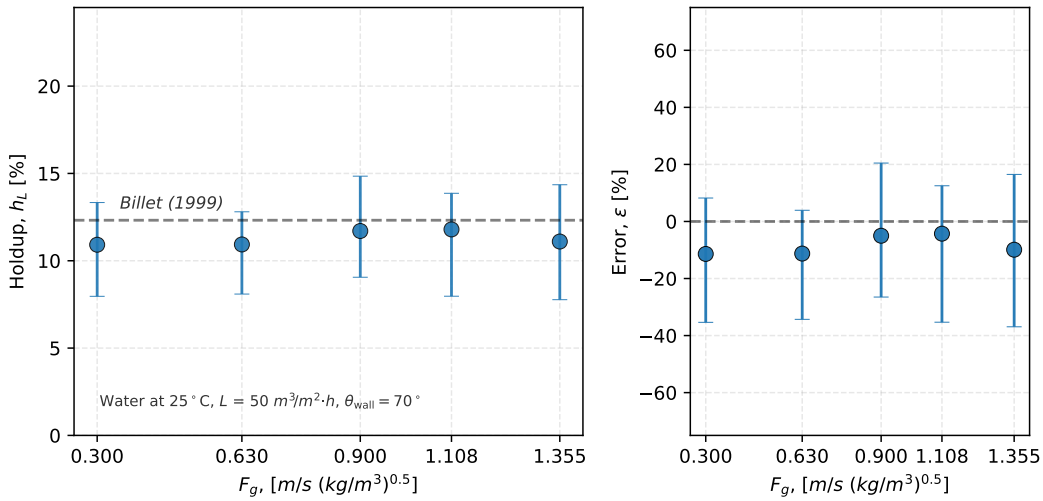


Figure 5.11 Effect of gas load on liquid holdup compared with correlation by Tsai based on Billet–Schultes [1, 16]

5.2.3.3 Effect of Static Contact Angle

The static contact angle governs the initial wetting behavior: lower static contact angles increase film formation and slightly higher holdup, while higher values limit liquid spread on the packing surface. In dynamic conditions, the contact angle increases with the local capillary number, leading to short drying and oscillatory fluctuations in the liquid film. Despite these transients, the time-averaged holdup remains largely unaffected, indicating that dynamic contact-angle effects introduce only minor deviations ($< 5\%$) around the baseline set by the static angle.

CFD results demonstrate the expected behavior: as shown in Fig. 5.12, reducing the wall–liquid contact angle produces an increasing holdup trend within the packing. Simulations at a static contact angle of 70° match the validation curve more closely than those at 45° and 30° for the operating case. Appendix Figs. A.7 and A.8 exhibit irregular, non-physical holdup distributions at the lower angles, whereas Fig. A.5 shows the expected rivulet structures on the packing surface.

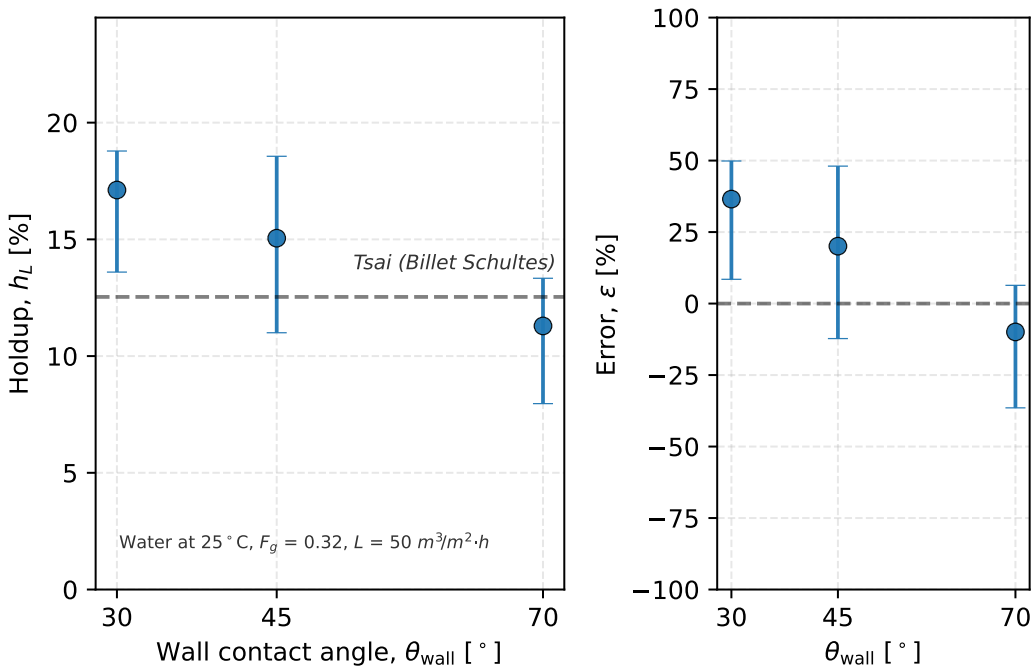


Figure 5.12 Effect of static wall contact angle on liquid holdup compared with correlation by Tsai based on Billet–Schultes [1, 16]

Moreover, the surface patterns on the packing (see in the first section Fig. 1.4 and Fig. 1.3) are specifically designed to reduce the contact angle. Since these small features are not explicitly represented in the CFD mesh, their influence is applied by especially adjusting the static contact angle parameter.

The altered film thickness resulting from contact angle variation has a direct impact on mass-transfer performance. Thicker liquid films increase the interfacial area, which can enhance overall mass-transfer coefficients and reduce the HETP. Ultimately, this shows importance of capturing lower contact-angle behavior in structured packings.

5.2.3.4 Effect of Dynamic Contact Angle

The influence of static and dynamic wall-contact angles on the flow field and on the derived bulk metrics such as liquid holdup and interfacial area was examined from both quantitative and qualitative manner[10, 15, 33]. Snapshots taken at 0.8, 0.9, and 1.0 s are compiled in Figure 5.13:

- Figure 5.13a employs a static contact angle of $\theta_{\text{wall}} = 70°$ without any user-defined function (UDF). Because the ensuing bulk-flow results differed

only marginally from the dynamic cases, this configuration is retained throughout the remainder of the thesis.

- Figure 5.13b represents a dynamic, advancing scenario in which the contact angle is increased to $\theta_{\text{wall}} = 70^\circ + 10^\circ$ via a dedicated UDF, yielding an effective wall angle of roughly 80° and thus accentuating the advancing behaviour.
- Figure 5.13c depicts a fully dynamic model with $\theta_{\text{wall}} = 70^\circ \pm 10^\circ$, enabling simultaneous assessment of both advancing and receding effects.

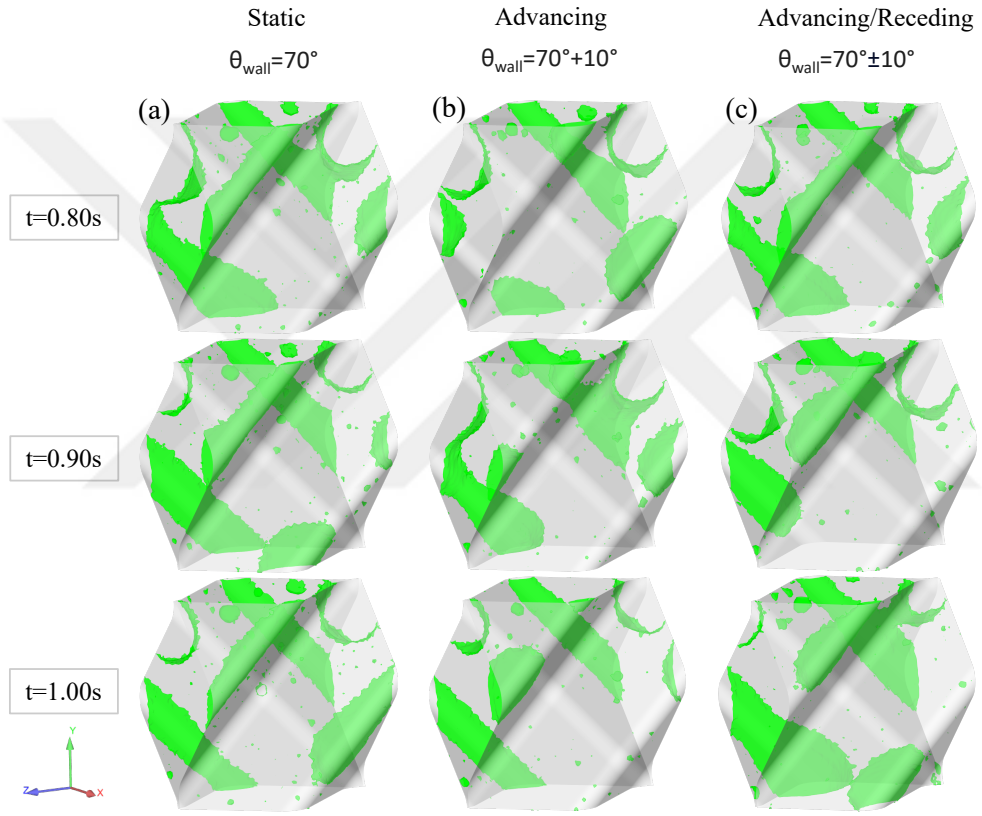


Figure 5.13 Static contact angle and dynamic contact angle comparison between 0.8s-1.0s: iso-surface at $\alpha = 0.5$

Although the DCA model was successfully implemented and verified, the overall impact on key macroscopic parameters such as holdup (Fig. 5.14) and interface area (Fig. 5.15) remained marginal. This suggests that under the studied flow regime, the capillary number remains sufficiently low (Ca < 0.01), demonstrating the dynamic variation of contact angle relatively minor. Consequently, the system behavior is averaged to the near-constant effective contact angle, and DCA exhibits limited influence on bulk flow characteristics.

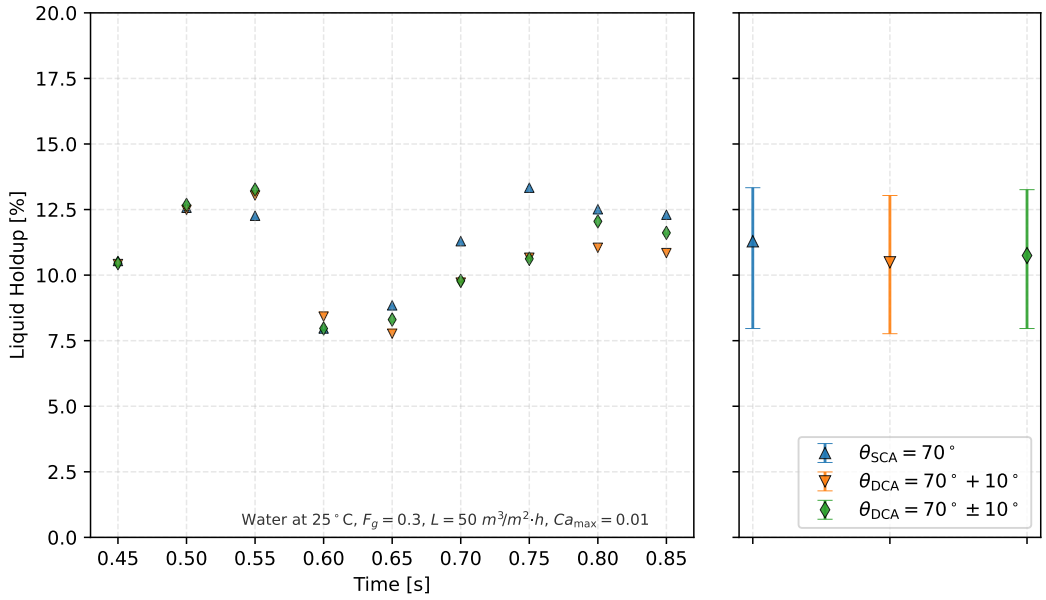


Figure 5.14 Dynamic contact angle and static contact angle comparison for holdup

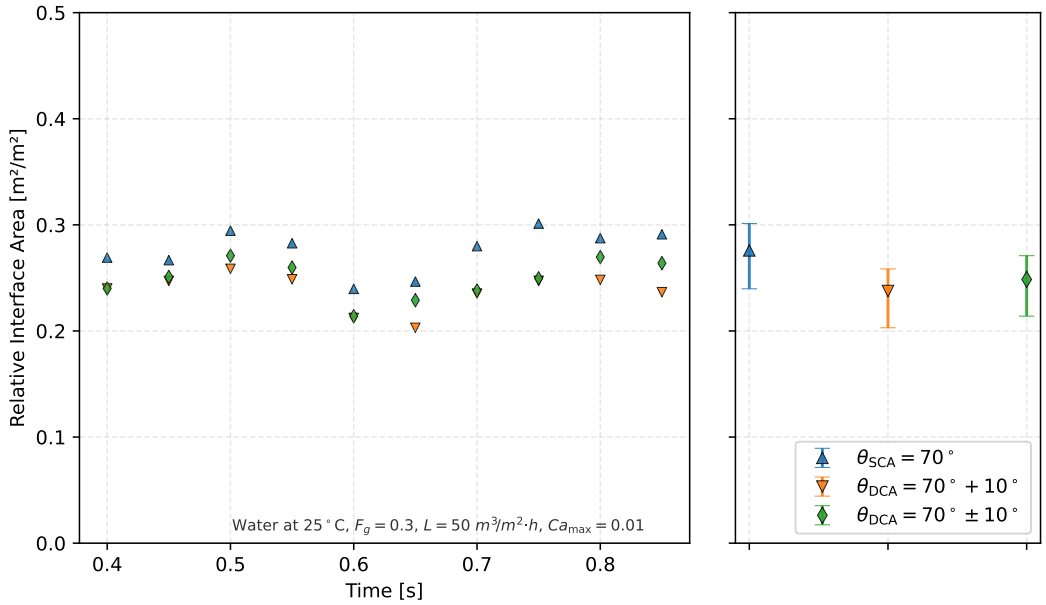


Figure 5.15 Dynamic contact angle and static contact angle comparison for relative interface area

5.2.4 Wet Pressure Drop

In this section, we extend the discussion from dry-gas hydrodynamics to the more computationally demanding wet-gas pressure drop. While dry-gas behavior is well documented in both CFD and experimental studies, detailed parametric CFD analyses of wet pressure drop are still lacking. The following bullet points summarize our approach:

- Dry-gas pressure was discussed with the results in the Single Phase Hydrodynamics section, where the face-to-face spacing of the number of REU's calibrated. In the literature there are many experimental investigations of dry gas pressure that are discussed in detail in the hydrodynamics chapter of the literature survey. However, parametric CFD studies addressing wet pressure drop remain scarce. This is due to the substantial computational effort required, since wet pressure drop analyses are computationally intensive.

- Nonetheless, wet pressure drop is a critical parameter for packed-column performance, since an operating column is never perfectly dry and always involves liquid–gas interactions. As liquid holdup increases, the void space available for gas flow through the structural packing narrows, leading to an increase in pressure drop. In this section, discrete point studies were performed to identify optimal modeling parameters and validate them against existing data.

- For the calculation of wet-gas pressure drop, we adopted a methodology based on the inlet and outlet planes of the REU's. Cells with liquid volume fraction $\alpha = 0$ were treated as pure gas, and the pressure difference between the REU boundaries was computed accordingly.

5.2.4.1 Effect of Liquid Load

In most published correlations [16, 30], the effect of varying liquid load on gas-phase pressure drop is not incorporated into the governing equations (see eqn. 2.13. However, as shown in Fig. 5.16, despite this common situation, increasing the liquid load from $L = 25\,\mathrm{m^3/m^2\,h}$ to $L = 50\,\mathrm{m^3/m^2\,h}$ results in a nominal pressure-drop increase of approximately 17%. Moreover, a further rise from $L = 50$ to $75\,\mathrm{m^3/m^2\,h}$ produces an additional, statistically significant increase of about 18%.

5.2.4.2 Effect of Gas Load

Although our CFD predictions show a certain percentage deviation from Tsai's experimental measurements and correlation, they reproduce the same exponential trend of increasing pressure drop with rising gas velocity (Fig. 5.17). It should be denoted that Tsai's final data point reveals the onset of flooding at very high gas loads.

Mesh-dependence analysis indicates that finer grids (M3 and M4) produce pressure-drop values for $F_g = 0.32$ at $L = 50\,\mathrm{m^3/m^2{\cdot}h}$ that are 30–40% lower—and

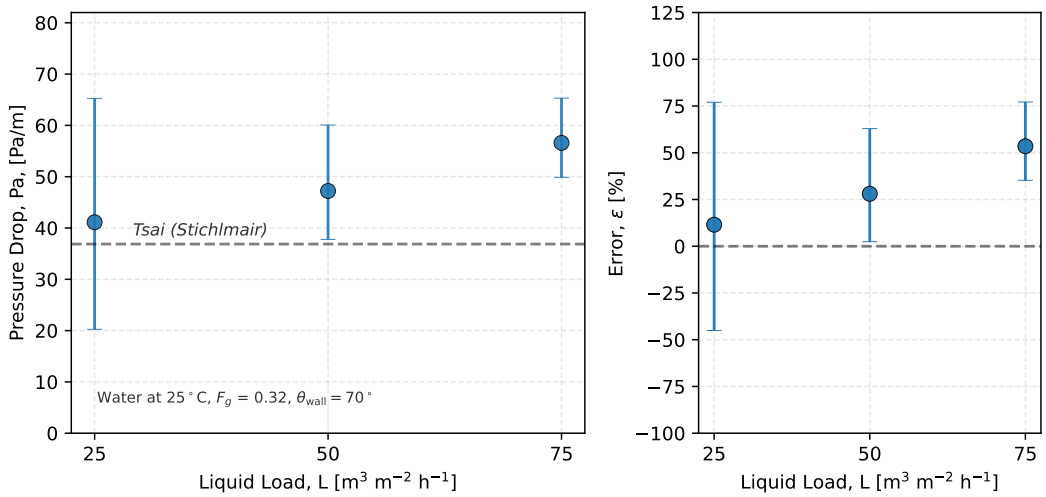


Figure 5.16 Effect of liquid load on pressure drop compared with correlation by Tsai based on Stichlmair [16, 30]

therefore in closer agreement with the correlation—than the coarser M2 mesh. This finding underscores the importance of using high-resolution meshes (>0.7 million cells per REU) specifically in wet-pressure-drop simulations.

The span between minimum and maximum pressure-drop results under a single-REU setup displays considerable scatter, as shown by the error bars in Fig. 5.17. While the single-phase hydrodynamics study confirmed REU independence, the wet-pressure-drop analysis remains highly sensitive to REU choice. Thus, when liquid holdup decreases in a single REU's boundary, pressure drop oscillates exponentially. Adopting multiple REU's would dampen these oscillations and yield more stable predictions.

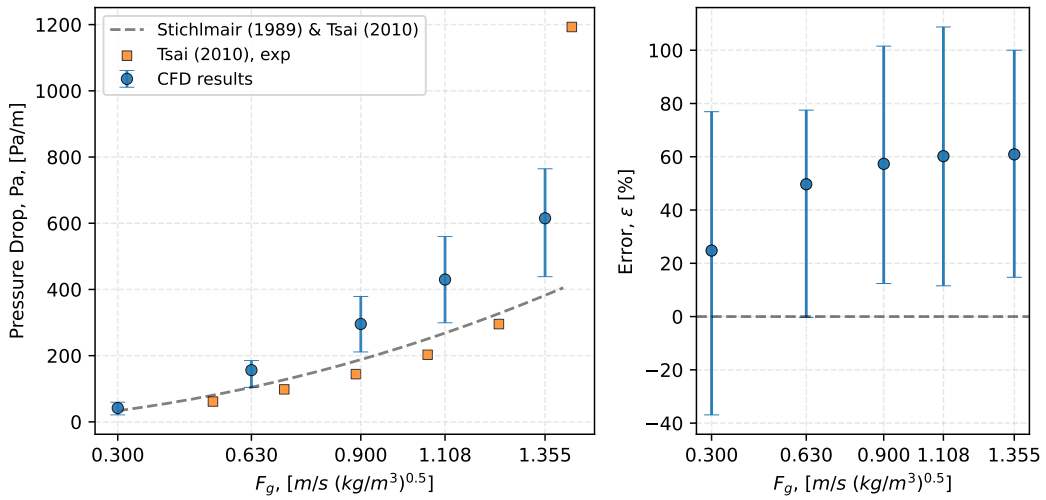


Figure 5.17 Effect of gas load on pressure drop compared with correlation by Tsai based on Stichlmair [16, 30]

5.2.4.3 Effect of Contact Angle

The static wall contact angle was identified as another critical parameter influencing wet pressure drop. In CFD simulations at 25 °C with water, contact angles of 30°, 45°, and 70° were tested, and the 70° case yielded the closest agreement with expected pressure-drop behavior. At lower angles (45° in Fig. A.7 and 30° in Fig. A.8), rivulet formation is inhibited, the liquid film is overly dispersed, and realistic pressure drops could not develop. These observations are demonstrated in Fig. 5.18. Since the contact angles of 30° and 45° are higher than 100% error, therefore they are not shown in the error bar.

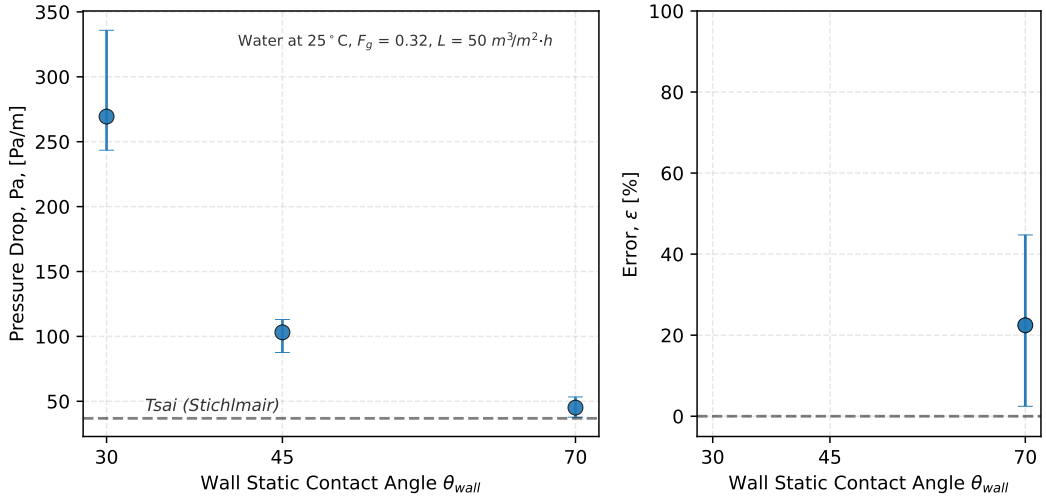


Figure 5.18 Effect of gas load on pressure drop compared with correlation by Tsai based on Stichlmair [16, 30]

5.2.5 Interface Area

5.2.5.1 Effect of Liquid Load

Figure 5.19 shows our CFD-based relative interface areas with the frequently cited correlations in the literature. In this Figure, The left panel plots the dimensionless interface area $a_{\text{int}}/a_{\text{p}}$ as a function of liquid load L, while the right panel reports the corresponding percentage error with respect to the empirical fit of Schug's measurements.

All data sets exhibit the expected a rise in interfacial area as L increases, confirming that a higher liquid throughput promotes film thickening and rivulet formation.

The apparent spread in the fractional area $\alpha = a_{\text{eff}}/a_p$ originates from four fundamental differences in experimental strategy and model construction

Since Billet-Schultes [27] extracted a_{eff} indirectly by regressing overall mass-transfer data from $\sim$2600 column runs. The resulting correlation, embeds both hydraulic and physico-chemical effects, so any systematic bias in k_L is automatically absorbed into the correlation. Note that Billet's data is dominated by low-tension distillation mixtures (such as hydrocarbons) therefore the direct comparison might alter than the real comparison. Tsai [64] measured a_{eff} via CO_2/NaOH absorption, then fitted a dimensionless power law that collapses liquid Weber and Froude numbers. The approach decouples film properties from mass-transfer coefficients, but packs all geometric complexity into a single length scale, so fine textures or partial wetting might not be captured. Moreover, Tsai employed mid-high surface tension solvents (30–72 mN m^{-1}) therefore their correlation might not align with very low tension solvents. Schug [18] employed high resolution X-ray CT to count wetted pixels and calculate interface area accordingly. Since Schug employed Mellapak 500.Y. in their study, therefore implementing experimental data to this study is valuable. The X-ray CT technique reveals dead zones and rivulet formation bridges driving lower than Tsai's correlation. Further, Schug used Isopropanol and Water in their experiments that aligns with this study and capture interface area well. Ultimately, compared studies answer different questions: Billet-Schultes [27] delivers a correlation to be tuned to estimate overall column efficiency; Tsai supplies a physics-clean scaling law for aqueous absorbers; Schug uncovers the true interfacial area inside the structural packing. The CFD results discussed here is naturally aligning with closest Billet and Schug. The study overshoots Tsai which might be high Weber numbers that push the correlation beyond its calibration. Consequently, the study which seemed consistent with the methodological approach disccussed above.

In CFD results three iso-surface thresholds were demonstrated to parameterize gas–liquid interface, $\alpha = 0.5$ (blue circles), 0.3 (orange squares) and 0.1 (green triangles).

- The iso-surface cut-off $\alpha = 0.1$ remains close to $\pm 10\,\%$ of Schug's fit over the entire L range. Although the fit and our study remained close, the physical realism might not be captured well due to exaggerated interface demonstrated in the Fig. A.14 and Fig. A.13.
- Increasing the threshold progressively incorporates increasing rivulet flows, inflating the calculated area. The iso-surface cut-off $\alpha = 0.3$ remained close the the iso-surface cut-off $\alpha = 0.5$, therefore both of the cut-offs close agreement with Billet-Schultes [27] correlation.

As a result, selecting an interface criterion is therefore substantial; iso-surface $\alpha = 0.5$ shows a practical balance in physical realism, whereas lower iso-surface area should be further considered for studies explicitly targeting dispersed droplets or entrainment.

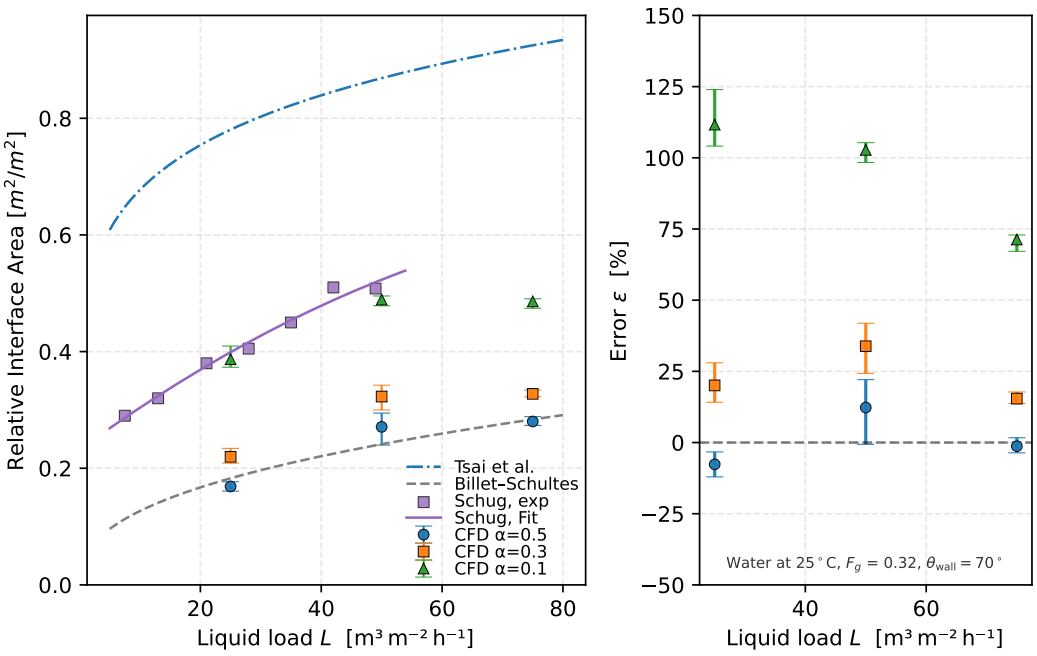


Figure 5.19 Effect of liquid load on interface area compared with correlations by Tsai [64], Billet-Schultes [27],Schug [18] depending on different iso-surfaces

5.2.5.2 Effect of Gas Load

In Fig. 5.20, in-line and expected with the literature, no statistically significant change in the relative interface area is observed over the investigated gas-load range ($F_g = 0.30$–$1.36\ \mathrm{m\,s^{-1}(kg\,m^{-3})^{0.5}}$) at a fixed liquid rate of $L = 50\ \mathrm{m^3\,m^{-2}\,h^{-1}}$. The CFD-predicted values cluster close around the Billet–Schultes correlation [27] evaluated for the given operating point. Assuming a wall static contact angle of $\theta_{\mathrm{wall}} = 70°$ for water at 25 °C yields the smallest deviation (within $\pm 10\%$) from the Billet–Schultes benchmark, validating this choice for subsequent simulations. Furthermore, although the Single-REU model adapted, low oscillating behavior in error bars ($< 20\%$) across all F_g levels demonstrate that the Single-REU model could be a good candidate for especially interfacial area determination in CFD studies.

5.2.5.3 Effect of Contact Angle

Diminishing θ_{wall} to 30° increases the predicted interface area by roughly 2.4 times, bringing it closer to the capillary-driven relationship reported by [64], however,

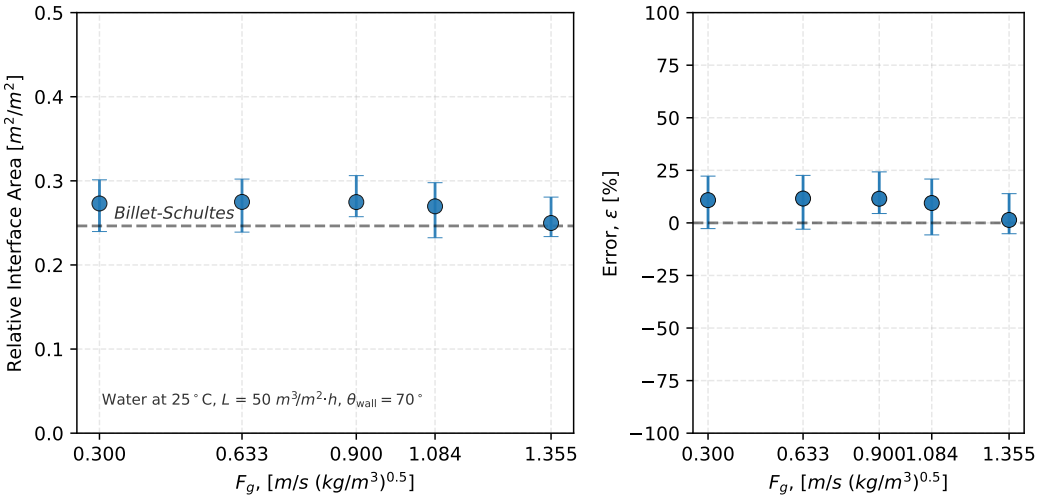


Figure 5.20 Effect of gas load on interface area compared with Billet-Schultes [27]

this scenario simultaneously produces unrealistically high holdup and high pressure drop for water in Mellapak 500.Y. An intermediate angle of $45°$ offers a more balanced outcome but still overpredicts interface area (approximately $0.40\ \mathrm{m^2\,m^{-2}}$) and can exaggerate rivulet formation. The reference case of $\theta_{\mathrm{wall}} = 70°$ aligns best with Billet–Schultes [27], reinforcing it as the most realistic setting for water at $25\ ^{\circ}\mathrm{C}$ on this packing. Moreover, a $\pm 5°$ perturbation around the $70°$ baseline alters the interface-area prediction by less than 5%, indicating that modest uncertainties on model accuracy especially in interfacial area.

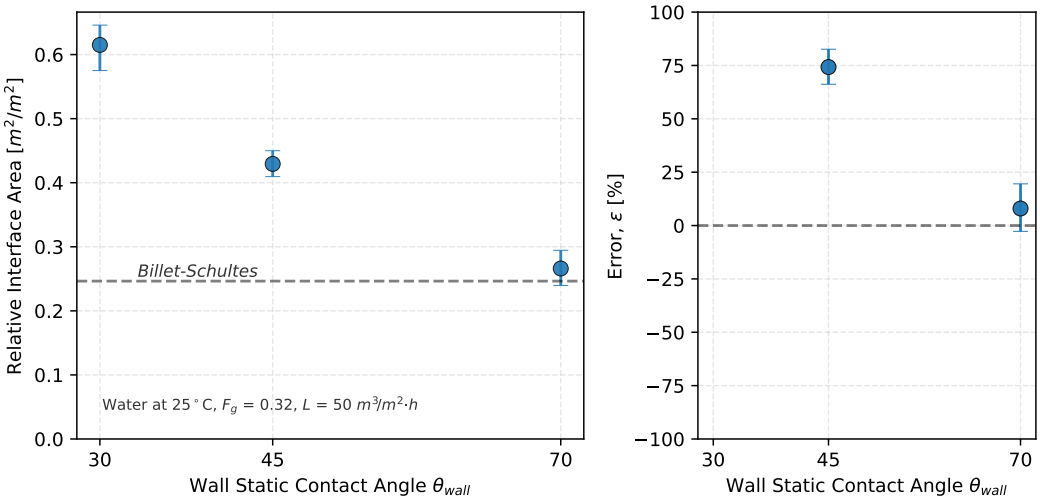


Figure 5.21 Effect of wall static contact angle on interface area compared with Billet-Schultes [27]

5.3 Two-Phase Reactive CO_2-MEA Absorption

In this section, the results of reactive CO_2–MEA absorption are examined. The chemical reactions and corresponding kinetic rates applied during the simulations are presented in Section 3.3.3, while the thermophysical property models are described in Section 4.4. The developed mass transfer methodology was implemented into ANSYS Fluent through a user-defined function (UDF), as detailed in Section 4.5.1.

A mesh sensitivity analysis was performed using the $K_G a_e$ metric for the case with the highest liquid loading, while keeping some mesh parameters constant. The mesh resolution was selected to balance accuracy and computational cost optimally. Furthermore, operational parameters were calculated from literature sources in order to compare with the appropriate literature source. The sensitivity of selected parameters, such as the wall contact angle, was also investigated. The model results compared with literature $K_G a_e$ values.

Moreover, the interfacial area was reported separately, allowing direct evaluation of the overall mass-transfer coefficient $K_G a_e$ under the assumption that $a_e = a_{\text{int}}$. Finally, the obtained a_{int} and a_e values were compared with literature correlations through tabulated results, highlighting the order of magnitude and consistency of the present findings.

5.3.1 Mesh Sensitivity Analysis

In the Figure 5.22, mesh sensitivity summary given for $K_g a_e$. All meshes used identical numerics in Fluent Meshing: prism-layer growth factor $= 1.1$ with layers grown only on REU wall surfaces, global Courant number set to ≈ 0.5, and simulation time has been conducted to reach $1.5\,\text{s}$ simulation time. Grid size and near-wall resolution increase from M1 to M5. The number of cells contained in each mesh are: M1 ≈ 0.19M, M2 ≈ 0.51M, M3 ≈ 0.76M, M4 ≈ 1.12M, M5 ≈ 2.22M cells. Prism-layer settings vary as:

- M1–M2: 7 layers (first-layer AR $= 2$)
- M3–M4: 9 layers (first-layer AR $= 3$)
- M5: 12 layers (first-layer AR $= 3$)

It was observed that the convergence time in the simulations increased particularly for cases where cells contained nonzero volume fractions of the liquid phase

(VOF > 0). This occurs because additional iterations are required to resolve the interfacial dynamics within these cells. Consequently, cases with higher liquid loads exhibited larger numbers of inner iterations per time step. Moreover, increasing the superficial gas velocity also led to longer convergence times. As shown in the CFL condition (see Eq. 4.18), when the Courant number is adaptively maintained at a constant value, a higher velocity u necessitates a smaller time step Δt. Additionally, refinement of the computational mesh decreases the spatial step Δx, which in turn further reduces the allowable time step size and thus affects the overall convergence rate. Approximate wall-clock times were given in the Fig. 5.22, which is conducted

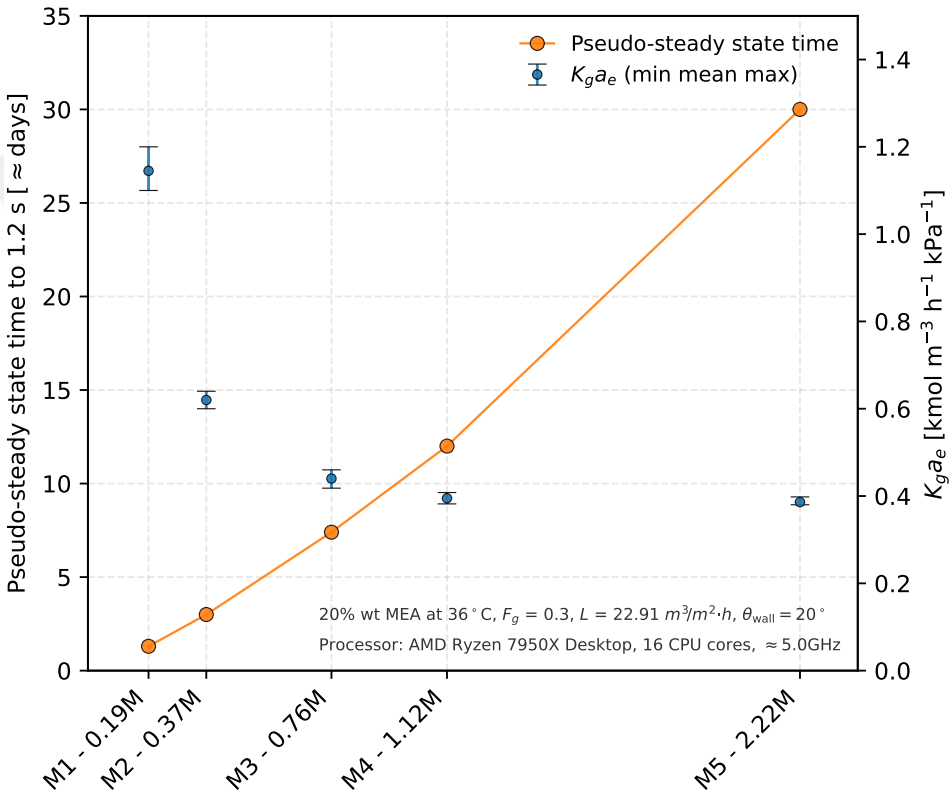


Figure 5.22 Effect of number of cells to the mass transfer of REU

with Ryzen 7950X - 16 physical core.

Considering all factors discussed above, an optimal mesh configuration was selected to achieve a balance between computational accuracy and convergence efficiency. Predicted $K_g a_e$ results showed that diminishing changes with refinement, suggesting a near-plateau by M3, while M4 and M5 mesh cases yields only marginal improvement at substantially higher cost. Thus, mesh M3 was adopted as the reference grid because it demonstrates the better balance between computational cost and accuracy, yielding near-converged predictions while requiring markedly less wall-clock time than M4 ($\sim$13 days) and M5 ($\sim$30 days).

Figure 5.22 also indicates a systematic grid effect on $K_g a_e$. The coarser meshes (M1 and M2) predict substantially larger $K_g a_e$ values, whereas the change from M3 to M5 is comparatively small. This behavior is consistent with VOF based interface capturing, where insufficient spatial resolution can smear the interface and increase numerical diffusion, which artificially enhances the apparent interfacial transport. Accordingly, M1 and M2 should be treated as overpredictive for reactive absorption, while M3 provides a practical near converged estimate at a feasible computational cost.

Across the five mesh levels (M1–M5), the time traces over $0 \leq t \leq 1$ s show that the relative interfacial area a_{int} as shown in Fig.5.23 follows a consistent transient toward a quasi-steady plateau. The outlet CO_2 mole fraction remains bounded between ≈ 0.0191 and 0.0196. M1-M2 meshes demonstrated poor performance on grid-sensitivty analysis according to the parameters investigated. A broad range of cells swept (~ 0.2 to 2.22 million cells) confirms mesh-independent trends for all reported quantities.

A small but systematic phase lag is observed between the hydrodynamic indicator and the outlet based mass transfer metrics. The relative interfacial area a_{int} reaches its plateau earlier (typically around $t \approx 0.50 - 0.60\,\text{s}$), whereas $K_g a_e$ and $y_{\text{CO}_2,\text{out}}$ approach a quasi steady level later (after around $t \approx 0.7\,\text{s}$). This delay is physically expected because a_{int} is a local hydrodynamic quantity, while $K_g a_e$ and especially $y_{\text{CO}_2,\text{out}}$ are evaluated at the packing outlet and therefore include a convective transport time for the CO_2 fed from the inlet to reach the outlet plane. A simple time of flight estimate gives

$$t \approx \frac{H}{u_G} = \frac{0.0142\,\text{m}}{0.30\,\text{m}\,\text{s}^{-1}} \approx 4.7 \times 10^{-2}\,\text{s}, \tag{5.1}$$

indicating that outlet based quantities should respond with a finite lag even after a_{int} has stabilized. Additional numerical and physical factors (species transport, interfacial renewal, and transient development) can further broaden this response, hence the later stabilization of $K_g a_e$ and $y_{\text{CO}_2,\text{out}}$ is consistent with the physical fluid behavior.

A consistent ranking is observed across the three reported quantities. Meshes that yield larger a_{int} also yield larger $K_g a_e$ and a lower $y_{\text{CO}_2,\text{out}}$, indicating higher predicted absorption. Along with the consistency discussed above, across a_{int}, $K_g a_e$, and $y_{\text{CO}_2,\text{out}}$ provides an internal physical cross check of the coupled hydrodynamics and mass transfer response to grid refinement.

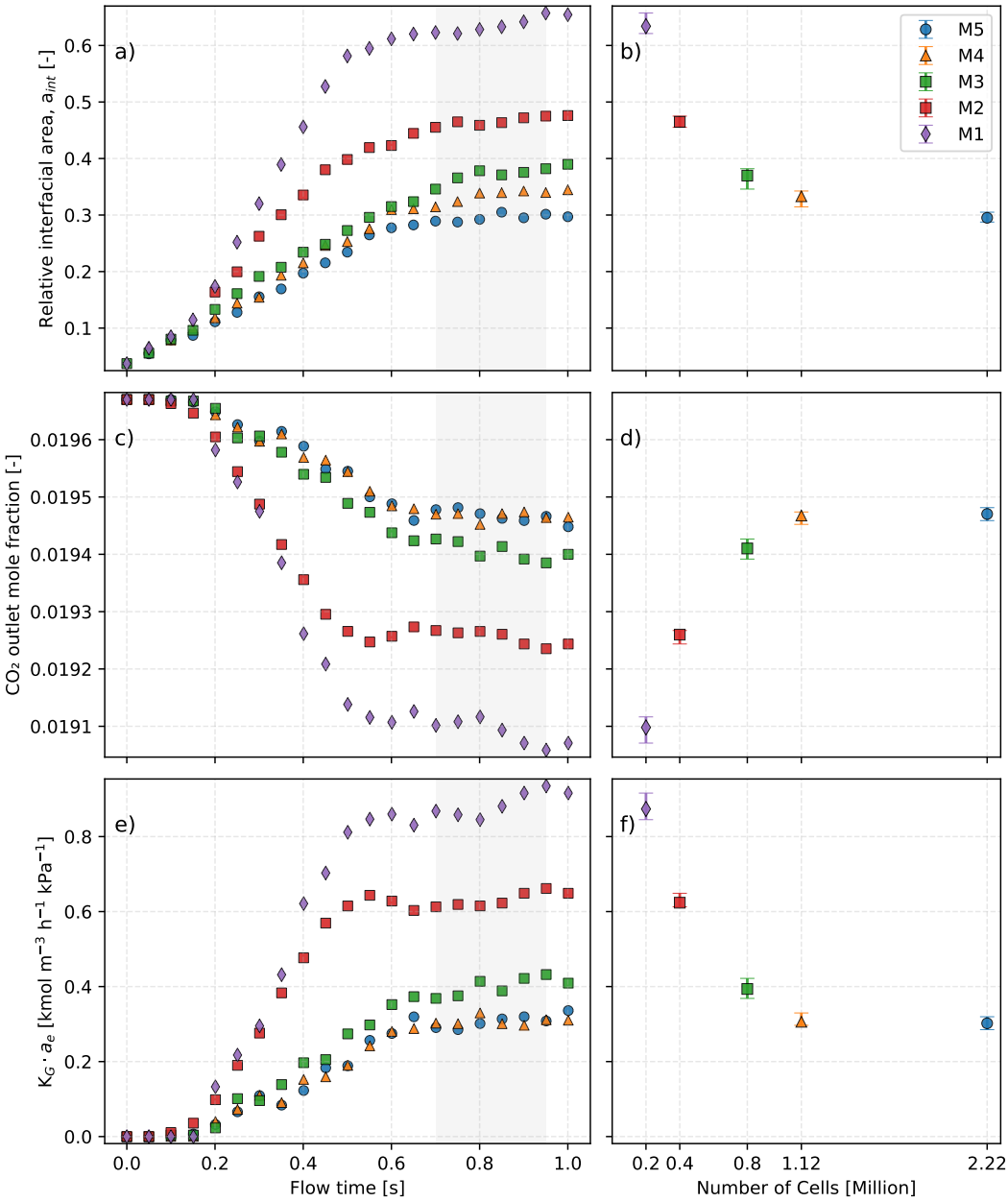


Figure 5.23 Reactive absorption sensitivity analysis comparing $K_g a_e$ with a_{int} and the CO_2 outlet mole fraction over a $1.0\,\mathrm{s}$ interval. Time-averaged values (grayed area) were computed over the pseudosteady-state window from 0.70 to $0.95\,\mathrm{s}$. Operating conditions were $L = 22.91\,\mathrm{m^3\,m^{-2}\,h^{-1}}$ and $F_g = 0.3\,\mathrm{m\,s^{-1}}$, using $20\,\mathrm{wt\%}$ MEA at $36\,^{\circ}\mathrm{C}$.

5.3.2 Transient Development of Reactive Absorption

Figure 5.24 demonstrates three consecutive snapshots ($t = 0.80$, 0.90 and 1.00 s) of the two–phase flow field inside single REU Mellapak 500.Y model. The gray surface represents the surface of the sheet, the blue map the instantaneous liquid volume fraction (α_L, iso-surface at 0.5), and the brown to yellow streamlines gas phase CO_2 (15% mole/mole)-Air mixture. Streamlines are colored by the local CO_2 mole fraction, as indicated by the color bar.

Throughout the three frames the liquid forms a spatially continuous, film flow (periodical on the z-axis) interrupted by thicker rivulets and droplet residues due to the surface tension and static wall contact angle. In the figure, quasi–steady state has been reached since there is reduced oscillation behavior in: holdup, interface area and CO_2 outlet mole fraction. This observation is consistent with the earlier holdup behavior reported in the section where the two phase hydrodynamic results discussed.

The streamlines originate at the column bottom (high y_{CO_2}, brown) and rise upwards while gradually turning yellow–white, demonstrating CO_2 absorption into the liquid film. The color transition is smooth and monotonic near the liquid film surface, implying the a realistic behavior in absorption. Moreover, near the sheet face to face region (optimum distance for single REU modeling is discussed in dry pressure drop section) showing how the corrugation promotes lateral mixing and renews between bulk and surface interface.

The figure corroborates three key mechanistic insights:

- A largely wetted sheet surface with localized rivulet thickening and droplet remnants.
- Progressive CO_2 depletion along gas flow paths in proximity to the liquid film.
- Lateral redistribution of gas streamlines induced by the corrugated channel geometry.
- The face-to-face sheet alignment promotes gas mixing and enhances turbulence, improving phase interaction.

These observations strengthen the validity of the CFD model for gas absorption along with discussed holdup and interface area.

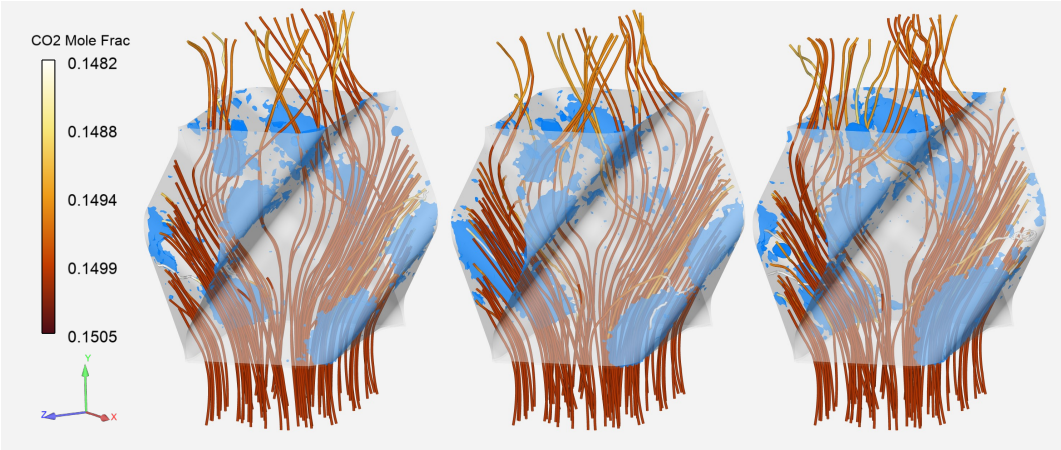


Figure 5.24 Transient reactive absorption for single REU: Streamlines, liquid volume fraction ($\alpha_L = 0.5$) and CO_2 absorption for 0.8, 0.9 and 1.0s (MEA ≈20% wt. at 36°C, $\theta_{wall} = 50°$, $L = 23\ m^3 m^{-2} h$, $F_g = 1.3, m/s\ (kg/m^3)^{0.5}$)

5.3.3 Effective and Interfacial Area

The CFD-predicted effective interfacial area (normalized) increases monotonically with liquid load L over $3.82 - 22.91\ \mathrm{m^3\,m^{-2}\,h^{-1}}$, and falls within the envelope delimited by correlations (Billet–Schultes, Tsai, Bravo–Rocha–Fair, and Brito). Quantitatively, the CFD curve tracks closest to Billet–Schultes at low–to–moderate L, whereas Tsai tends to anticipate higher wetting (larger relative areas) across the range; Bravo–Rocha–Fair and Brito bound the lower side of the envelope at portions of the domain. Overall, the CFD trend corroborates literature expectations—area growth with increasing L and no anomalous departures—supporting the physical plausibility of the simulated film hydrodynamics for MEA ≈ 20 wt% at 36°C.

Relative effective interfacial area (a_e/a_0) versus liquid load L for MEA ≈ 20 wt% at 36°C. Literature correlations [27, 29, 35, 64] are compared against CFD-derived a_{int}; the CFD points fall between the Billet–Schultes and Brito trends over given operating liquid loads.

The CFD results in Figure 5.25 show a monotonic increase of the relative interfacial area with liquid load L, with a gradually decreasing slope at higher L. This concave trend is consistent with progressive wetting of additional surface at low L, followed by an approach toward a more saturated wetting state where further increases in L provide diminishing gains in newly wetted area.

Importantly, the quantity reported here as a_{int} is obtained from a VOF based interface identification and therefore depends on the adopted interface definition. When the interface is extracted using an $\alpha_L = 0.5$ iso surface, the resulting area

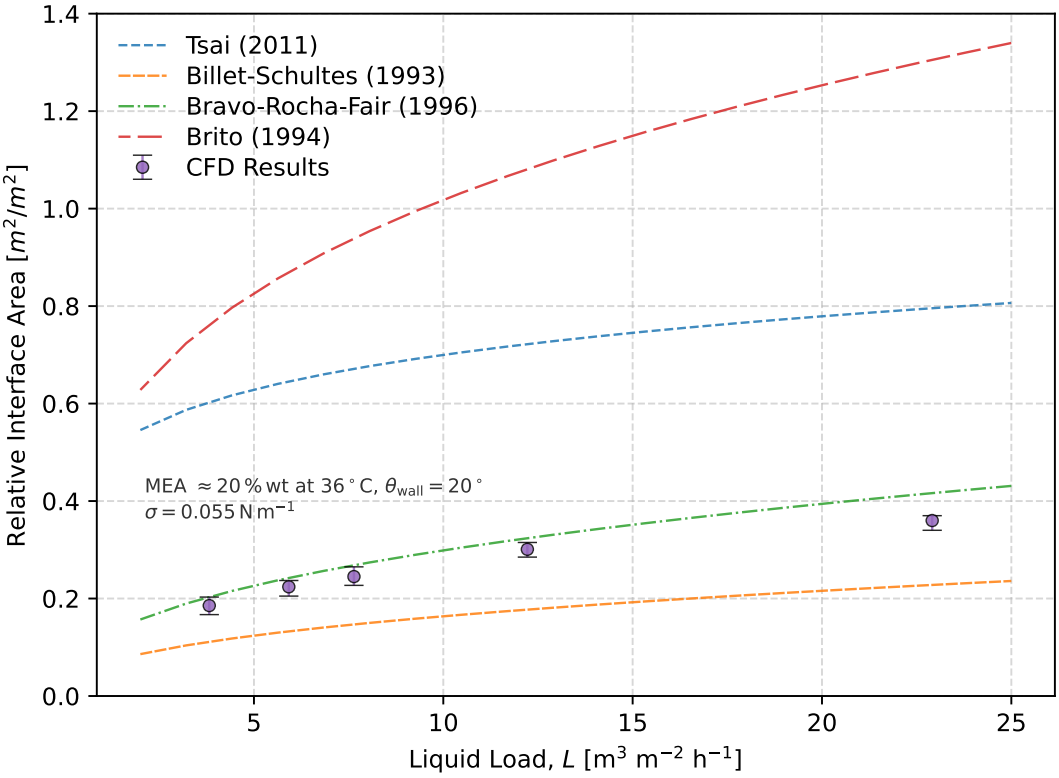


Figure 5.25 Comparison for calculated a_e values [27, 29, 35, 64] and the CFD Results a_{int} across liquid load of $L = 3.82 - 22.91\ m^3 m^{-2} h$

tends to be more geometric and may fall closer to correlations that predict lower effective wetting. In contrast, using a broader phase fraction cut, $\alpha_{\min} < \alpha_L < \alpha_{\max}$ with $\alpha_{\min} = 0.01$ and $\alpha_{\max} = 0.99$, includes a wider interfacial region and can shift the reported area toward higher values. This shift is further discussed in the previous Section 5.2.5 and demonstrated the sensitivity in the Figure 5.19. Therefore, in the present work a_{int} should be interpreted as an effective proxy linked to the numerical interface representation rather than a strict equivalent of the correlation based effective area a_e. Consequently, the comparison against literature correlations is used primarily to assess trend consistency and order of magnitude, rather than to assert a one to one equality $a_{\text{int}} = a_e$.

5.3.4 Overall Mass Transfer Coefficient

Figure 5.26 shows that our mesh was tailored to resolve the thin-film regime at moderate to high liquid loads (discussed in the hydrodynamics section), leading to excellent agreement with the experimental trend for the operation.

The comparison in Figure 5.26 indicates a consistent, but moderate, negative deviation of the CFD-predicted $K_g a_e$ from the experimental measurements of

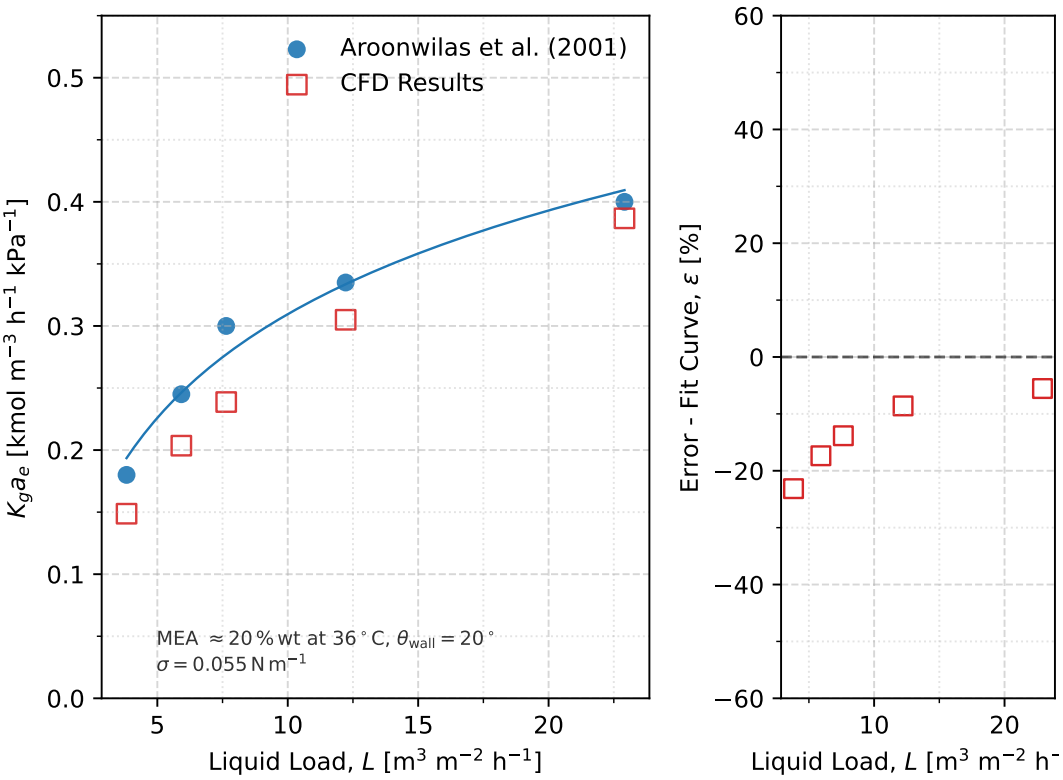


Figure 5.26 Comparison of calculated $K_g a_e$ values [kmol m^{-3} h^{-1} kPa^{-1}] with experimental data from Aroonwilas [19]

Aroonwilas et al. [19]. The magnitude of this deviation is larger at the low-L end of the investigated range and becomes progressively smaller as L increases.

Such load-dependent bias is physically plausible because, under low liquid loads, interfacial coverage is more likely to be spatially heterogeneous and intermittently renewed, and the resulting mass-transfer response can be sensitive to:

- partial-wetting behavior,
- thin-film thickness distributions, and
- local interfacial renewal mechanisms.

In the present framework, these effects are represented through an effective contact-angle specification and a finite interface resolution inherent to the VOF formulation, which may not fully resolve the smallest-scale interfacial features governing transport at low L. Nevertheless, the CFD results reproduce the experimentally observed monotonic increase of $K_g a_e$ with increasing L and remain within the correct order of magnitude over the full operating window, supporting the predictive consistency of the implemented reactive absorption methodology.

A further point is that the near-wall mesh requirement can depend on the liquid load. In VOF-based reactive absorption, the controlling gradients are concentrated close to the wall and around the gas–liquid interface, so a very fine local resolution may be needed. This means that a single mesh design may not be equally suitable for all operating conditions. At low liquid loads, wetting can be patchy and the liquid may appear as thin films or rivulets, so a finer mesh directly at the wall and around the interface is often required to represent the local wetting pattern. At higher liquid loads, the liquid film becomes thicker and more continuous, and important gradients can extend farther from the wall, so additional refinement slightly away from the wall may become more effective. Overall, the observed load-dependent deviation is consistent with the idea that mesh requirements are not independent of L, and that a load-aware meshing strategy can improve consistency across the operating range.

Additional modeling simplifications may also contribute to the observed underprediction. First, constant thermophysical properties were applied along the packing height. In reality, temperature and composition can vary due to absorption and reaction, which may change viscosity, diffusivity, Henry's constant, and thus the effective mass-transfer rates. Neglecting these axial variations can therefore introduce a bias in $K_g a_e$, particularly when the experimental system experiences measurable property changes along the column. Second, the present simulations were performed on a single REU rather than a full-column geometry. While the REU approach is efficient and captures local sheet-scale hydrodynamics, it cannot fully reproduce column-scale effects such as inlet maldistribution, large-scale flow reorganization, and axial development of the gas–liquid contact. These effects may increase the effective interfacial renewal in experiments and can lead to higher measured $K_g a_e$ compared to an idealized periodic REU representation.

As discussed in the literature, perforations can promote additional wetting and rivulet formation on the sheet surface, therefore increasing the available interfacial area and enhancing surface renewal. Bertling [32] reported that such features can measurably increase wetting and generate additional film structures and surface area. Since this mechanism was neglected here, a reduction in the predicted $K_g a_e$ relative to experiments is expected.

Finally, additional uncertainty may originate from the way the experimental $K_g a_e$ values are obtained from Aroonwilas et al. [19]. These values are typically back-calculated from measured inlet–outlet compositions using auxiliary assumptions and estimated inputs. Any uncertainty in the reported operating conditions or in the supporting correlations used during the back-calculation propagates directly into the inferred $K_g a_e$. Moreover, because parts of the original

data set are not fully specified in the open literature, some of the inputs required to reproduce the experiments had to be approximated in the present work as discussed in the Appendix Section A.5.2. Such approximations can lead to a residual mismatch even if the CFD model captures the correct trends, and they should be considered when interpreting the remaining deviation between CFD predictions and the experimental reference.

6
CONCLUSION

This thesis developed and validated a structure-resolved CFD framework for a REU of Sulzer Mellapak 500.Y, directly linking packing geometry to the underlying hydrodynamics and reactive mass transfer in a physics-based manner.

Key findings can be concluded:

- The CFD simulations were able to reproduce the main hydrodynamic characteristics of Mellapak 500Y. Film flow, liquid holdup, and wetting patterns followed the expected behavior, while pressure drop predictions turned out to be strongly dependent on mesh sensitivity.
- Transient VOF simulations captured liquid holdup, wet pressure drop, and interfacial area with consistent dependencies on L, F_g, and wall contact angle. Using a dynamic contact-angle were not measurably affected h_L and a_{int}. Thus, static wall contact angle adopted agreed with the literature studies.
- The coupled mass transfer and reaction within VOF setup reproduced the expected trends of $K_G a_e$ versus L and solvent loading for CO_2–MEA, yielding a good consistency with experimental baselines and demonstrating that interface-resolved CFD can cover transport phenomena performance metrics.

The key original contributions of this thesis can be summarized as follows:

- A systematic optimization of the face-to-face sheet spacing was performed for the single-phase flow domain, which had not been previously addressed in the literature for Mellapak-type packings.
- The wet pressure drop and associated hydrodynamics of two-phase flow were investigated for the first time within this geometry, providing a direct CFD-based linkage between gas–liquid distribution and pressure losses.

- A mechanistic, interface-resolved CO_2 rigorous mass transfer model was implemented within the VOF framework and applied to Mellapak 500.Y structured packing representing the first rigorous CFD study of reactive absorption in such REU configuration.

The main limitations of the present study can be summarized as follows:

- Although the two-phase domain computed in single-REU approach, the transient solution still demands substantial computational resources.
- The simplified sheet geometry neglects embossing and perforation features, which suppress the development of rivulets or surface waves that would normally enhance interfacial area in real packings. Consequently, both local hydrodynamics and mass-transfer surface activation may be underestimated in this idealized REU configuration.
- Due to the grid resolution constraints, the internal liquid turbulence within thin films could not be fully resolved. Consequently, the enhancement factor did not emerge naturally when the reaction was activated and was therefore explicitly implemented along with the developed UDF model.
- Constant thermophysical properties were used along the packing height. In practical operation, temperature and composition may vary axially, which can affect viscosity, diffusivity, solubility, and reaction kinetics; neglecting these variations may introduce deviations in the predicted $K_g a_e$.
- The REU framework represents an idealized periodic section of the packing and does not capture column-scale effects such as inlet maldistribution, large-scale flow redistribution, and axial development of gas–liquid contact. These non-idealities can influence the experimentally observed effective interfacial renewal and thus $K_g a_e$.
- For scaled-up columns, the variation of material properties along the column height becomes significant; in this study, the short column length minimizes such effects.

The outlook and future recommendations can be summarized as follows:

- Extend the geometric realism by incorporating embossing, perforations, and sheet joints, and quantify their influence on h_L, a_e, and $K_G a_\mathrm{e}$; include partial wetting and surface roughness effects through dedicated submodels.

- The current configuration with stacked REUs imposes limited liquid distribution; hence, the framework can be extended to a full-scale column to capture large-scale flow development.
- Implement a non-ideal solution property framework (including binary interaction effects) to enable composition-dependent thermophysical properties and more realistic axial variation of mixture behavior along the column height.
- Future work may also investigate flooding and entrainment phenomena under higher gas loads.

Overall, the study shows that once dry-gas behavior is calibrated, a single-REU, interface-resolving CFD model can estimate the coupled hydrodynamics and reactive absorption of structured packings with the right trends and magnitudes, offering an expandable tool for packing screening, design, and future scale-up.

REFERENCES

[1] R. Billet, M. Schultes, "Prediction of mass transfer columns with dumped and arranged packings: Updated summary of the calculation method of billet and schultes," *Chemical Engineering Research and Design*, vol. 77, no. 6, pp. 498–504, 1999, issn: 0263-8762. doi: https://doi.org/10.1205/026387699526520.

[2] P. Suess, L. Spiegel, "Hold-up of mellapak structured packings," *Chemical Engineering and Processing: Process Intensification*, vol. 31, no. 2, pp. 119–124, 1992, issn: 0255-2701. doi: https://doi.org/10.1016/0255-2701(92)85005-M. [Online]. Available: https://www.sciencedirect.com/science/article/pii/025527019285005M.

[3] A. A. Kiss, R. Smith, "Rethinking energy use in distillation processes for a more sustainable chemical industry," *Energy*, vol. 203, p. 117 788, 2020, issn: 0360-5442. doi: 10.1016/j.energy.2020.117788.

[4] N. J. Czarnecki, L. Giannetti, S. A. Owens, S. Barnicki, R. B. Eldridge, "Energy and economic evaluation of wall placement for divided wall distillation columns," *Industrial & Engineering Chemistry Research*, vol. 63, no. 43, pp. 18 513–18 524, 2024. doi: 10.1021/acs.iecr.4c01691.

[5] Elsevier, *Scopus Database*, https://www.scopus.com, Data retrieved on May 24, 2025.

[6] G. Towler, R. Sinnott, "Chapter 17 - separation columns (distillation, absorption, and extraction)," in *Chemical Engineering Design (Second Edition)*, Second Edition, Boston: Butterworth-Heinemann, 2013, pp. 807–935, isbn: 978-0-08-096659-5. doi: https://doi.org/10.1016/B978-0-08-096659-5.00017-1.

[7] H. Versteeg, W. Malalasekera, *An Introduction to Computational Fluid Dynamics: The Finite Volume Method*. Pearson Education Limited, 2007, isbn: 9780131274983.

[8] R. Bird, W. Stewart, E. Lightfoot, *Transport Phenomena*. Wiley, 2006, isbn: 9780470115398.

[9] Sulzer Chemtech Ltd, *Structured packings for distillation, absorption and reactive distillation*, Brochure reviewed and supplemented in 2002/2003, Sulzer Chemtech Ltd, Winterthur, Switzerland, 2003. [Online]. Available: https://www.sulzer.com/en/shared/documents/packings/Structured_Packings_Mellapak.pdf.

[10] R. K. Singh, J. Bao, C. Wang, Y. Fu, Z. Xu, "Hydrodynamics of countercurrent flows in a structured packed column: Effects of initial wetting and dynamic contact angle," *Chemical Engineering Journal*, vol. 398, p. 125 548, 2020, issn: 1385-8947. doi: https://doi.org/10.1016/j.cej.2020.125548.

[11] A. S. Ambekar, E. Peters, O. Hinrichsen, V. V. Buwa, J. Kuipers, "Understanding the role of perforations on the local hydrodynamics of gas–liquid flows through structured packings," *Chemical Engineering Journal*, vol. 486, p. 150 084, 2024, issn: 1385-8947. doi: https://doi.org/10.1016/j.cej.2024.150084.

[12] A. Ataki, H.-J. Bart, "Experimental and cfd simulation study for the wetting of a structured packing element with liquids," *Chemical Engineering & Technology*, vol. 29, no. 3, pp. 336–347, 2006. doi: https://doi.org/10.1002/ceat.200500302. eprint: https://onlinelibrary.wiley.com/doi/pdf/10.1002/ceat.200500302.

[13] S. Shojaee, S. H. Hosseini, B. S. Razavi, "Computational fluid dynamics simulation of multiphase flow in structured packings," *Journal of Applied Mathematics*, vol. 2012, no. 1, p. 917 650, 2012. doi: https://doi.org/10.1155/2012/917650.

[14] Q. Wang, X. Liu, X. Wu, C. Yang, T. Qiu, "A multi-scale approach to optimize vapor-liquid mass transfer layer in structured catalytic packing," *Chemical Engineering Science*, vol. 214, p. 115 434, 2020, issn: 0009-2509. doi: https://doi.org/10.1016/j.ces.2019.115434.

[15] A. Olenberg, E. Y. Kenig, "Numerical simulation of two phase flow in representative elements of structured packings," Computer Aided Chemical Engineering, vol. 40, pp. 2089–2094, 2017, issn: 1570-7946. doi: 10.1016/B978-0-444-63965-3.50350-0.

[16] R. E. Tsai, "Mass transfer area of structured packing," Advisors: Gary T. Rochelle and R. Bruce Eldridge, Ph.D. Dissertation, The University of Texas at Austin, Austin, Texas, May 2010.

[17] M. Wehrli, T. Kogl, T. Linder, W. Arlt, "An unobstructed view of liquid flow in structured packing," *Chemical Engineering Transactions*, vol. 69, pp. 775–780, Oct. 2018. doi: 10.3303/CET1869130.

[18] S. Schug, "Untersuchung der fluiddynamik in packungskolonnen mittels computertomographie," Gutachter: Wolfgang Arlt, Ph.D. dissertation, Friedrich-Alexander-Universität Erlangen-Nürnberg, Erlangen, Germany, Jan. 2018.

[19] A. Aroonwilas, P. Tontiwachwuthikul, A. Chakma, "Effects of operating and design parameters on co2 absorption in columns with structured packings," *Separation and Purification Technology*, vol. 24, no. 3, pp. 403–411, 2001, issn: 1383-5866. doi: https://doi.org/10.1016/S1383-5866(01)00140-X.

[20] X. Wu, M. He, Y. Yu, Z. Qin, Z. Zhang, "Overall mass transfer coefficient of co2 absorption in a diameter-varying spray tower," *Energy Procedia*, vol. 114, pp. 1665–1670, 2017, 13th International Conference on Greenhouse Gas Control Technologies, GHGT-13, 14-18 November 2016, Lausanne, Switzerland, issn: 1876-6102. doi: https://doi.org/10.1016/j.egypro.2017.03.1295.

[21] D. Flagiello, A. Parisi, A. Lancia, F. Di Natale, "A review on gas-liquid mass transfer coefficients in packed-bed columns," *ChemEngineering*, vol. 5, no. 3, 2021, issn: 2305-7084. doi: 10.3390/chemengineering5030043.

[22] Ž. Olujić, "Effect of column diameter on pressure drop of a corrugated sheet structured packing," *Chemical Engineering Research and Design*, vol. 77, no. 6, pp. 505–510, 1999, issn: 0263-8762. doi: https://doi.org/10.1205/026387699526539.

[23] Ž. Olujić, A. Kamerbeek, J. de Graauw, "A corrugation geometry based model for efficiency of structured distillation packing," *Chemical Engineering and Processing: Process Intensification*, vol. 38, no. 4, pp. 683–695, 1999, issn: 0255-2701. doi: 10.1016/S0255-2701(99)00068-9.

[24] S. A. Owens, "Advanced analysis of structured packing via computational fluid dynamics simulation," Available through the UT Electronic Theses and Dissertations repository, Ph.D. Dissertation, The University of Texas at Austin, Austin, Texas, 2010.

[25] M. A. Basden, "Characterization of structured packing via computational fluid dynamics," Available through the UT Electronic Theses and Dissertations repository, Ph.D. dissertation, The University of Texas at Austin, Austin, Texas, Dec. 2014, p. 277.

[26] J. A. Rocha, J. L. Bravo, J. R. Fair, "Distillation columns containing structured packings: A comprehensive model for their performance. 1. hydraulic models," *Industrial & Engineering Chemistry Research*, vol. 32, no. 4, pp. 641–651, 1993. doi: 10.1021/ie00016a010.

[27] R. Billet, M. Schultes, "Predicting mass transfer in packed columns," *Chemical Engineering & Technology*, vol. 16, no. 1, pp. 1–9, 1993. doi: https://doi.org/10.1002/ceat.270160102.

[28] H. T. Kakusaburo Onda, Y. Okumoto, "Mass transfer coefficients between gas and liquid phases in packed columns," *Journal of Chemical Engineering of Japan*, vol. 1, no. 1, pp. 56–62, 1968. doi: 10.1252/jcej.1.56.

[29] M. H. de Brito, U. von Stockar, A. M. Bangerter, P. Bomio, M. Laso, "Effective mass-transfer area in a pilot plant column equipped with structured packings and with ceramic rings," *Industrial & Engineering Chemistry Research*, vol. 33, no. 3, pp. 647–656, 1994. doi: 10.1021/ie00027a023.

[30] J. Stichlmair, J. Bravo, J. Fair, "General model for prediction of pressure drop and capacity of countercurrent gas/liquid packed columns," *Gas Separation Purification*, vol. 3, no. 1, pp. 19–28, 1989, issn: 0950-4214. doi: 10.1016/0950-4214(89)80016-7.

[31] M. Isoz, J. Haidl, "Computational-fluid-dynamics analysis of gas flow through corrugated-sheet-structured packing: Effects of packing geometry," *Industrial & Engineering Chemistry Research*, vol. 57, no. 34, pp. 11 785–11 796, 2018. doi: 10.1021/acs.iecr.8b00676.

[32] Bertling, "Simulation of liquid flow in structured packings using cfd methods," *Chemical Engineering Science*, vol. 269, p. 118 405, 2023. doi: https://doi.org/10.1016/j.ces.2022.118405.

[33] R. K. Singh, J. E. Galvin, X. Sun, "Multiphase flow studies for microscale hydrodynamics in the structured packed column," *Chemical Engineering Journal*, vol. 353, pp. 949–963, 2018, issn: 1385-8947. doi: 10.1016/j.cej.2018.07.067.

[34] K. Nikou, Ehsani, "Turbulence models application on cfd simulation of hydrodynamics, heat and mass transfer in a structured packing," *International Communications in Heat and Mass Transfer*, vol. 35, no. 9, pp. 1211–1219, 2008, issn: 0735-1933. doi: 10.1016/j.icheatmasstransfer.2008.05.017.

[35] J. A. Rocha, J. L. Bravo, J. R. Fair, "Distillation columns containing structured packings: a comprehensive model for their performance. 2. mass-transfer model," *Industrial & Engineering Chemistry Research*, vol. 35, no. 5, pp. 1660–1667, 1996. doi: 10.1021/ie940406i.

[36] C. Wang, "Mass transfer coefficients and effective area of packing," Ph.D. dissertation, The University of Texas at Austin, Austin, TX, Mar. 2015.

[37] Q. Xu, "Thermodynamics of co_2 loaded aqueous amines," Advisor: Gary T. Rochelle; Committee: Keith Johnston, Isaac Sanchez, Frank Seibert, Steven Bryant, Ph.D. Dissertation, The University of Texas at Austin, Austin, Texas, Dec. 2011.

[38] A. Aboudheir, P. Tontiwachwuthikul, A. Chakma, R. Idem, "Kinetics of the reactive absorption of carbon dioxide in high co_2-loaded, concentrated aqueous monoethanolamine solutions," *Chemical Engineering Science*, vol. 58, pp. 5195–5210, 2003. doi: https://doi.org/10.1016/j.ces.2003.08.014.

[39] A. Aroonwilas, A. Chakma, P. Tontiwachwuthikul, A. Veawab, "Mathematical modelling of mass transfer and hydrodynamics in co_2 absorbers packed with structured packings," *Chemical Engineering Science*, vol. 58, pp. 4037–4053, 2003. doi: https://doi.org/10.1016/S0009-2509(03)00315-4.

[40] G. Puxty, R. Rowland, M. Attalla, "Comparison of the rate of co2 absorption into aqueous ammonia and monoethanolamine," *Chemical Engineering Science*, vol. 65, no. 2, pp. 915–922, 2010, issn: 0009-2509. doi: 10.1016/j.ces.2009.09.042.

[41] R. Notz, H. P. Mangalapally, H. Hasse, "Post combustion co_2 capture by reactive absorption: Pilot plant description and results of systematic studies with mea," *International Journal of Greenhouse Gas Control*, vol. 6, pp. 84–112, 2012. doi: https://doi.org/10.1016/j.ijggc.2011.11.004.

[42] T. L. Sønderby, K. B. Carlsen, P. L. Fosbøl, L. G. Kiørboe, N. von Solms, "A new pilot absorber for co_2 capture from flue gases: Measuring and modelling capture with mea solution," *International Journal of Greenhouse Gas Control*, vol. 12, pp. 181–192, 2013. doi: https://doi.org/10.1016/j.ijggc.2012.10.010.

[43] A. Krótki, L. Więcław-Solny, A. Tatarczuk, T. Spietz, T. Chwoła, S. Dobras, "A pilot study comparing mea and aeea solvents in carbon capture," *International Journal of Greenhouse Gas Control*, vol. 126, p. 103 891, 2023. doi: https://doi.org/10.1016/j.ijggc.2023.103891.

[44] J. Chen, C. Liu, X. Yuan, G. Yu, "Cfd simulation of flow and mass transfer in structured packing distillation columns," *Chinese Journal of Chemical Engineering*, vol. 17, no. 3, pp. 381–388, Jun. 2009, Received 23 October 2008; accepted 2 March 2009.

[45] L. H. Macfarlan, A. F. Seibert, M. T. Phan, R. B. Eldridge, "Cfd-based study on structured packing geometry," *Chemical Engineering Science*, vol. 243, p. 116 767, 2021, issn: 0009-2509. doi: https://doi.org/10.1016/j.ces.2021.116767.

[46] D. A. Pham, Y.-I. Lim, H. Jee, E. Ahn, Y. Jung, "Porous media eulerian computational fluid dynamics (cfd) model of amine absorber with structured-packing for co2 removal," *Chemical Engineering Science*, vol. 132, pp. 259–270, 2015, issn: 0009-2509. doi: https://doi.org/10.1016/j.ces.2015.04.009.

[47] L. H. Macfarlan, M. T. Phan, R. Bruce Eldridge, "A volume-of-fluid methodology for interfacial mass transfer," *Chemical Engineering Science*, vol. 275, p. 118 720, 2023, issn: 0009-2509. doi: https://doi.org/10.1016/j.ces.2023.118720.

[48] B. Sun, T. Bhatelia, R. P. Utikar, G. M. Evans, V. K. Pareek, "Study on hydrodynamic performance of structured packings for gas-liquid flow: Effects of geometry parameters," *Chemical Engineering Research and Design*, vol. 167, pp. 318–326, 2021. doi: https://doi.org/10.1016/j.cherd.2021.01.003.

[49] C. Zeng, Y. Fu, R. Singh, J. Bao, Z. Xu, "Differentiation of static and dynamic interfacial area in the structured packed column," *Chemical Engineering Science*, vol. 260, p. 117 877, 2022, issn: 0009-2509. doi: https://doi.org/10.1016/j.ces.2022.117877.

[50] C. Gu, R. Zhang, X. Zhi, S. Zhu, L. Qiu, "Numerical investigation on the flow characteristics of liquid oxygen and water in the structured packing," *Cryogenics*, vol. 110, p. 103 140, 2020. doi: https://doi.org/10.1016/j.cryogenics.2020.103140.

[51] B. Sun, W. S. Tan, T. Bhatelia, V. K. Pareek, "Study on the hydrodynamics of structured packing: Liquid holdup and pressure drop of a novel 3d printed packing," *Chemical Engineering Research and Design*, vol. 206, pp. 200–209, 2024. doi: https://doi.org/10.1016/j.cherd.2024.05.006.

[52] J. Neukäufer, F. Hanusch, M. Kutscherauer, S. Rehfeldt, H. Klein, T. Grützner, "Methodology for the development of additively manufactured packings in thermal separation technology," *Chemical Engineering & Technology*, vol. 42, no. 9, pp. 1970–1977, 2019. doi: https://doi.org/10.1002/ceat.201900220.

[53] J. Neukäufer et al., "Development of enhanced three-dimensional printed packings for scale-up of distillation columns: A successful case study," *AIChE Journal*, vol. 69, no. 3, 2023. doi: https://doi.org/10.1002/aic.17902.

[54] N. Rausch et al., "Simulation of the liquid flow distribution in laboratory-scale additively manufactured structured packings," *Chemical Engineering Research and Design*, vol. 196, pp. 28–39, 2023. doi: https://doi.org/10.1016/j.cherd.2023.06.035.

[55] Y. G. Shah, A. C. Jackson, C. Tsouris, C. E. Finney, G. Panagakos, "Multiphase computational fluid dynamics modeling of reacting flows in absorption columns for carbon capture," *Digital Chemical Engineering*, vol. 16, p. 100 252, 2025, issn: 2772-5081. doi: https://doi.org/10.1016/j.dche.2025.100252.

[56] P. Niegodajew, D. Asendrych, "Amine based co2 capture – cfd simulation of absorber performance," *Applied Mathematical Modelling*, vol. 40, no. 23, pp. 10 222–10 237, 2016. doi: https://doi.org/10.1016/j.apm.2016.07.003.

[57] J. Tao, H. Zhang, X. Zheng, Z. Lin, Z. Zhu, "Study on the performance of a baffle demister for improving the separation efficiency of small droplets," *Chemical Engineering Research and Design*, vol. 196, pp. 118–132, 2023. doi: https://doi.org/10.1016/j.cherd.2023.06.011.

[58] S. N. Shoghl, A. Naderifar, F. Farhadi, G. Pazuki, "Optimization of separator internals design using cfd modeling in the joule-thomson process," *Journal of Natural Gas Science and Engineering*, vol. 89, p. 103 889, 2021. doi: https://doi.org/10.1016/j.jngse.2021.103889.

[59] P. Bender, A. Moll, "Modifications to structured packings to increase their capacity," *Chemical Engineering Research and Design*, vol. 81, no. 1, pp. 58–67, 2003. doi: 10.1205/026387603321158195.

[60] Z. Olujić, H. Jansen, B. Kaibel, T. Rietfort, E. Zich, "Stretching the capacity of structured packings," *Industrial & Engineering Chemistry Research*, vol. 40, no. 26, pp. 6172–6180, 2001. doi: 10.1021/ie010323j.

[61] B. Hanley, "On packed column hydraulics," *AIChE Journal*, vol. 58, no. 6, pp. 1671–1682, 2012. doi: https://doi.org/10.1002/aic.12706.

[62] V. Wolf-Zöllner, F. Seibert, M. Lehner, "Extended performance comparison of different pressure drop, hold-up and flooding point correlations for packed columns," *Chemical Engineering Research and Design*, vol. 147, pp. 699–708, 2019. doi: 10.1016/j.cherd.2019.05.028.

[63] V. Bontozoglou, K. Serifi, "Falling film flow along steep two-dimensional topography: The effect of inertia," *International Journal of Multiphase Flow*, vol. 34, no. 8, pp. 734–747, 2008. doi: 10.1016/j.ijmultiphaseflow.2008.01.006.

[64] R. E. Tsai, A. F. Seibert, R. B. Eldridge, G. T. Rochelle, "A dimensionless model for predicting the mass transfer area of structured packing," *AIChE Journal*, vol. 57, no. 5, pp. 1173–1184, 2011. doi: 10.1002/aic.12345.

[65] R. E. Tsai et al., "Influence of surface tension on effective packing area," *Industrial & Engineering Chemistry Research*, vol. 47, no. 4, pp. 1253–1260, 2008. doi: 10.1021/ie0707801.

[66] S. A. Jayarathna, C. K. Jayarathna, D. A. Kottage, S. Dayarathna, D. A. Eimer, M. C. Melaaen, "Density and surface tension measurements of partially carbonated aqueous monoethanolamine solutions," *Journal of Chemical and Engineering Data*, vol. 58, no. 2, pp. 343–348, 2013. doi: 10.1021/je300920t.

[67] C. W. Hirt, B. D. Nichols, "Volume of fluid (vof) method for the dynamics of free boundaries," *Journal of Computational Physics*, vol. 39, no. 1, pp. 201–225, 1981. doi: 10.1016/0021-9991(81)90145-5.

[68] J. U. Brackbill, D. B. Kothe, C. Zemach, "A continuum method for modeling surface tension," *Journal of Computational Physics*, vol. 100, no. 2, pp. 335–354, 1992. doi: 10.1016/0021-9991(92)90240-Y.

[69] C. W. Hirt, B. D. Nichols, "Volume of fluid (vof) method for the dynamics of free boundaries," *Journal of Computational Physics*, vol. 39, no. 1, pp. 201–225, 1981. doi: 10.1016/0021-9991(81)90145-5.

[70] H. Benbelkacem, H. Debellefontaine, "Modeling of a gas–liquid reactor in batch conditions. study of the intermediate regime when part of the reaction occurs within the film and part within the bulk," *Chemical Engineering and Processing: Process Intensification*, vol. 42, no. 10, pp. 723–732, 2003, issn: 0255-2701.

[71] R. Sander, "Compilation of henry's law constants (version 4.0) for water as solvent," *Atmospheric Chemistry and Physics*, vol. 15, no. 8, pp. 4399–4981, 2015. doi: 10.5194/acp-15-4399-2015.

[72] B. R. W. Pinsent, L. Pearson, F. J. W. Roughton, "The kinetics of combination of carbon dioxide with hydroxide ions," *Transactions of the Faraday Society*, vol. 52, pp. 1512–1520, 1956. doi: 10.1039/TF9565201512.

[73] W. J. Thomas, M. J. Adams, "Measurement of the diffusion coefficients of carbon dioxide and nitrous oxide in water and aqueous solutions of glycerol," *Transactions of the Faraday Society*, vol. 61, pp. 668–673, 1965. doi: 10.1039/TF9656100668.

[74] P. M. Knupp, "Algebraic mesh quality metrics," *SIAM Journal on Scientific Computing*, vol. 23, no. 1, pp. 193–218, 2001. doi: 10.1137/S1064827500371499.

[75] J. Pátek, J. Hrubý, A. H. Harvey, "Reference correlations for thermophysical properties of liquid water at 0.1 mpa," *Journal of Physical and Chemical Reference Data*, vol. 38, no. 1, 2009. doi: 10.1063/1.3043575.

[76] *CRC Handbook of Chemistry and Physics*. CRC Press, 2024, Molecular weights for common species.

[77] D. W. Green, M. J. Southard, Eds., *Perry's Chemical Engineers' Handbook*, 8th ed. McGraw Hill, 2008.

[78] J. M. Smith, H. C. Van Ness, M. M. Abbott, *Introduction to Chemical Engineering Thermodynamics*, 7th ed. McGraw Hill, 2005.

[79] W. Sutherland, "The viscosity of gases and molecular force," *Philosophical Magazine*, vol. 36, pp. 507–531, 1893.

[80] B. E. Poling, J. M. Prausnitz, J. P. O'Connell, *The Properties of Gases and Liquids*, 5th ed. McGraw Hill, 2001.

[81] K. G. Joback, R. C. Reid, "Estimation of pure-component properties from group-contributions," *Chemical Engineering Communications*, vol. 57, no. 1-6, pp. 233–243, 1987. doi: 10.1080/00986448708960487.

[82] *Ansys fluent theory guide*, Release 2024 R2, Ansys, Inc., Canonsburg, PA, 2024.

[83] I. A. for the Properties of Water, S. (IAPWS), *Revised release on surface tension of ordinary water substance*, IAPWS Release, Authorized at the IAPWS meeting in Moscow, Russia, 23–27 June 2014, Jun. 2014. [Online]. Available: https://iapws.org/public/documents/CH-L9/Surf-H2O-2014.pdf.

A APPENDIX

A.1 Snapshots of Single-Phase Gas Flow

Geometry of the domain is shown in the Figures A.1,A.2, A.3, composed of four planar sections labeled as A, B, C, and D. The overall dimensions are $X = 5.88 \times 10^{-3}\,\mathrm{m}$, $Y = 8.88 \times 10^{-2}\,\mathrm{m}$, and $Z = 6.22 \times 10^{-3}\,\mathrm{m}$. Section C is located at $y = 7.074 \times 10^{-2}\,\mathrm{m}$, and section d is located at $y = 1.41 \times 10^{-2}\,\mathrm{m}$. Sections A and B coincide with the mid-planes at $z = Z/2$ and $x = X/2$, respectively. CFD-results of absolute pressure distribution (Pa) in each section A.1, CFD-results of velocity gradient distribution (m/s) in each section A.2, CFD-results of turbulent kinetic energy distribution $\mathrm{m}^2/\mathrm{s}^2$) in each section A.3 were given.

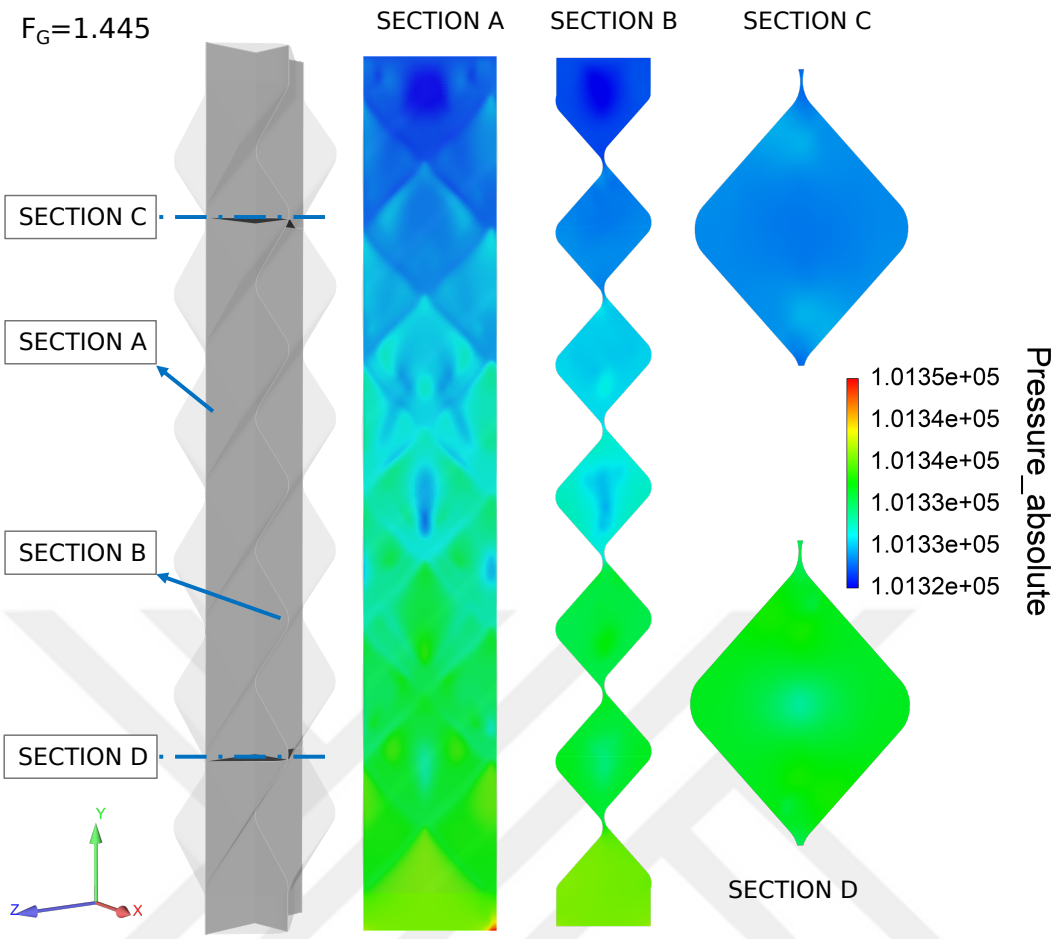


Figure A.1 Pressure contour of single-phase sectioned view for six-REUs at $F_g = 1.445$

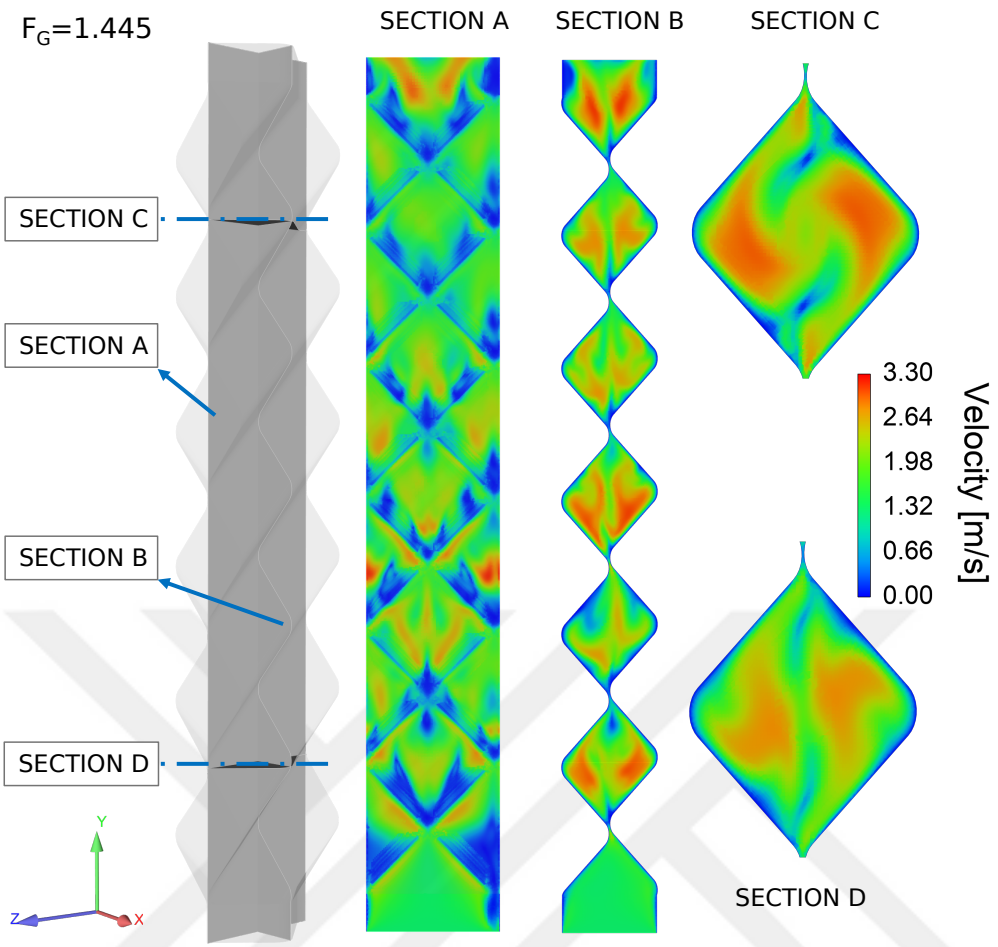


Figure A.2 Velocity contour of single-phase sectioned view for six-REUs at $F_g = 1.445$

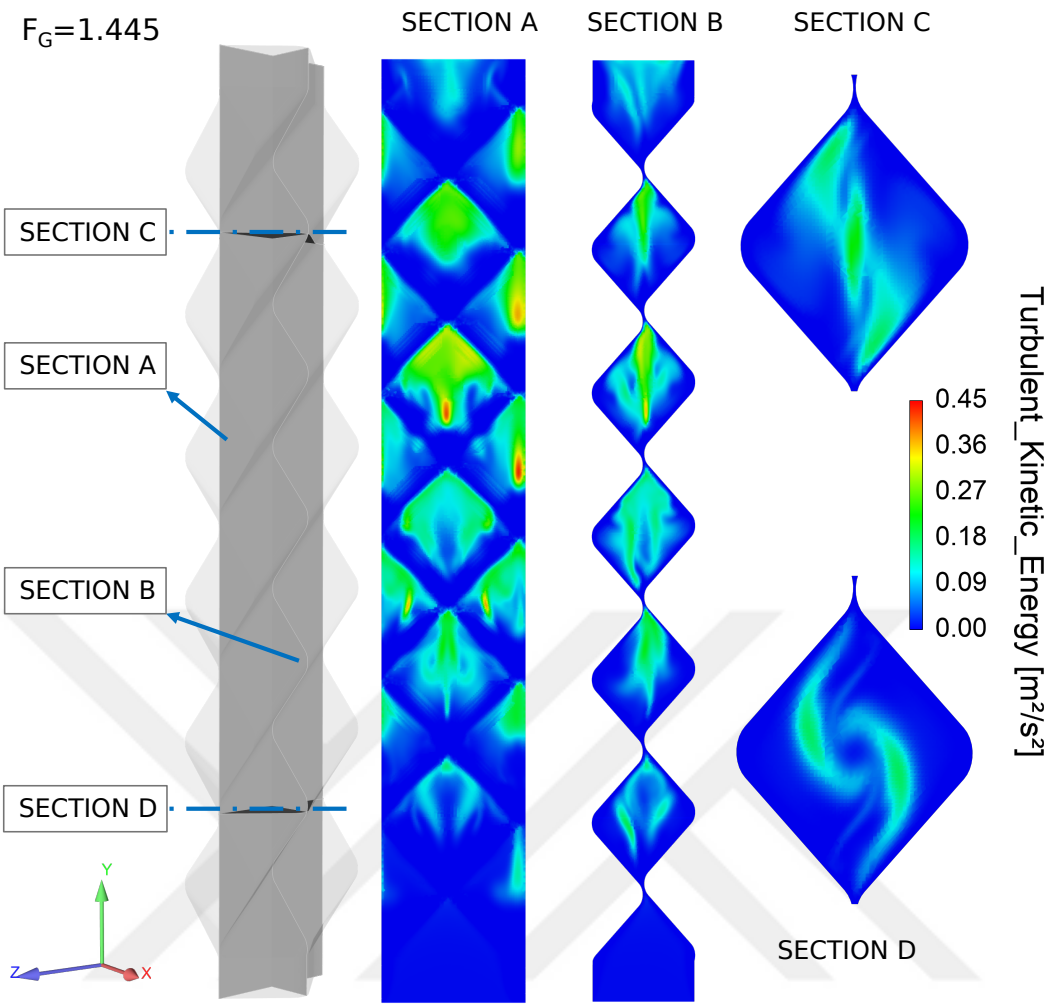


Figure A.3 Turbulent kinetic energy contour of single-phase sectioned view for Six-REUs at $F_g = 1.445$

A.2 Snapshots of Transient Liquid Flow Development

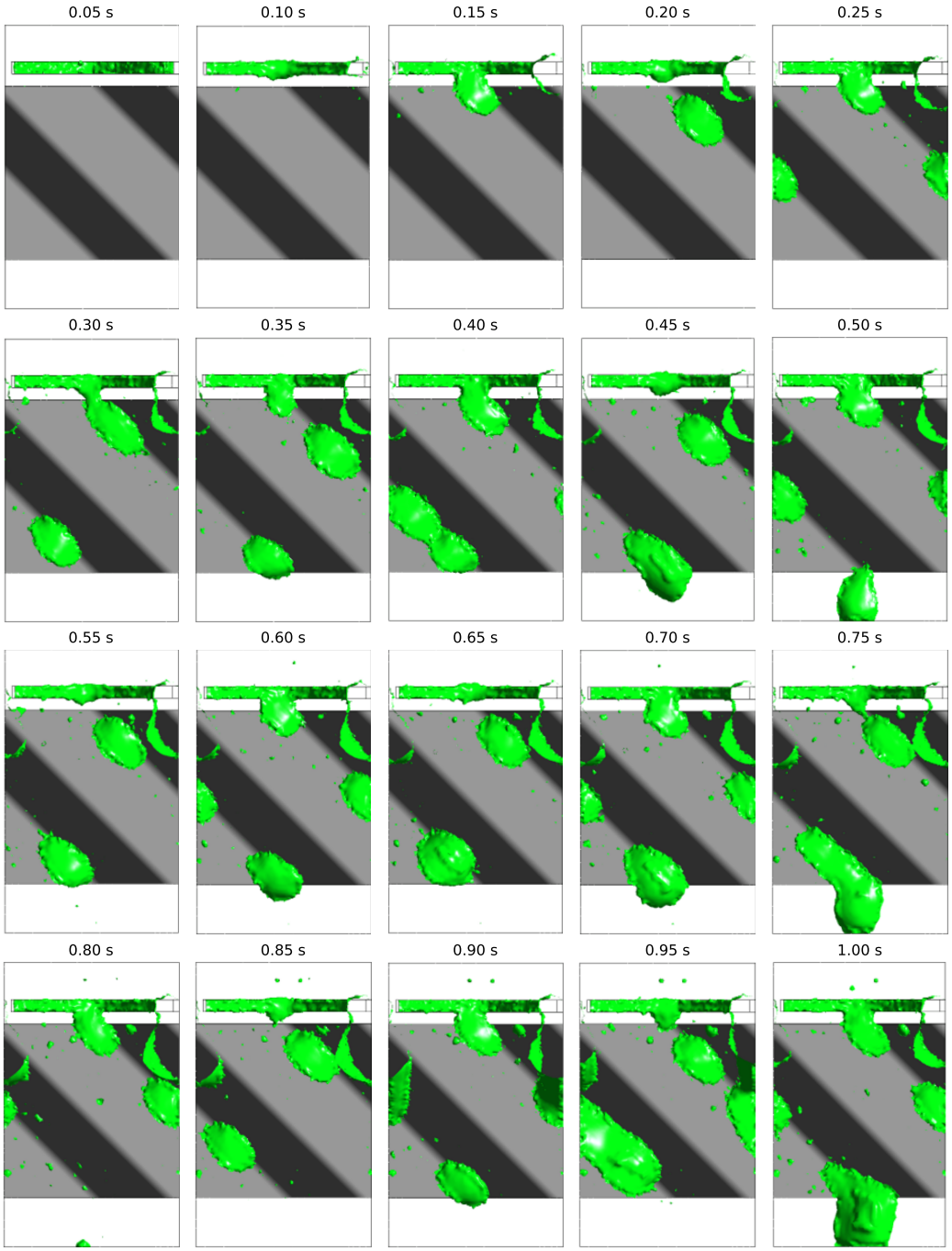


Figure A.4 Two-phase liquid flow streams for 0.05 s to 1.00 s (Water at 25°C, $\theta_{wall} = 70°$, $L = 25\ m^3hm^{-2}$, $F_g = 0.3$, $m/s\ (kg/m^3)^{0.5}h$)

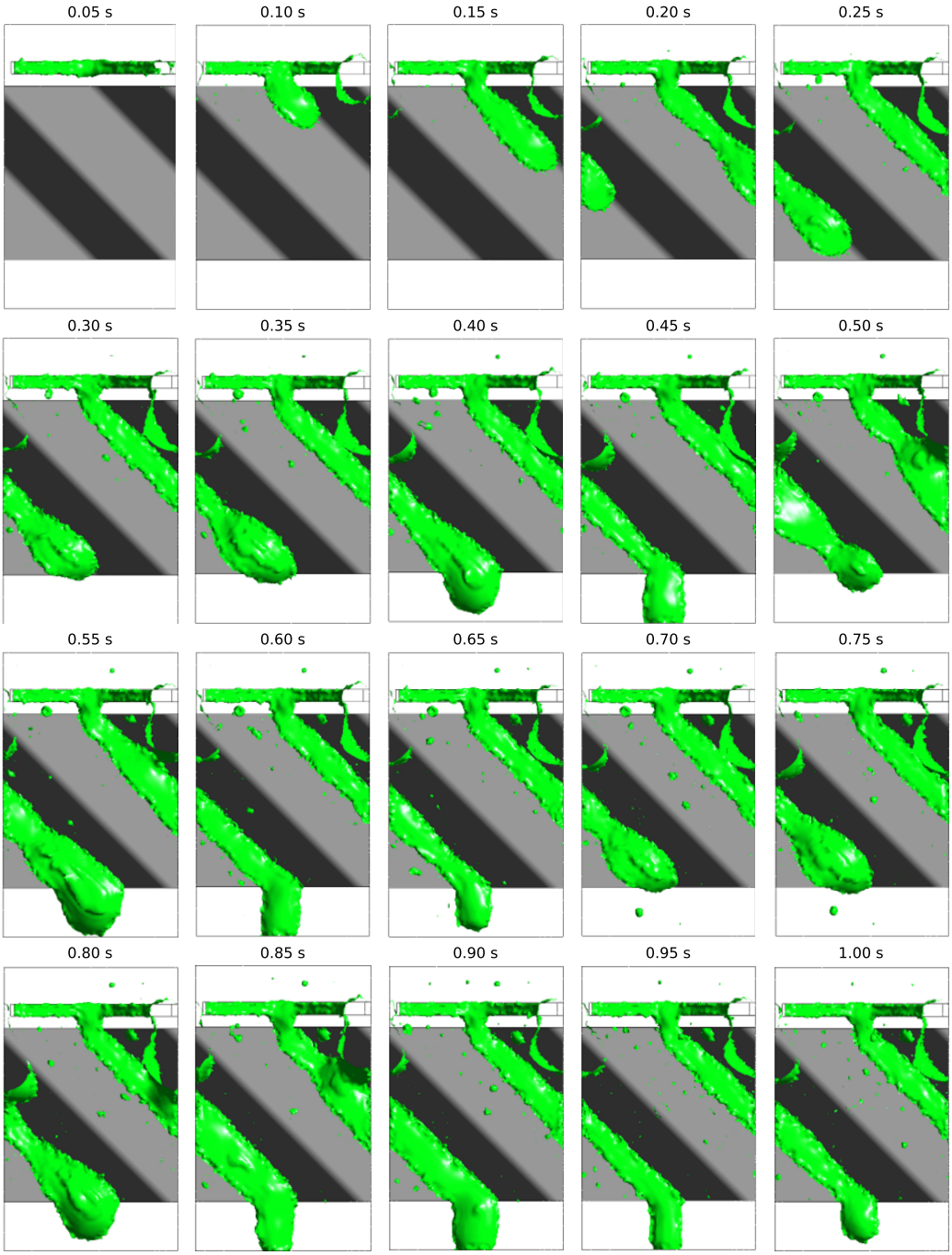


Figure A.5 Two-phase liquid flow streams for 0.05 s to 1.00 s (Water at 25°C, $\theta_{wall} = 70°$, $L = 50\ m^3hm^{-2}$, $F_g = 0.3, m/s\ (kg/m^3)^{0.5}h)$

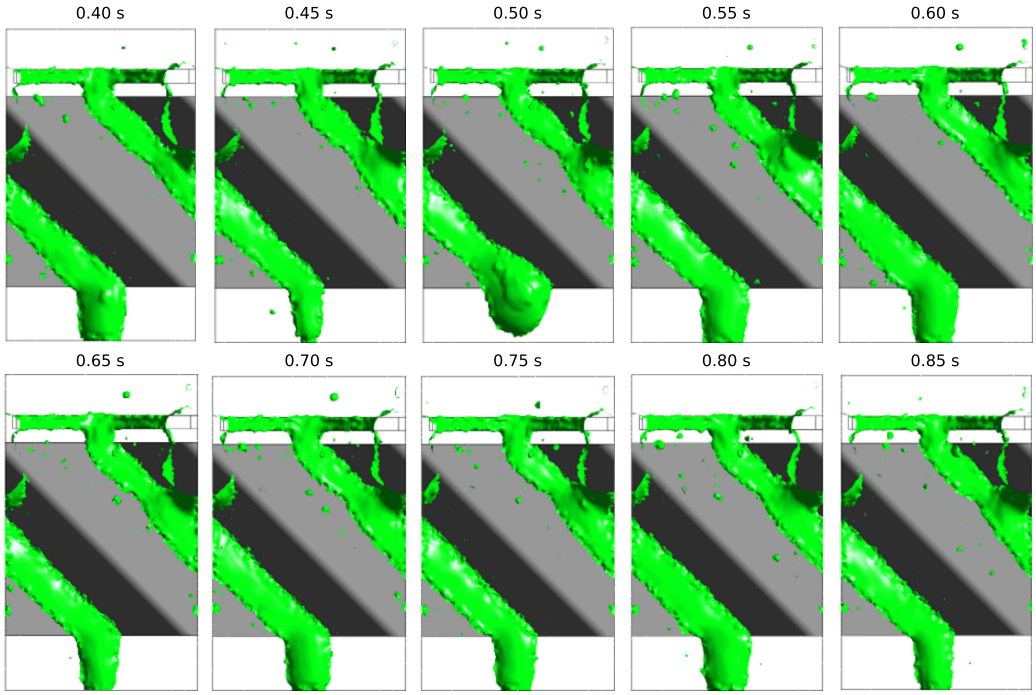


Figure A.6 Two-phase liquid flow streams for 0.40 s to 0.85 s (Water at 25°C, $\theta_{wall} = 70°$, $L = 75\ m^3hm^{-2}$, $F_g = 0.3$, $m/s\ (kg/m^3)^{0.5}h$)

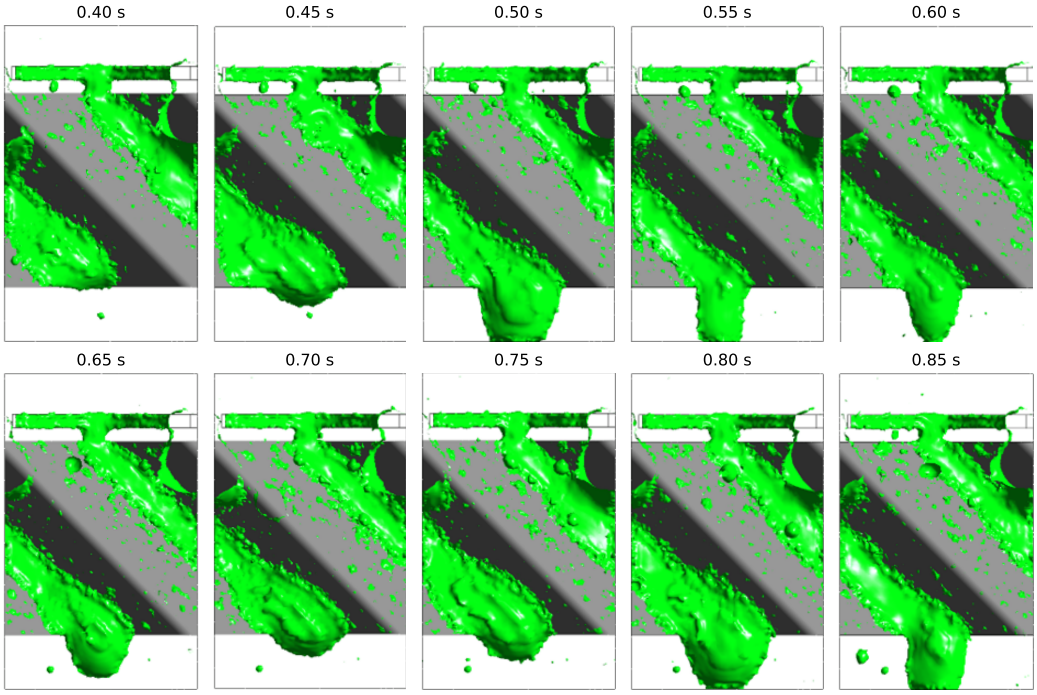


Figure A.7 Two-phase liquid flow streams for 0.40 s to 0.85 s (Water at 25°C, $\theta_{wall} = 45°$, $L = 75\ m^3hm^{-2}$, $F_g = 0.3$, $m/s\ (kg/m^3)^{0.5}h$)

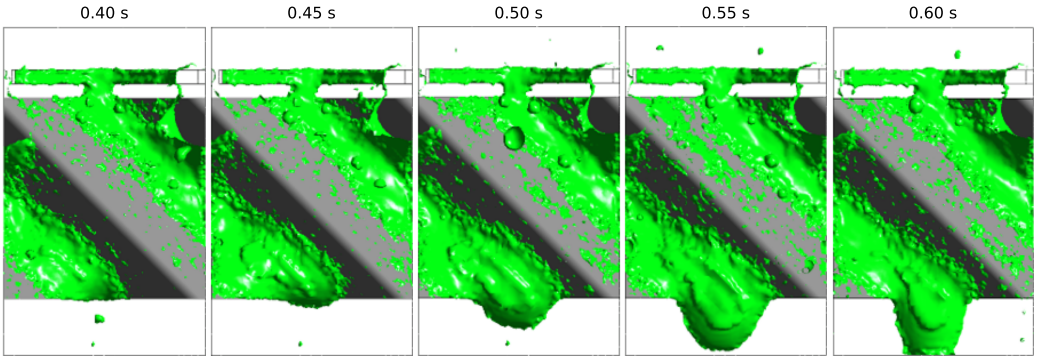


Figure A.8 Two-phase liquid flow streams for 0.40 s to 0.60 s (Water at 25°C, $\theta_{wall} = 30°$, $L = 75\ m^3hm^{-2}$, $F_g = 0.3$, $m/s\ (kg/m^3)^{0.5}h$)

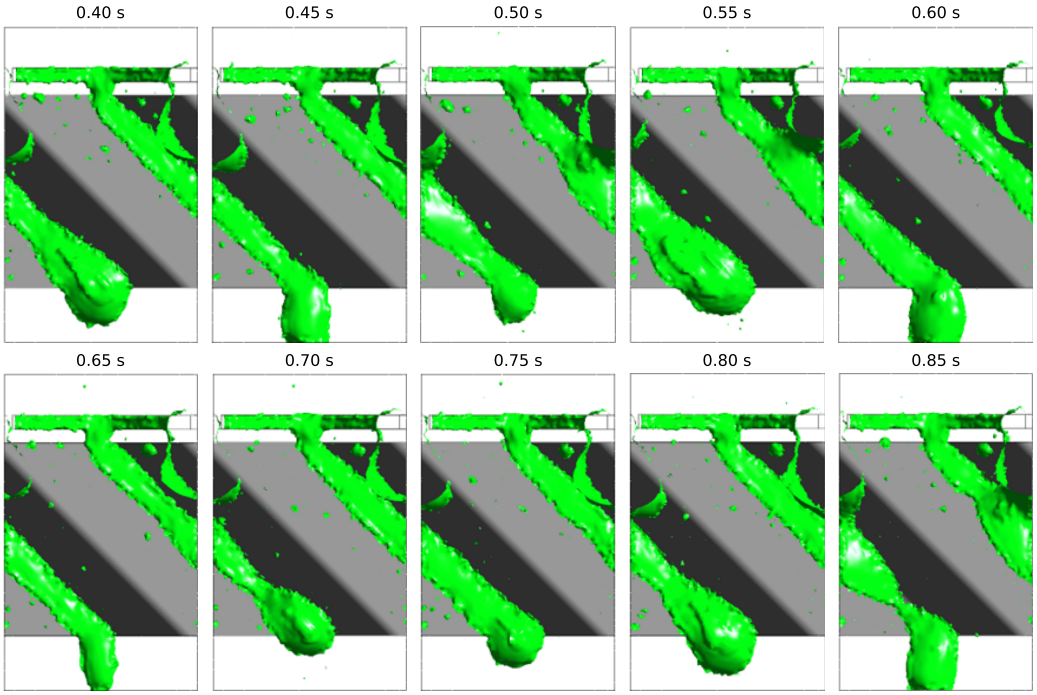


Figure A.9 Two-phase liquid flow streams for 0.40 s to 0.85 s (Water at 25°C, $\theta_{wall} = 70°$, $L = 50\ \ m^3m^{-2}h$, $F_g = 0.633$, $m/s\ (kg/m^3)^{0.5}h$)

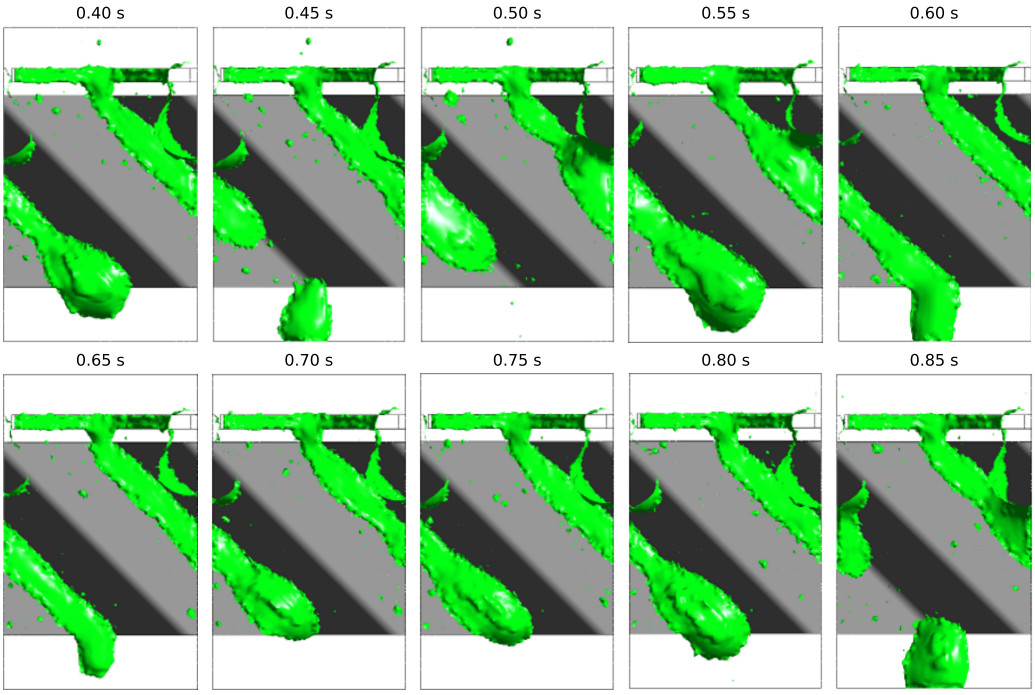


Figure A.10 Two-phase liquid flow streams for 0.40 s to 0.85 s (Water at 25°C, $\theta_{wall} = 70°$, $L = 50\ \ m^3m^{-2}h$, $F_g = 0.900, m/s\ (kg/m^3)^{0.5}h$)

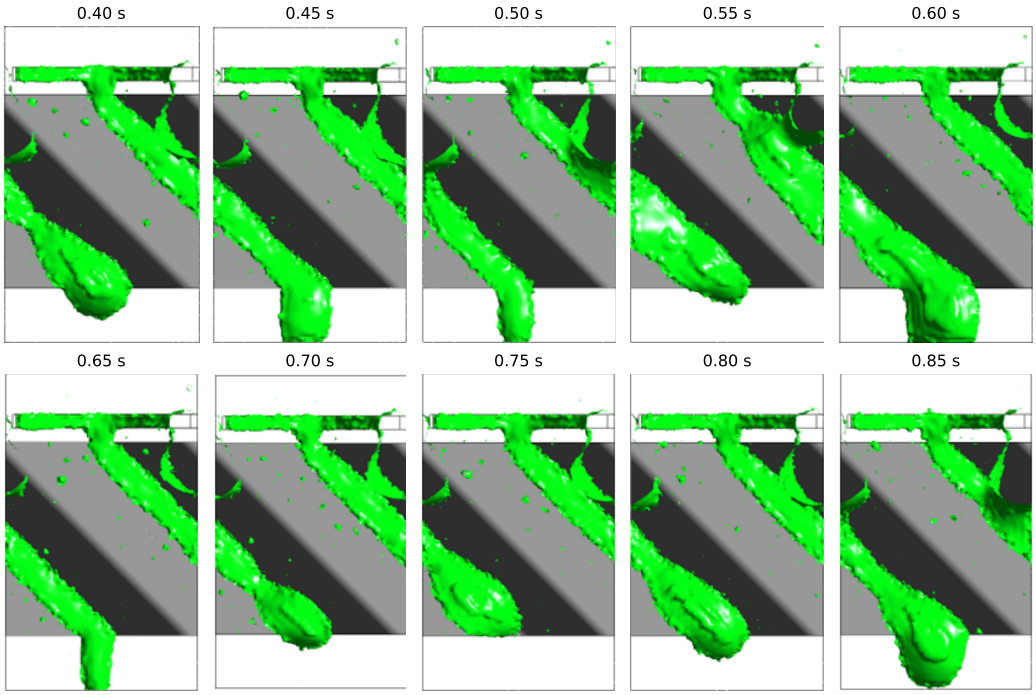


Figure A.11 Two-phase liquid flow streams for 0.40 s to 0.85 s (Water at 25°C, $\theta_{wall} = 70°$, $L = 50\ \ m^3m^{-2}h$, $F_g = 1.084, m/s\ (kg/m^3)^{0.5}h$)

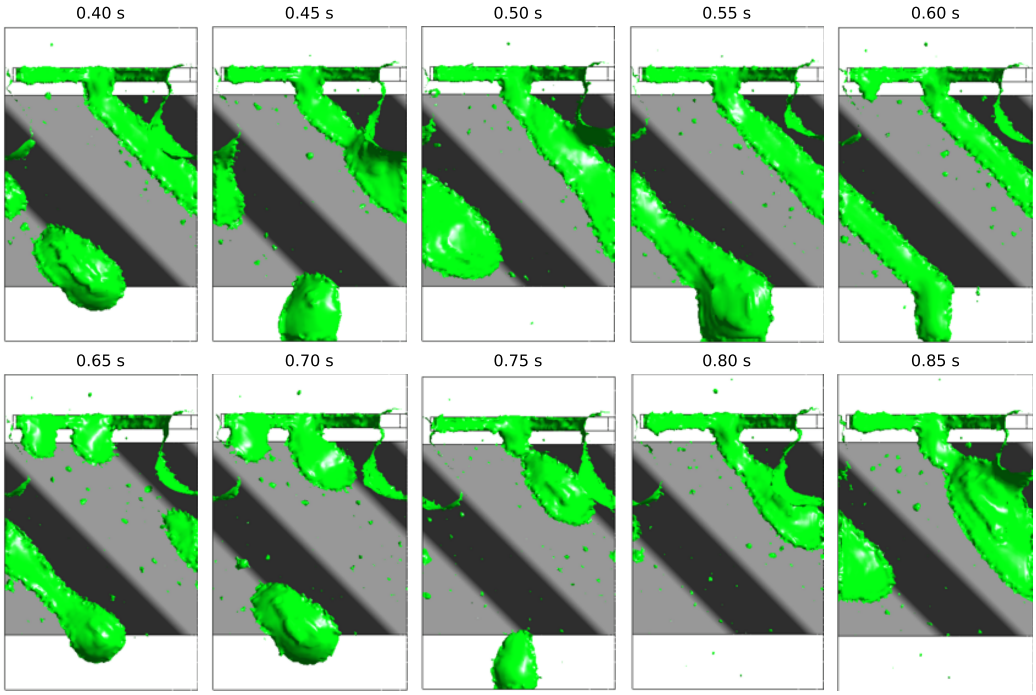


Figure A.12 Two-phase liquid flow streams for 0.40 s to 0.85 s (Water at 25°C, $\theta_{wall} = 70°$, $L = 50\ \ m^3m^{-2}h$, $F_g = 1.355$, $m/s\ (kg/m^3)^{0.5}h$)

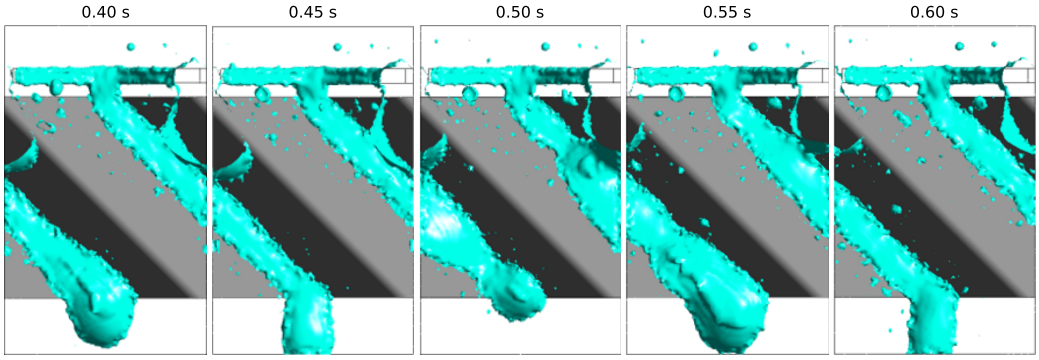


Figure A.13 Two-phase liquid flow streams for 0.40 s to 0.85 s (Water at 25°C, $\theta_{wall} = 70°$, $L = 50\ m^3m^{-2}h$, $F_g = 0.3$, $m/s\ (kg/m^3)^{0.5}h$) at iso-surface $\alpha = 0.3$

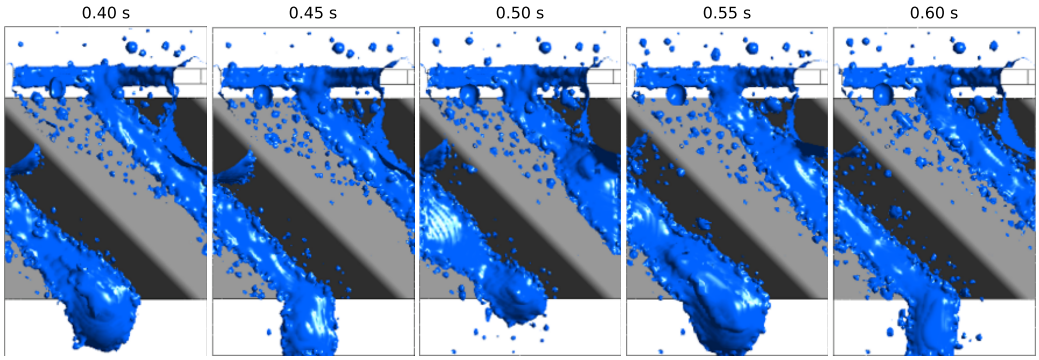


Figure A.14 Two-phase liquid flow streams for 0.40 s to 0.85 s (Water at 25°C, $\theta_{wall} = 70°$, $L = 50\ m^3m^{-2}h$, $F_g = 0.3$, $m/s\ (kg/m^3)^{0.5}h$) at iso-surface $\alpha = 0.1$

A.3 Snapshots of Reactive Gas–Liquid Flow Evolution

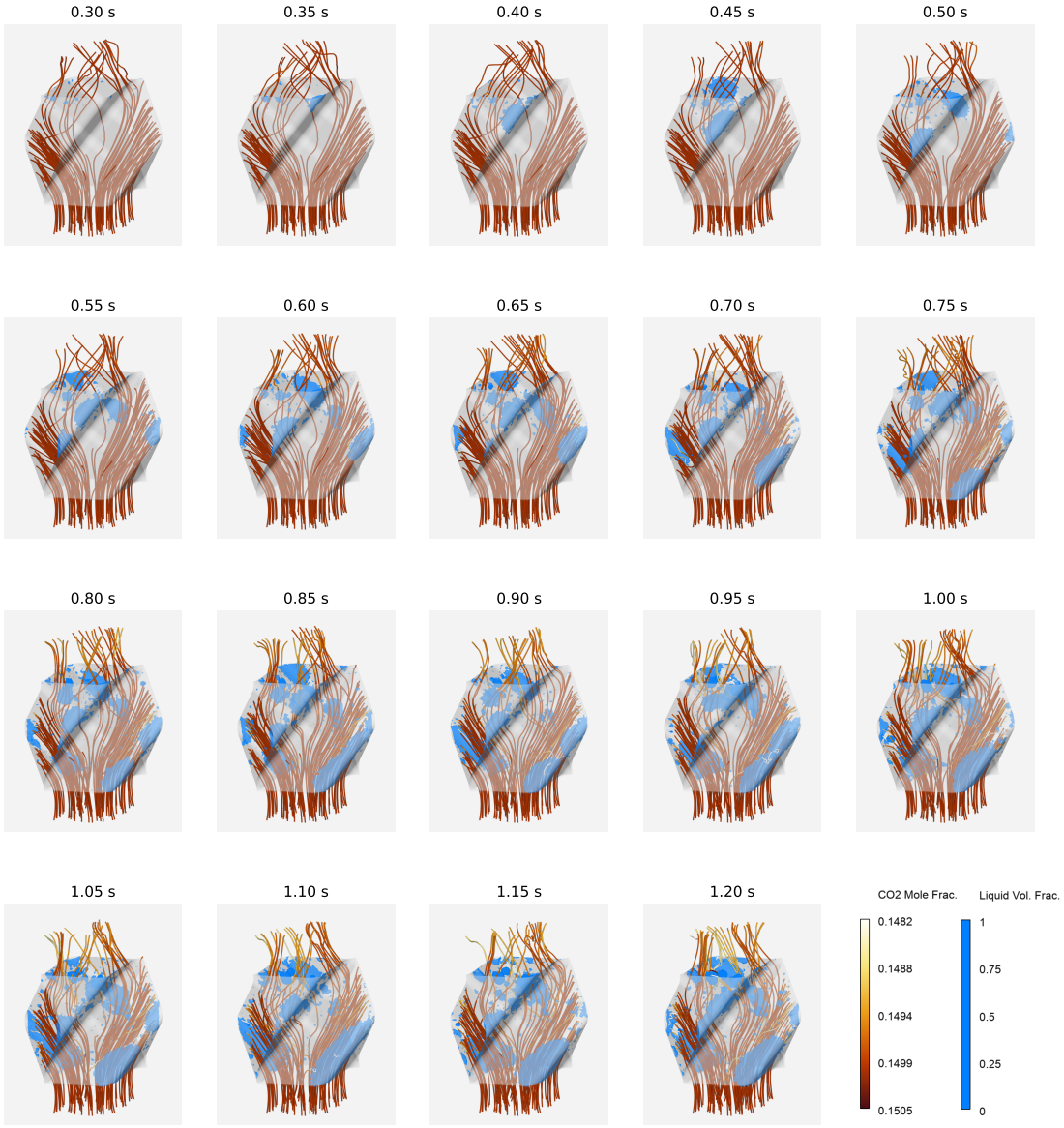


Figure A.15 Reactive absorption for 0.30 s to 1.2 s (MEA ≈20% wt. at 36°C, $\theta_{wall} = 50°$, $L = 23\ m^3 m^{-2} h$, $F_g = 1.3$, $m/s\ (kg/m^3)^{0.5} h$)

A.4 UDF Algorithms

Algorithm 1: VOF Mass Transfer Source for CO_2 in 20 wt% MEA (UDF)

Inputs: cell c on mixture thread t; gas sub-thread index $from_index$; liquid sub-thread index to_index; CO_2 species indices.

Constants:
$M_{\mathrm{CO_2}}, M_{\mathrm{H_2O}}, M_{\mathrm{AIR}}, M_{\mathrm{MEA}}, k_{L0}, D_{\mathrm{CO_2},L}, W_{\mathrm{MEA}}, H_{cp,\mathrm{ref}}, \beta_H, T_{\mathrm{ref}}, \alpha_{\min}, \alpha_{\max}$ and BBox limits.

1. Retrieve sub-threads: $gas \leftarrow \mathrm{THREAD_SUB_THREAD}(t, from_index)$,; $liq \leftarrow \mathrm{THREAD_SUB_THREAD}(t, to_index)$.
2. $\mathbf{x} \leftarrow C_CENTROID(c,t)$; **return** 0 if $\mathbf{x}$ lies outside the BBox.
3. $\alpha_L \leftarrow C_\mathrm{VOF}(c, liq)$; **return** 0 if $\alpha_L \notin [\alpha_{\min}, \alpha_{\max}]$.
4. Read local fields: $Y_g^{\mathrm{CO_2}}, X_L^{\mathrm{CO_2}}, T, \rho_L, P_{\mathrm{abs}}$.
5. $y_{CO_2} \leftarrow \dfrac{Y_g^{\mathrm{CO_2}}/M_{\mathrm{CO_2}}}{Y_g^{\mathrm{CO_2}}/M_{\mathrm{CO_2}} + (1 - Y_g^{\mathrm{CO_2}})/M_{\mathrm{AIR}}}$.
6. $H_{cp}(T) \leftarrow H_{cp,\mathrm{ref}} \exp\!\Big[\beta_H\Big(\dfrac{1}{T} - \dfrac{1}{T_{\mathrm{ref}}}\Big)\Big], \quad H_{px}(T) \leftarrow \dfrac{\rho_L/M_{\mathrm{H_2O}}}{H_{cp}(T)}$.
7. $x_{eq} \leftarrow \dfrac{y_{CO_2} P_{\mathrm{abs}}}{H_{px}(T)}$.
8. $x_L \leftarrow \mathrm{massfrac_to_molefrac_liq}(X_L^{\mathrm{CO_2}})$.
9. $\Delta x \leftarrow x_{eq} - x_L$; **return** 0 if $|\Delta x| < 10^{-12}$.
10. $C_L \leftarrow \mathrm{liquid_molar_density}(\rho_L, X_L^{\mathrm{CO_2}})$.
11. *Chemical enhancement:*
    (a) $c_{\mathrm{MEA}} = \dfrac{W_{\mathrm{MEA}}\rho_L}{M_{\mathrm{MEA}}}$,; $c_{\mathrm{H_2O}} = \dfrac{(1 - W_{\mathrm{MEA}} - X_L^{\mathrm{CO_2}})\rho_L}{M_{\mathrm{H_2O}}}$.
    (b) $k_1 = k_{R\mathrm{NH_2}}(T) c_{\mathrm{MEA}}^2 + k_{\mathrm{H_2O}}(T) c_{\mathrm{H_2O}} c_{\mathrm{MEA}}$.
    (c) $\mathrm{Ha} = \sqrt{D_{\mathrm{CO_2},L} k_1}/k_{L0}$,; $E = \sqrt{1 + \mathrm{Ha}^2}$.
    (d) $k_L \leftarrow k_{L0} E$.
12. $a_{int} \leftarrow \mathrm{interfacial_area_density}(c,t)$.
13. $N \leftarrow k_L\, a_{int}\, C_L\, \Delta x$.
14. $\dot{m} \leftarrow M_{\mathrm{CO_2}}\, N$; **return** $\dot{m}$ (positive $\Rightarrow$ absorption).

Algorithm 2: Dynamic Contact Angle Boundary Profile (UDF) for VOF

Constants: θ_S [deg], Δ [deg], $\mathrm{Ca}_{\max}$ [–], σ [N/m].

1. **For each** boundary face f in thread t:

   (a) $c_0 \leftarrow F_C0(f,t)$; $\quad t_0 \leftarrow \mathrm{THREAD_T0}(t)$.

   (b) $\mu_L \leftarrow C_MU_L(c_0, t_0)$ (liquid viscosity, Pa·s)

   (c) $\mathbf{u} \leftarrow (C_U, C_V, C_W)(c_0, t_0)$; $\quad u_L \leftarrow \|\mathbf{u}\|$.

   (d) $Ca \leftarrow \mu_L\, u_L/\sigma$; $\quad Ca \leftarrow \min(Ca,\, \mathrm{Ca}_{\max})$.

   (e) $\theta_{dyn} \leftarrow \theta_S - \Delta(2\,Ca/\mathrm{Ca}_{\max} - 1)$.

   (f) $\theta_{dyn} \leftarrow \max(\theta_S - \Delta,\, \min(\theta_S + \Delta,\, \theta_{dyn}))$ (clamp)

   (g) $\theta_{\mathrm{rad}} \leftarrow \theta_{dyn} \cdot \pi/180$.

   (h) $F_PROFILE(f, t, \textit{position}) \leftarrow \theta_{\mathrm{rad}}$.

A.5 Reconstruction of Experimental Data and Derivation of CFD Validation Parameters

In order to obtain validation data representative of the column entrance region, additional $k_{Ga}e$ values were interpolated from the experimental measurements reported by Aroonwilas et al. [19]. The interpolation was carried out via linear regression on digitized data points extracted from the original figure, and the corresponding operational parameters were applied accordingly.

A.5.1 Data reconstruction and regression details

Axial CO_2 concentration profiles $c_{\mathrm{CO_2}}(z)$ reported in [19] were digitized at $z \in [0, 2.2]$ m for $L \in \{3.82,\, 5.92,\, 7.64,\, 12.22,\, 22.91\}\,\mathrm{m^3\,m^{-2}\,h^{-1}}$. Points were de-noised by removing duplicated z and enforcing monotone sorting.

For each L, we fit a polynomial surrogate

$$\widehat{c}(z \mid L) = \sum_{k=0}^{n} a_k(L)\, z^k,$$

with coefficients obtained by weighted least squares

$$\min_{\{a_k\}} \sum_{i=1}^{N_L} w_i \left[c_i - \sum_{k=0}^{n} a_k z_i^k\right]^2, \qquad w_i = \frac{1}{\sigma_i^2}.$$

Unless otherwise noted, $w_i \equiv 1$ (homoscedastic noise). To limit overfitting we use $n = \min(3, N_L - 1)$; as a sensitivity, $n \in \{2, 3, 4\}$ was tested and the smallest n within $\Delta\mathrm{AIC} \le 2$ retained. Table A.1 lists metrics by L. Next, the fit quality is summarized by

$$R^2 = 1 - \frac{\sum_i (c_i - \widehat{c}_i)^2}{\sum_i (c_i - \bar{c})^2}, \quad \mathrm{MAE} = \frac{1}{N_L}\sum_i |c_i - \widehat{c}_i|, \quad \mathrm{MAXE} = \max_i |c_i - \widehat{c}_i|.$$

Table A.1 Fit quality for polynomial surrogates by liquid load L (errors at original digitized points).

L $[m^3 m^{-2} h^{-1}]$	Degree n	R^2	MAE [%]	MAXE [%]
3.82	3	0.996	0.068	0.126
5.92	3	0.999	0.046	0.094
7.64	3	0.999	0.059	0.152
12.22	3	0.999	0.072	0.184
22.91	3	0.998	0.160	0.359

The experimental axial CO_2 concentration profiles reported by [19] were digitized and reconstructed via polynomial regression for each liquid load, yielding the interpolated curves shown in Fig. A.16.

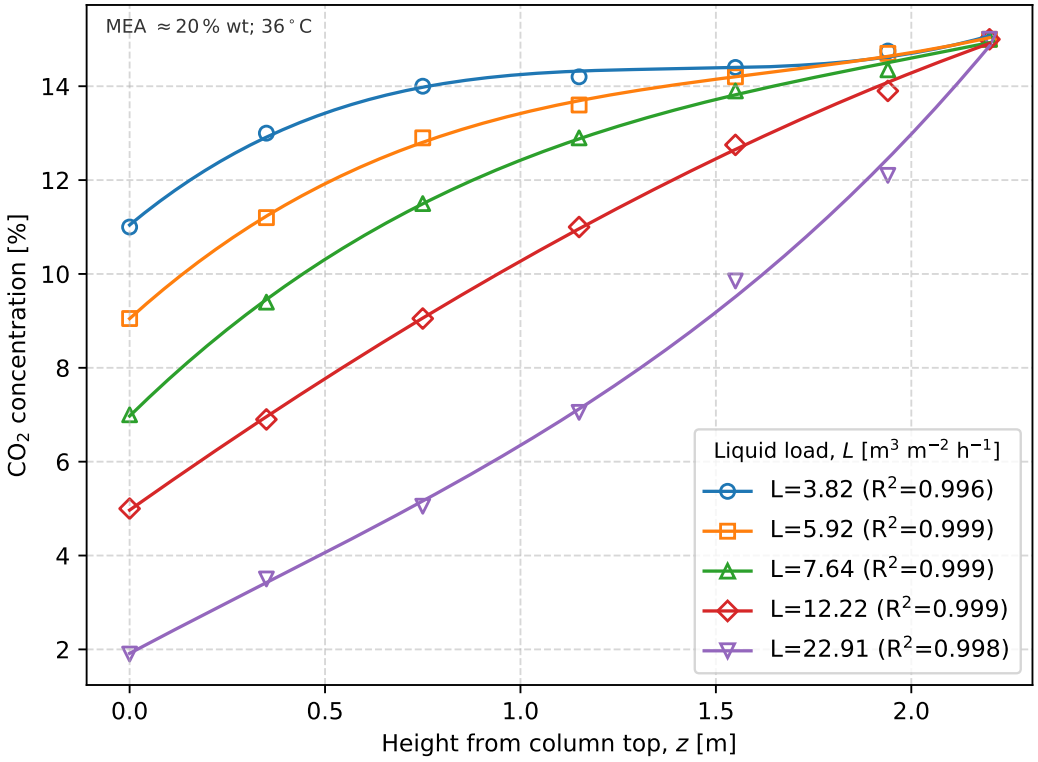


Figure A.16 Fitted validation curves from the reference [19]

A.5.2 Calculating Corresponding u_G for Reactive Absorption

In order to determine the superficial gas velocity values (u_G) corresponding to the experimental conditions of Aroonwilas et al. [19], the following reconstruction procedure was employed.

The overall gas-side mass–transfer coefficients $K_G a_e$ reported in Fig. 4 of Aroonwilas et al. [19] were first digitized for each liquid load $L \in \{3.82, 5.92, 7.64, 12.22, 22.91\}\,\mathrm{m^3\,m^{-2}\,h^{-1}}$. The values, originally expressed in

$[\mathrm{kmol\,m^{-3}\,h^{-1}\,kPa^{-1}}]$, were converted into the equivalent gas–liquid volumetric coefficients $k_G a_e\,[\mathrm{s^{-1}}]$ using the ideal–gas relation at $T = 309$ K and $R = 8.314\ \mathrm{kPa\,m^3\,mol^{-1}\,K^{-1}}$:

$$k_G a_e = K_G a_e \times \frac{RT}{3600}.$$

Using the simplified relation given in Eq. (3.18) (see Chapter 3), the gas superficial velocity u_G was computed for each L by inserting:

- the interpolated CO_2 inlet concentration C_{in} and outlet concentration C_{out} from Fig. 3 of Aroonwilas et al. [19], given in the table A.2
- the total packed height $Z = 2.2$ m,
- and the corresponding $k_G a_e\,[\mathrm{s^{-1}}]$ values obtained above.

To define the CO_2 inlet composition consistently with the experimental data, a representative axial position of $z = 0.0142$ m was selected within the column. This height corresponds to a region very close to the top of the column, where the liquid phase can be considered nearly pure MEA; therefore, it was deemed suitable for defining the inlet boundary of the CFD domain.

At this height, the interpolated concentration values from the digitized experimental profiles were extracted for all liquid loads L. The resulting inlet mole fractions are given in the table A.2. These interpolated values were used as CO_2 inlet concentrations in the CFD validation runs.

Table A.2 Operating values used for interpolation at $z = 0.0142$ m.

Variable	**Liquid load** L [$\mathrm{m^3m^{-2}h^{-1}}$]				
	3.82	5.92	7.64	12.22	22.91
C_{in} (interp. from A.16) [mol/mol]	0.11102	0.09149	0.07108	0.05077	0.01967
C_{out} [19] [mol/mol]	0.11000	0.09000	0.07000	0.05000	0.01900
$K_g a_e$ [19] [kmol $\mathrm{m^{-3}\,h^{-1}\,kPa^{-1}}$]	0.1900	0.2500	0.3000	0.3300	0.4000
$k_g a$ (calculated) [$\mathrm{s^{-1}}$]	0.1356	0.1784	0.2141	0.2355	0.2854
u_G (calculated) [m/s]	0.96	0.77	0.62	0.47	0.30

The dominant source of uncertainty originates from the digitization of Aroonwilas' experimental plots. This introduces an estimated deviation of about 1–2% in the reconstructed concentrations and $k_G a_e$ values. Given the smooth variation of u_G with these quantities, this level of deviation does not significantly affect the accuracy or sensitivity of the present validation study.

A.5.3 Holdup Data from [2]

The original Suess–Spiegel holdup curves are provided here for reference, forming the basis of the reconstructed data used in the main text.

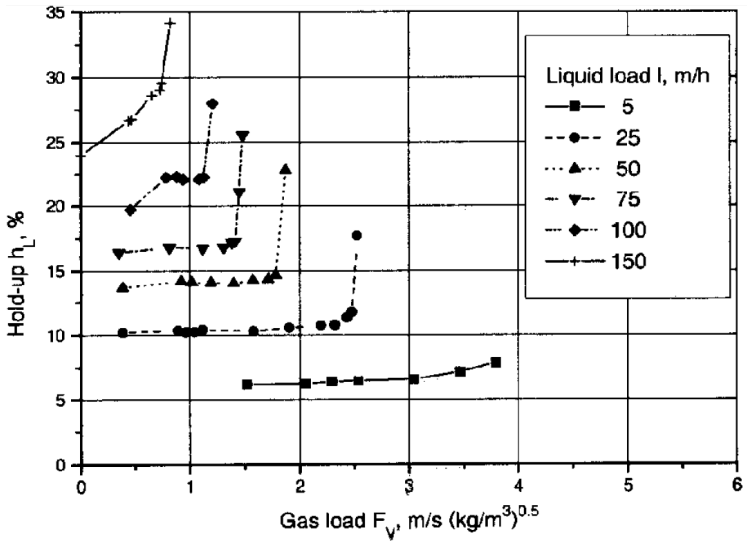


Figure A.17 Liquid holdup h_L as a function of gas load F_G for various liquid loads L for Mellapak 500Y structural packing. (Figure from [2])

A.6 Snapshots of Ansys Fluent Interface

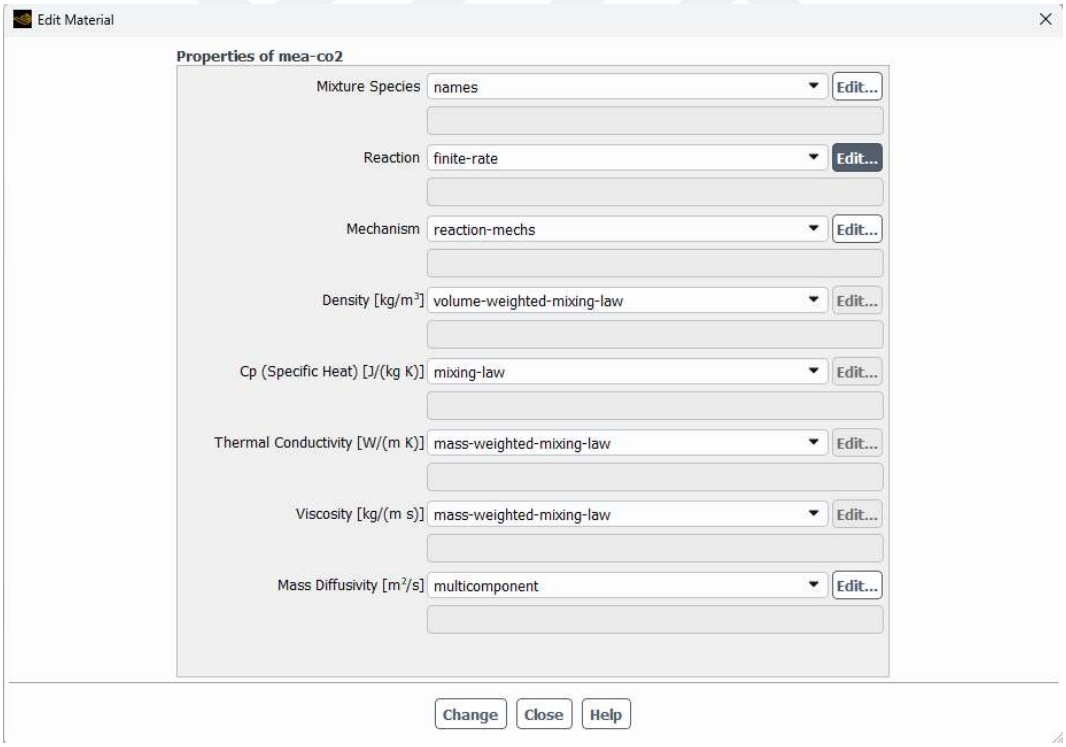


Figure A.18 ANSYS-Fluent property mixture window

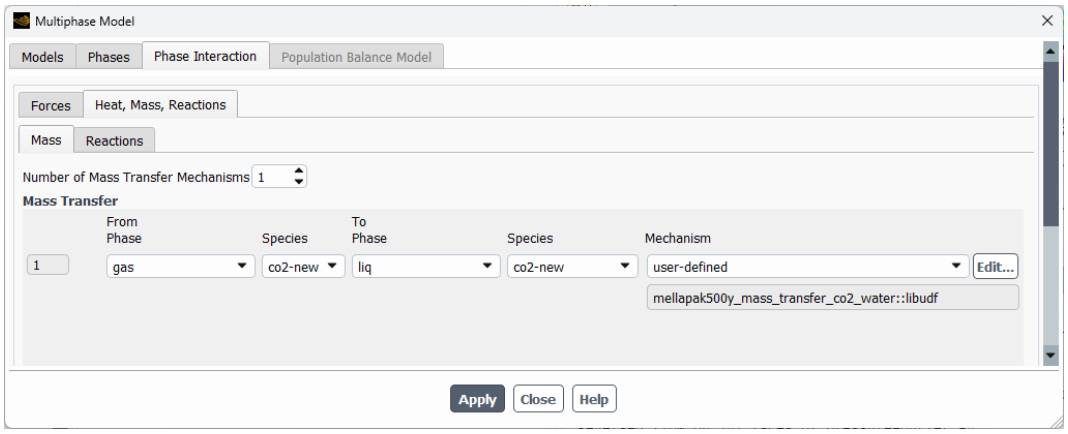


Figure A.19 ANSYS-Fluent phase interaction

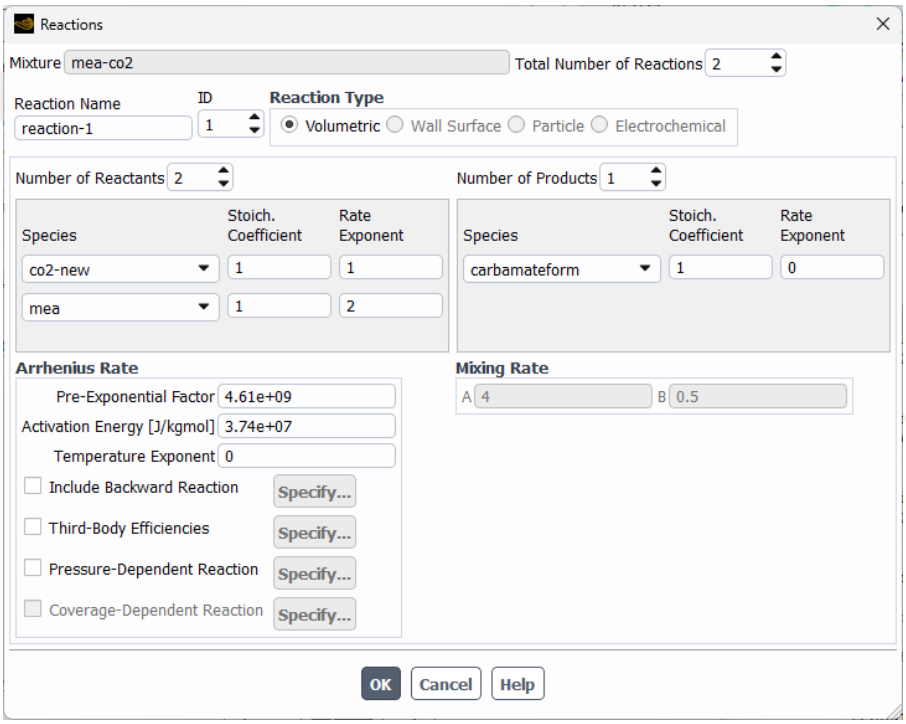


Figure A.20 ANSYS-Fluent reaction no: 1

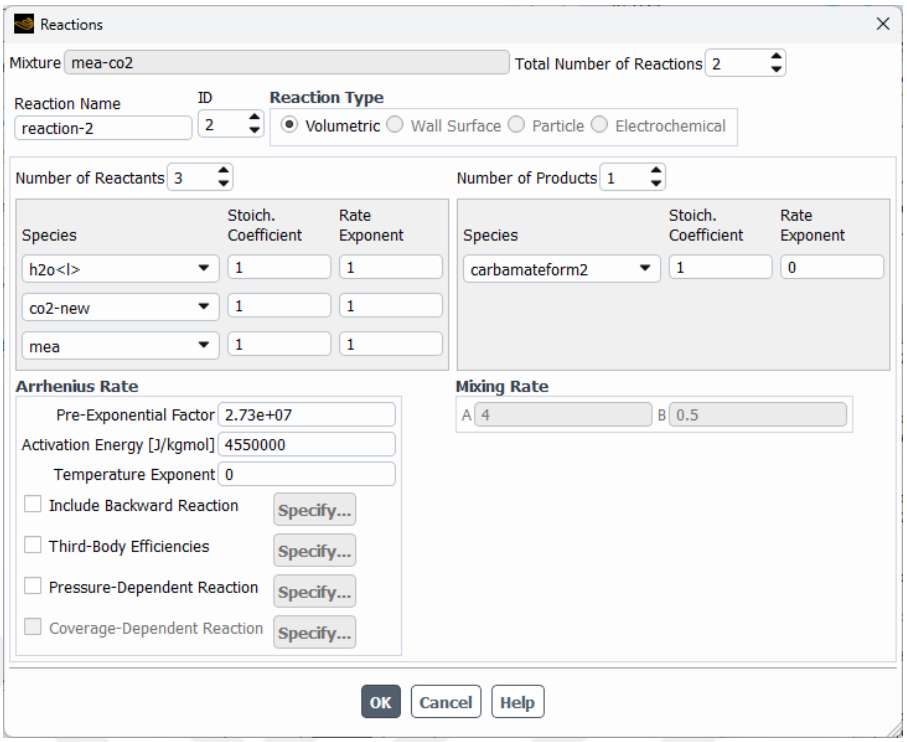


Figure A.21 ANSYS-Fluent reaction no: 2

PUBLICATIONS FROM THE THESIS

Conference Papers

1. V. Topaloğlu, H. Demir, "Numerical Investigation of Dry Pressure Drop Optimization in Structured Packing," *Proceedings of the 14th International Congress on Engineering and Technology Management*, Istanbul, Türkiye, 15–16 Nov. 2025, pp. 230–235.